

DEPARTMENT OF MECHANICAL ENGINEERING & MECHANICS
COLLEGE OF ENGINEERING & TECHNOLOGY
OLD DOMINION UNIVERSITY
NORFOLK, VIRGINIA 23529

INVESTIGATION OF NOSE BLUNTNES AND ANGLE OF ATTACK
EFFECTS ON SLENDER BODIES IN VISCOUS HYPERTENSION
FLOWS

By

A.K. Sehgal, Graduate Research Assistant

S.N. Tiwari, Principal Investigator

D.J. Singh, Research Assistant

Progress Report
For the period ended April 30, 1991

Prepared for

National Aeronautics and Space Administration
Langley Research Center
Hampton, Virginia 23665-5225

Under

Cooperative Agreement NCC1-68

Dr. Robert E. Smith Jr., Technical Monitor
ACD-Computer Applications Branch

(NASA-CR-188153) INVESTIGATION OF NOSE
BLUNTNES AND ANGLE OF ATTACK EFFECTS ON
SLENDER BODIES IN VISCOUS HYPERTENSION FLOWS
Progress Report, period ending 30 Apr. 1991
(Old Dominion Univ.) ~~125P~~ 125P CSCL 01A G3/02

N91-21117

J32596

Unclass

0008219

May 1991

Old Dominion University Research Foundation is a not-for-profit corporation closely affiliated with Old Dominion University and serves as the University's fiscal and administrative agent for sponsored programs.

Any questions or comments concerning the material contained in this report should be addressed to:

**Executive Director
Old Dominion University Research Foundation
P. O. Box 6369
Norfolk, Virginia 23508-0369**

**Telephone: (804) 683-4293
Fax Number: (804) 683-5290**

**DEPARTMENT OF MECHANICAL ENGINEERING & MECHANICS
COLLEGE OF ENGINEERING & TECHNOLOGY
OLD DOMINION UNIVERSITY
NORFOLK, VIRGINIA 23529**

**INVESTIGATION OF NOSE BLUNTNES AND ANGLE OF ATTACK
EFFECTS ON SLENDER BODIES IN VISCOUS HYPERTENSION
FLOWS**

By

A.K. Sehgal, Graduate Research Assistant

S.N. Tiwari, Principal Investigator

D.J. Singh, Research Assistant

**Progress Report
For the period ended April 30, 1991**

**Prepared for
National Aeronautics and Space Administration
Langley Research Center
Hampton, Virginia 23665-5225**

**Under
Cooperative Agreement NCC1-68
Dr. Robert E. Smith Jr., Technical Monitor
ACD-Computer Applications Branch**

**Submitted by the
Old Dominion University Research Foundation
P.O. Box 6369
Norfolk, Virginia 23508-0369**

May 1991

INVESTIGATION OF EFFECTS OF NOSE BLUNTNES AND ANGLE OF ATTACK ON SLENDER BODIES IN VISCOUS HYPERSONIC FLOWS

A.K. Sehgal¹, S.N. Tiwari², and D.J. Singh³

**Department of Mechanical Engineering and Mechanics
Old Dominion University, Norfolk, VA, 23529-0247.**

SUMMARY

Hypersonic flows over cones and straight biconic configurations are calculated for a wide range of free stream conditions in which the gas behind the shock is treated as perfect. Effect of angle of attack and nose bluntness on these slender bodies in air is investigated extensively. The numerical procedures are based on the solution of complete Navier-Stokes equations at the nose section and parabolized Navier Stokes equations further downstream. The flow field variables and surface quantities show significant differences when the angle of attack and nose bluntness are varied. The complete flow field is thoroughly analyzed with respect to velocity, temperature, pressure and entropy profiles. The post-shock flow field is studied in detail from the contour plots of Mach number, density, pressure and temperature. Flow separation is observed on the leeward plane for an on-axis, $12.84^\circ / 7^\circ$ (fore-cone and aft-cone angle) biconic geometry at 12° angle of attack. Also, the windward and leeward heating rates for the fore-cone section decreases by a factor of four and by a factor of five respectively, when the nose bluntness is increased by an order of magnitude. The effect of nose bluntness for slender cone persists as far as 200 nose radii downstream.

¹ Graduate Research Assistant

² Eminent Professor

³ Present Affiliation : Research Scientist, Analytical Services and Materials Inc., Hampton, VA 23666

ACKNOWLEDGEMENTS

This is a progress report on the research project "Numerical Solutions of Three-Dimensional Navier-Stokes Equations for Closed-Bluff Bodies," for the period ended April 30, 1991. Specific efforts during this period were directed in the area of "Investigation of Nose Bluntness and Angle of Attack Effects on Slender Bodies in Viscous Hypersonic Flows."

This work was supported by the NASA Langley Research Center through Cooperative Agreement NCC1-68. The cooperative agreement was monitored by Dr. Robert E. Smith Jr. of the Analysis and Computation Division (Computer Applications Branch), NASA Langley Research Center, mail stop 125. The work, in part, was also supported by the Old Dominion University's ICAM Project through NASA Grant NAG-1-363; this grant was monitored by Dr. Samuel E. Massenberg, University Affairs Officer, NASA Langley Research Center, Hampton, Virginia 23665-5225. The authors are indebted to Dr. A. Kumar of NASA Langley Research Center (FLDMD-Theoretical Flow Physics Branch) for originally suggesting the need for this research

TABLE OF CONTENTS

	Page
ACKNOWLEDGEMENTS	ii
LIST OF TABLES	v
LIST OF FIGURES	vi
LIST OF SYMBOLS	xi
Chapter	
1 INTRODUCTION	1
2 PHYSICAL MODEL AND THEORETICAL CONCEPTS	7
2.1 Downstream Effects of Nose Bluntness and Angle of Attack .	10
2.1.1 Aerodynamic Heating	10
2.1.2 Entropy Layer	11
2.1.3 Bluntness and Angle of Attack Effects on Transition .	13
3 THEORETICAL FORMULATIONS	15
3.1 Introduction	15
3.2 Basic Governing Equations	16
3.3 Streamwise Pressure Gradient	20
3.4 Freestream and Boundary Conditions	22
4 METHOD OF SOLUTION	23
4.1 Boundary Conditions	26
4.2 Shock Fitting Procedure	30

5 RESULTS AND DISCUSSION	34
5.1 Results for Slender Cone	34
5.2 Results for the Straight Biconic	41
5.2.1 Experimental Verification	42
5.2.2 Nose Bluntness Effects	42
5.2.3 Effects of Angle of Attack	60
5.2.4 Effects of Nose Bluntness and Angle of Attack on Flow field Quantities	67
6 CONCLUSIONS	100
REFERENCES	102
APPENDIX A CALCULATION OF JACOBIANS	105

LIST OF TABLES

<u>TABLE</u>		<u>PAGE</u>
5.1	Freestream flow conditions for 5° cone, $\alpha=0^\circ$ and 2°	35
5.2	Freestream flow conditions for $12.87^\circ / 7^\circ$ bicone; $\alpha=0^\circ, 8^\circ$ and 12° .	35

LIST OF FIGURES

<u>FIGURE</u>		<u>PAGE</u>
2.1	Physical model for hypersonic flow past a blunt slender cone.	8
2.2	Physical model for hypersonic flow past on-axis $12.84^\circ / 7^\circ$ biconic configuration.	9
4.1	Grid for $12.84^\circ / 7^\circ$ biconic configuration at 0° AOA.	27
4.2	Grid for $12.84^\circ / 7^\circ$ biconic configuration at 12° AOA.	28
5.1	Variation of wall pressure with axial distance for blunted cone at 0° and 2° AOA.	37
5.2	Variation of shock standoff distance with axial distance for blunted cone at 0° and 2° AOA.	38
5.3	Variation of wall heat transfer with axial distance for blunted cone at 0° and 2° AOA.	39
5.4	Variation of skin friction coefficient with axial distance for blunted cone at 0° and 2° AOA.	40
5.5	Comparison of experimental and numerical results of variation of wall heat flux with axial distance for straight biconic at 0° AOA.	44
5.6	Comparison of experimental and numerical results of variation of wall heat flux with axial distance for straight biconic at 12° AOA.	45
5.7	Effect of nose bluntness on surface pressure for on-axis biconic at 0° AOA.	46

5.8	Effect of nose bluntness on wall heat transfer for on-axis biconic at 0° AOA.	47
5.9	Effect of nose bluntness on skin friction coefficient for on-axis biconic at 0° AOA.	48
5.10	Effect of nose bluntness on shock stand-off distance for on-axis biconic at 0° AOA.	49
5.11	Effect of nose bluntness on surface pressure for on-axis biconic at 12° AOA.	50
5.12	Effect of nose bluntness on wall heat transfer for on-axis biconic at 12° AOA.	51
5.13	Effect of nose bluntness on skin friction coefficient for on-axis biconic at 12° AOA.	52
5.14	Effect of nose bluntness on shock shape for on-axis biconic at 12° AOA.	53
5.15	Circumferential variation of coefficient of pressure for on-axis biconic at 0° , 8° and 12° AOA, $x=18.016 R_n$	54
5.16	Circumferential variation of wall heat transfer for on-axis biconic at 0° , 8° and 12° AOA, $x=18.016 R_n$	55
5.17	Circumferential variation of skin friction coefficient for on-axis biconic at 0° , 8° and 12° AOA, $x=18.016 R_n$	56
5.18	Circumferential variation of coefficient of pressure for on-axis biconic at 0° and 12° AOA, $R_n = 0.04$ m, $x=30.89 R_n$	57
5.19	Circumferential variation of wall heat transfer for on-axis biconic at 0° and 12° AOA, $R_n = 0.04$ m, $x=30.89 R_n$	58
5.20	Cross flow velocity vector plot for on-axis biconic at 12° AOA, $R_n = 0.04$ m, $x=30.89 R_n$	59

5.21	Variation of surface pressure with axial distance for $12.84^\circ / 7^\circ$ on-axis biconic at 0° , 8° and 12° AOA.	62
5.22	Variation of wall heat transfer with axial distance for on-axis biconic at 0° , 8° and 12° AOA.	63
5.23	Variation of skin friction coefficient with axial distance for on-axis biconic at 0° , 8° and 12° AOA.	64
5.24	Variation of shock stand-off distance with axial distance for on-axis biconic at 0° , 8° and 12° AOA.	65
5.25	Variation of shock shape with axial distance for on-axis biconic at 8° and 12° AOA.	66
5.26	Variation of surface pressure with axial distance for on-axis biconic at 0° and 12° AOA, $R_n=0.04$ m.	68
5.27	Variation of wall heat transfer with axial distance for on-axis biconic at 0° and 12° AOA, $R_n=0.04$ m.	69
5.28	Variation of skin friction coefficient with axial distance for on-axis biconic at 0° and 12° AOA, $R_n=0.04$ m.	70
5.29	Variation of shock standoff distance with axial distance for on-axis biconic at 0° and 12° AOA for $R_n=0.04$ m.	71
5.30	Variation of shock shape with axial distance for on-axis biconic at 0° and 12° AOA, $R_n=0.04$ m.	72
5.31	u velocity profile for on-axis biconic at 0° AOA.	76
5.32	u velocity profile at leeward side for on-axis biconic at 12° AOA.	77
5.33	u velocity profile at windward side for on-axis biconic at 12° AOA.	78
5.34	Temperature profiles for on-axis biconic at 0° AOA.	79
5.35	Temperature profiles at leeward side for on-axis biconic at 12° AOA.	80
5.36	Temperature profiles at windward side for on-axis biconic at 12° AOA.	81
5.37	Entropy profiles for on-axis biconic at 0° AOA.	82

5.38	Entropy profiles at leeward side for on-axis biconic at 12° AOA.	83
5.39	Entropy profiles at windward side for on-axis biconic at 12° AOA.	84
5.40	Pressure profiles for on-axis biconic at 0° AOA.	85
5.41	Pressure profiles at leeward side for on-axis biconic at 12° AOA.	86
5.42	Pressure profiles at windward side for on-axis biconic at 12° AOA.	87
5.43	Mach contours for on-axis biconic at 0° AOA, $R_n=0.00383$ m, $x=11.9 R_n$	88
5.44	Density contours for on-axis biconic at 0° AOA, $R_n=0.00383$ m, $x=11.9 R_n$	89
5.45	Pressure contours for on-axis biconic at 0° AOA, $R_n=0.00383$ m, $x=11.9 R_n$	90
5.46	Temperature contours for on-axis biconic at 0° AOA, $R_n=0.00383$ m, $x=11.9 R_n$	91
5.47	Mach contours for on-axis biconic at 12° AOA, $R_n=0.00383$ m, $x=26 R_n$	92
5.48	Density contours for on-axis biconic at 12° AOA, $R_n=0.00383$ m, $x=26 R_n$	93
5.49	Pressure contours for on-axis biconic at 12° AOA, $R_n=0.00383$ m, $x=26 R_n$	94
5.50	Temperature contours for on-axis biconic at 12° AOA, $R_n=0.00383$ m, $x=26 R_n$	95
5.51	Mach contours for on-axis biconic at 12° AOA, $R_n=0.04$ m, $x=26 R_n$	96
5.52	Density contours for on-axis biconic at 12° AOA, $R_n=0.04$ m, $x=26 R_n$	97
5.53	Pressure contours for on-axis biconic at 12° AOA, $R_n=0.04$ m, $x=26 R_n$	98

LIST OF SYMBOLS

C_d	= coefficient of drag
C_f	= coefficient of skin friction, $\frac{\tau_w}{\frac{1}{2}\rho_\infty V_\infty^2}$
C_p	= coefficient of pressure, $\frac{P_w - P_\infty}{\frac{1}{2}\rho_\infty V_\infty^2}$
e	= internal energy per unit volume nondimensionalized by V_∞^2
h_{aw}	= enthalpy for adiabatic wall
h_w	= enthalpy at wall
J	= transformation Jacobian
M	= Mach number
p	= pressure nondimensionalized by $\frac{1}{2}\rho_\infty V_\infty^2$
P_r	= Prandtl number
q	= heat transfer, W/m^2
Q_w	= dimensional wall heat flux in MW/m^2
\bar{Q}_w	= wall heat transfer nondimensionalized by $\rho_\infty V_\infty^3$
r	= normal radius, m
r_{sh}	= shock shape, m
R	= specific gas constant, J/(kg.K)
Re	= Reynolds number
R_n	= nose radius, m
s	= distance along body surface measured from the stagnation point, m
T	= temperature nondimensionalized by T_∞
u	= axial velocity nondimensionalized by V_∞
U	= conservative variable
v	= normal component of velocity nondimensionalized by V_∞
V_∞	= freestream velocity

w	= circumferential component of velocity nondimensionalized by V_∞
x	= streamwise coordinate in physical domain measured from virtual tip of sharp nose
y	= normal coordinate in physical domain
γ	= ratio of specific heats
δ	= shock standoff distance, m
θ_a	= aft cone half angle
θ_c	= cone half angle
θ_f	= fore cone half angle
ϕ	= meridian angle
μ	= dynamic viscosity nondimensionalized by μ_∞
ξ, η, ζ	= curvilinear coordinates
ρ	= density nondimensionalized by ρ_∞
τ	= viscous shear stress

Subscripts

B	= body
w	= conditions at wall
∞	= freestream conditions

Chapter 1

INTRODUCTION

The field of hypersonic aerodynamics has been studied extensively in recent years with a resurgence of interest. The main reason for this motivation is the currently envisaged National Aerospace plane (NASP) which will cruise at hypersonic speeds. The propulsion system of such hypersonic flight vehicle is dominated by complex interactions of multiple shocks with the viscous flow. A better understanding of the complex flow field in different regions of the aerospace vehicle and determination of performance characteristics is essential for vehicle design. The renewed interest in hypersonic flows is also due to possibility of manned exploration of the planets. Mars, because of its close vicinity to earth and its physical characteristics makes it the first choice for such a mission. After adequate knowledge about Mars atmosphere being available, the aerocapture and aerobraking have become promising techniques in planetary missions and Earth orbital transfer applications. With the use of these techniques there is a significant increase in the payload weight and reduced transit times as compared to a pure rocket propulsion system.

The aerobraking [1]* technique uses the drag during successive passes through the upper atmosphere of the planet to circularize a highly elliptical orbit. The aerocapture represents a transfer of the vehicle into a closed stable orbit from a fly-by trajectory. The primary design factors for these transatmospheric vehicles are high lift to drag ratio, low hypersonic ballistic coefficient, and high volumetric efficiency. Straight and bent biconics are being considered as the relevant configurations for these vehicles. Also, biconic shapes would fit nicely into the shuttle orbiter bay.

* The numbers in brackets indicate references.

To avoid a conservative design involving larger and heavier control characteristics, thus reducing scientific return, an accurate database on vehicle performance during entry is needed. Because wind tunnels are not capable of duplicating the full flight trajectory of a planetary entry vehicle, numerical techniques must be relied upon heavily to furnish this database, that is, to furnish the flow environment surrounding the vehicle during entry. With recent advancements in Computational Fluid Dynamics (CFD), a wide variety of complicated flow fields in different regions of the transatmospheric vehicle can be analyzed. Numerical modelling of the flow field has proven to be a valuable tool for getting better insight into the complex nature of these flows.

For many hypersonic applications, forebody configurations are relatively simple and can be modelled by long slender bodies of revolution with a blunted nose. In the analysis of the vehicle flow field , the forebody flow provides the initial conditions. It becomes inevitable to accurately predict the forebody flow field by incorporating realistic flow conditions and geometrical modelling. There are two important features which have significant effects on the entire flow field, one is the angle of attack (AOA) and the second is the nose bluntness.

One of the important fields of investigation in hypersonic aerodynamics is the determination of heat transfer to the body surface as a function of body shape and flight conditions. This problem is of practical interest because the aerodynamic heating at hypersonic speeds is very large and represents the major limiting factor for some of the useful flight conditions. Usually, all hypersonic vehicles have blunt noses or blunt leading edges, in order to reduce (to acceptable values) the heat transfer in the stagnation regions. Blunt leading edges, however, result in a drastic increase in drag. With the advancement in material technology, it is possible to reduce the leading edge thickness without encountering intolerable heating rates in the vicinity of the nose.

The presence of blunt noses or leading edges and, therefore, of detached and highly curved shocks introduces the necessity of considering in the heat transfer investigations

new parameters related to the entropy gradients existing in the flow. The presence of large entropy gradients in the flow field can affect the heat transfer on the body and the transition of boundary layers from laminar to turbulent. The extent to which this bluntness influences the development of flow downstream is not known precisely for hypersonic flows. In general, such a calculation is very difficult because of the various intervening effects such as pressure interaction, vorticity interaction, and curvature parameters.

When the free stream is at an angle of incidence, the wall quantities and flow field variables are affected significantly. The circumferential shock shape gets displaced towards the leeward side and no longer remains concentric with the conical body. The surface pressure, wall heat transfer and skin friction show higher values on the windward meridian as compared to the leeward meridian. The circumferential distribution of surface quantities show maximum values on the most windward rays and minimum on the most leeward rays. At AOA exceeding the fore cone half angle, there exists an imbedded shock within the shock layer on the leeward side. At high AOA, the flow on the leeward side separates in a circumferential mode, forming two symmetrical, supersonic, counter-rotating longitudinal vortices.

To calculate the flow over blunted slender bodies, two sets of equations are utilized in the present investigation. For the nose section, the use of full Navier-Stokes (NS) equations is necessary due to the presence of a relatively large subsonic region, but immediately downstream of the nose region on the body, the flow becomes predominantly supersonic and the space marching parabolized Navier-Stokes equations (PNS) are used.

Recently, Singh and Tiwari [2] have done an extensive literature survey on the nose bluntness, AOA and viscous interaction effects on slender bodies at hypersonic speeds. However a few important numerical and experimental works related to the present study are reviewed here. Tracy [3] conducted an experimental study of a 10° semi-apex circular cone in air at Mach 8 and at yaw angles up to 24° . The basic measurements consisted of surface pressure, heat transfer and a complete survey of the Pitot pressure

in the flow field. The probe data delineated the boundary between viscous and inviscid flow and determined the shape of the outer shock as well as imbedded shocks which appeared in the flow field at large yaw. Lubard and Helliwell [4] investigated the flow field on cones at high angles of attack for hypersonic laminar case. They developed an iterative implicit finite difference technique to solve the three-dimensional PNS. The new theoretical approach was validated by comparing the numerical results with experimental data obtained by Tracy [3] on a sharp 10° half angle cone at $\alpha=12^\circ$ with Mach number 8 and by Stetson [5] on a sharp 5.6° half angle cone at $\alpha=8^\circ$ with Mach number of 14.2. A good agreement was found between experimental and numerical work. Stetson [6] studied the effect of bluntness and AOA on boundary layer transition on cones and biconic configurations. The rearward displacement of transition due to bluntness was found to be quite sensitive to free stream Mach number and entropy swallowing distance. Transition location was also found to be sensitive to small changes in AOA.

Holden [7] conducted an experimental study to examine the separate and combined effects of surface roughness, entropy swallowing, and boundary layer transition on the distribution of heat transfer and skin friction over a series of biconic nose tip configurations and on sharp and blunted slender cones in high speed flow over highly cooled surfaces. In this investigation, emphasis was placed on examining the effects of free stream Mach number, Reynolds number, and wall to freestream stagnation temperature ratio, in addition to exploring those introduced by roughness height and model configuration. Miller and Gnoffo [8] conducted an experimental investigation of hypersonic flows over biconics at incidence. Pressure distributions, aerodynamic coefficients, shock shapes, and oil flow patterns were measured on spherically blunted, $12.87^\circ / 7^\circ$ on-axis and bent biconics (fore cone bent 7° upwards relative to aft-cone) at Mach 6 in air for various AOA's. The experimental results were compared with the inviscid Stein code and PNS code of Vigneron et al. [9]. Miller et al. [10] did an experimental study to determine the laminar heat transfer distributions on spherically

blunted on-axis and bent biconics at hypersonic-hypervelocity flow conditions in the atmospheres of helium, hydrogen, air and carbon dioxide at different AOA's. The effect of nose bend and real gas flow phenomena on heating distributions for biconics was also studied. Experimental results were compared with a three-dimensional PNS code. Gnoffo [11] modified the PNS code of Vigneron et al. [9] for straight and bent biconic geometries. Real gas effects were included by coupling the vectorized chemical equilibrium PNS code of Kumar et al. [12] with a variable-effective-gamma capability. With the variable-effective-gamma option, gamma has been defined as the ratio of enthalpy to internal energy of the gas mixture referenced to 0 K, to replace the usual definition as the ratio of specific heats. Some recent development in this field can be found in [13–18].

Moskovitz et al. [13, 18] conducted an experimental investigation of the effects of surface perturbations on the asymmetric flow past a slender body for laminar flow conditions. The perturbations included variations in model tip sharpness and roughness as well as discrete surface perturbations represented by cylindrical beads of varying height and diameter attached to a cone/cylinder model having 10° semi-apex angle and 3.0 caliber tangent ogive model both having base diameters of 3.5 inches. The tests were conducted at 40° AOA. They concluded that local surface perturbations could reverse the direction of flow asymmetry of the basic model if they were large enough relative to the body radius where they occurred. The perturbations were most effective when located at an azimuthal position between 120° and 160° from the windward ray.

Prabhu and Tannehill [14] developed a new PNS code to compute the hypersonic laminar flow of a multicomponent, chemically reacting mixture of thermally perfect gases over two dimensional and axisymmetric bodies. The new PNS code solves the gas dynamic and species conservation equations in a coupled manner using a non-iterative, implicit, space marching, finite difference method. Ericsson [15] studied the effect of nose bluntness and cone angle on boundary layer transition for slender cone geometry. He simulated the combined effect of these two parameters on transition analytically.

He also showed how the transition dependence on the nose bluntness induced inviscid shear layer changes when moving from the entropy swallowing (small bluntness) to the entropy impingement (large bluntness) region. Malik et al. [16] studied the effect of nose bluntness on boundary layer instability for Mach 8 flow past a 7° semi-vertex cone. In order to account for the variable entropy effects associated with the bow shock, the basic flow was computed using PNS equations. Linear stability analysis of the basic flow revealed that with small amount of bluntness, the critical Reynolds number for the onset of instability increased by an order of magnitude compared to the sharp cone value. Gupta et al. [17] did numerical analysis for hypersonic laminar and turbulent flows over blunted sphere cones using time-steady viscous shock layer equations. Results were obtained from a spatial marching, implicit, finite difference technique, which included coupling of the normal momentum and continuity equations and the use of the Vigneron [9] pressure condition in subsonic nose region to ensure stability.

In the present study, the PNS code of Vigneron et al. [9] was modified for the on-axis biconic geometry. The objective of the present investigation is to conduct a parametric study to determine the effect of AOA and nose bluntness on the entire flow field past slender bodies under different freestream conditions in viscous hypersonic flows. The slender bodies considered here are blunted cones and on-axis biconics with circular cross sections. Entropy was calculated at different axial locations in the streamwise direction for straight biconics under varying nose radii and AOA's. By comparing entropy, velocity, temperature, and pressure profiles, an estimate can be made about entropy layer swallowing distance for the straight biconic geometry.

The physical model and certain theoretical concepts are presented in Chap. 2. In Chap. 3 the theoretical formulation of the problem is provided. The solution procedure is explained in Chap. 4. The results obtained in the present study are discussed in detail in Chap. 5. Finally in Chap. 6, the conclusions are presented.

Chapter 2

PHYSICAL MODEL AND THEORETICAL CONCEPTS

The calculation of hypersonic viscous flow fields past long slender axisymmetric blunt bodies is of prime interest to the designer of certain aerospace vehicles. A wide variety of flow conditions are encountered during the transatmospheric flight of these vehicles. The forebody of these vehicles must have finite thickness in order to sustain the pressure and heating rates encountered at hypersonic speeds. For selected applications, the forebody is modelled by spherically blunted cones and biconics. The physical model for hypersonic flow past a blunt slender cone is shown in Fig. 2.1. The relative positions of boundary, entropy and shock layers are indicated in the figure. The first problem considered is the flow past a blunt-nosed slender cone at 0° and 2° AOA. The origin of the coordinate system is at the virtual tip of the sharp cone with x axis along the symmetry line and y axis normal to it. Due to symmetry of the flow field even at AOA, only one half of the flow field is computed. This case was run just to check the computer code. Numerical results have been obtained by employing a combination of a NS code and a PNS code. The results obtained are discussed in detail in Chap. 5

In the first problem, a 5° half angle cone with a nose tip radius of 0.025 m is selected. The second geometry considered (Fig. 2.2) is a spherically blunted, $12.84^\circ / 7^\circ$, on-axis biconic with a bend angle of 7° [10]. The maximum length of the biconic is $31.916 R_n$. The aft section starts after $x=18.159 R_n$. For this configuration, two nose tips with radii of 0.00383 m and 0.04 m are considered, with the smallest nose radius tip approximating the sharp tip. Blunting was accomplished by keeping the fore cone angle, the length of the forecone, and aft section fixed, and increasing the nose radius. As the body dimensions are held fixed, the extent to which the bluntness effects propagate

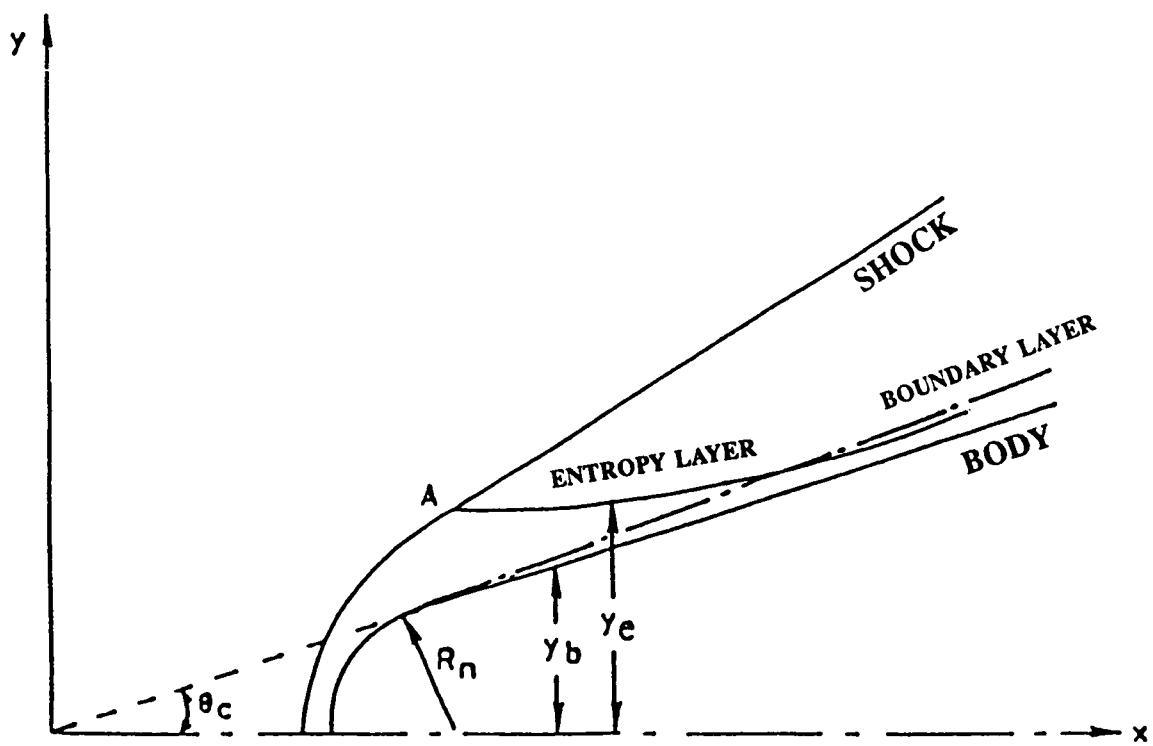


Fig. 2.1 Physical model for hypersonic flow past a blunt slender cone.

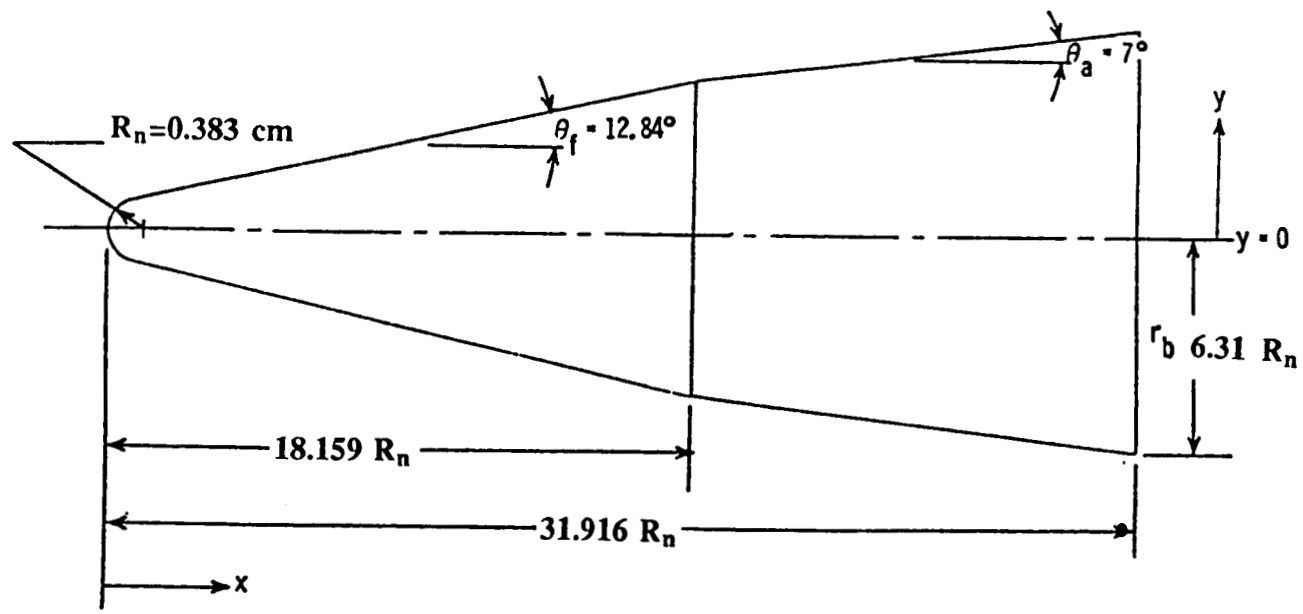


Fig. 2.2 Physical model for hypersonic flow past on-axis $12.84^\circ / 7^\circ$ biconic configuration.

downstream cannot be assessed. However, Singh and Tiwari [2, 19] have investigated this effect for blunted cones and ogives. Moreover, investigation in this area requires the minimum length of the body to be on the order of $250 R_n$. The bluntness effects are determined by comparing the solutions obtained from the blunted tip with that obtained from the sharp tip.

To study the effect of AOA on the biconic configuration, the fore cone angle and nose radius (0.00383 m) were held fixed. Results were obtained for 8° and 12° AOA cases and compared with the 0° AOA case. Next, the nose radius was increased to 0.04 m and results were obtained for 0° and 12° AOA.

2.1 Downstream Effects of Nose Bluntness and Angle of Attack

In this section, the effects of AOA and nose bluntness on the flow field and wall quantities over the forebody of a hypersonic re-entry vehicle are considered.

2.1.1 Aerodynamic Heating

From the practical aspect of the design of hypersonic vehicles, the stagnation point heat transfer becomes a vital parameter. It has been proved that the stagnation point heating varies inversely with the square root of nose radius [20], i.e.,

$$q_w \propto \frac{1}{\sqrt{R_n}}$$

Hence, the leading edge heat transfer can be reduced considerably by increasing the nose radius or bluntness. This is the reason why the nose and leading edge regions of hypersonic vehicles are designed to be blunt; otherwise, the severe aerothermal conditions in the stagnation region would quickly melt a sharp leading edge.

Aerodynamic heating becomes crucial at hypersonic speeds. For the flow over a flat plate, this is expressed as [20]

$$q_w \simeq \frac{1}{2} \rho_\infty V_\infty^3 C_h \quad (2.2)$$

where C_h is the Stanton number defined by

$$C_h = \frac{q_w}{\rho_\infty V_\infty (h_{aw} - h_w)}$$

Hence aerodynamic heating increases with cube of the velocity. By comparison, aerodynamic drag is given by

$$D = \frac{1}{2} \rho_\infty V_\infty^2 s C_d \quad (2.3)$$

which increases as the square of the velocity. Hence at hypersonic speeds, aerodynamic heating increases much more rapidly with velocity than drag, and this is the primary reason why aerodynamic heating is a dominant aspect of hypersonic vehicle design.

A major part of aerodynamic heating for a transatmospheric vehicle is encountered during ascent rather than during entry; because during ascent the vehicle will accelerate to orbital velocity within the sensible atmosphere (using air breathing propulsion), hence high velocity will be combined with relatively high density, which from Eq. (2.2) combine to yield very high heating values. In contrast, on atmospheric entry, the transatmospheric vehicle will follow a gliding flight path where deceleration to lower velocities will take place at higher altitudes, hence resulting in lower heating rates than are encountered during ascent.

2.1.2 Entropy Layer

Nose bluntness at hypersonic speeds causes the shock wave to be detached and curved in the nose region. The entropy of the flow increases across the shock layer; the stronger the shock wave, the larger the entropy increase. Thus the streamline passing through the nearly normal portion of the shock will have a large entropy increase than a streamline passing through the weaker portion of the shock. This change in entropy production in the nose region generates a layer of flow with an entropy gradient, known as the entropy layer. Since the entropy gradients are more severe at hypersonic Mach

numbers, it introduces a large amount of rotationality into the inviscid flow field, as can be quantitatively obtained from the Crocco's theorem

$$T\nabla s = \nabla h_0 - V \times (\nabla \times V) \quad (2.4)$$

where ∇h_0 is the gradient of total enthalpy, and $\nabla \times V$ is the vorticity.

The effects of entropy gradients can be classified into two groups [21]. For two dimensional and axially symmetric bodies, the presence of curved shocks can produce large vorticity normal to the direction of velocity at the surface and, therefore, velocity gradients in the direction normal to the body surface. These velocity gradients change the boundary layer velocity profile and, consequently, the heat transfer at the surface of the body. In this case the boundary layer profile must be such that the velocity and velocity gradients outside the boundary layer must match the shear flow outside of the boundary layer. Both the velocity and shear flow are functions of pressure and of mass flow contained in the boundary layer and thus of the Reynolds number.

The effect of entropy for three-dimensional flow can be more complicated because, for the three-dimensional case, the presence of entropy gradients can produce vorticity that has a component both normal to the stream direction and parallel to the stream direction of the flow outside the boundary layer. The component parallel to the stream direction can be large for bodies without axial symmetry and can affect heat transfer and boundary layer stability.

Ferri [22] pointed out that this interaction between the rotational external flow and the boundary layer may in some instances invalidate the classical boundary layer approach, particularly when the vorticity of the external stream is of the same order as the average vorticity in the boundary layer. These conditions may exist, for example, in the combination of low Reynolds number (low boundary-layer vorticity) and high Mach number (high external stream vorticity because of the highly curved shock). As the Reynolds number is increased, the effect of external vorticity on the boundary layer velocity and temperature profiles is lessened.

The thickness of the entropy layer is a function of the leading edge bluntness, even a small leading edge thickness generates an entropy layer which influences the local flow conditions for a large distance downstream. For some distance downstream of the blunt nose, the boundary layer grows inside the entropy layer which eventually is swallowed by the boundary layer in case of the flow past blunted cones. This distance is called the entropy swallowing distance. For conical flows, the entropy swallowing distance is defined as “the location at the cone frustum where fluid, which has gone through the strong portion of the bow shock, has been swallowed by the boundary layer [23].” This is by no means a precise definition as it depends upon the shock shape, boundary layer assumptions, and definition of entropy layer thickness.

The presence of entropy layer on a blunt nosed hypersonic body has an important effect on aerodynamic heating predictions using boundary layer techniques. In contrast, when the entire shock layer is treated as viscous from the body to the shock wave, the explicit treatment of the entropy layer is not needed. For such viscous shock layer treatment using a PNS approach, the interaction between the entropy layer and the shock layer “comes out in the wash”; no separate treatment is required, because it is contained within the framework of a fully viscous calculation.

2.1.3 Bluntness and Angle of Attack Effects on Transition

Boundary layer transition is a problem that has plagued several generations of aerodynamicists. The influence of nose tip bluntness on cone frustum transition remains an area which is poorly understood. From the results of bluntness investigations [6], it can be concluded that the effect of blunting on transition is very sensitive to free stream Mach number, with large Mach numbers producing a large rearward displacement of transition. The reason for this sensitivity with free stream Mach number is believed to be primarily related to the Reynolds number reduction associated with pressure losses across the bow shock. Small bluntness systematically moves the transition location rearward until the

maximum displacement is obtained. Large bluntness causes transition reversal. That is, additional increase in the nose tip radius or freestream Reynolds number produces a forward movement of transition. The forward movement of transition is very sensitive to small changes in Reynolds number or nose radius. The maximum rearward displacement of transition occurs under situations of low local Mach number flow. The trend of maximum transition displacement with free stream Mach number follows the trend of Reynold number reduction. Reynolds number reduction is believed to be a dominant effect associated with the rearward displacement of transition.

Although transition trends on a sharp cone at AOA may defy intuition, there seems to be general agreement regarding the expected movement of transition. Theory and experiment both indicate a rearward movement of transition on the windward ray and a forward movement on the leeward ray. The biconic configurations investigated did not produce any significant delays in the boundary layer transition (as compared to cone) and, in fact, often promoted an earlier transition.

Chapter 3

THEORETICAL FORMULATIONS

3.1 Introduction

The design of a supersonic/hypersonic vehicle requires a detailed analysis of the flow field. Calculation procedures that range from simple methods to complex numerical techniques have been developed over years. A traditional approach to the problem is to decouple the flow field into an inviscid region governed by the inviscid flow relations and a viscous region adjacent to the surface governed by the boundary layer equations. Once the inviscid flow field is known, either from experimental measurements or from a theoretical solution, procedures can be developed to generate solutions for the thin boundary layer near the vehicle surface. These procedures vary in degree of sophistication from simple correlation to numerical programs which calculate the non-similar boundary layers for laminar, transitional, and/or turbulent flows.

Two problems in the boundary layer formulation are :

1. The uncertainties in the flow properties associated with having to determine the boundary layer edge required for the solution of boundary layer equations.
2. The iterative process for locating the boundary layer edge.

In addition, for applications where a strong interaction between the viscous and inviscid regions occurs, the decoupling of the flow field is no longer an acceptable approach. This fact is particularly important for hypersonic flow fields where the shock layer is relatively thin and viscous effects may influence a large portion the shock layer. To address these types of flow fields, procedures are developed to solve the equations

of motion for the entire flow field. Obviously, the NS equations may be employed to solve such flow fields. However, the numerical solution of the NS equations requires a substantial amount of computer time and storage. This is due to the many iterations which are typically required in solving the unsteady NS equations in time until a converged steady state solution is reached. Thus it is desirable to reduce the NS equations to a form which can be solved efficiently, while concurrently the physics of the problem is essentially preserved. A popular method which has proven successful for the computation of these classes of flow fields is the space marching of the PNS equations. In this chapter, the strong conservation law form of NS and PNS equations will be presented for use with a generalized coordinate system.

3.2 Basic Governing Equations

Two sets of equations are utilized to calculate the flow over blunted slender bodies. For the nose section, the use of the full NS equations is necessary due to the presence of the subsonic region; but slightly downstream of the nose region on the body, the flow becomes predominantly supersonic and the NS equations are simplified for space marching. The NS equations without body force and external heat addition can be written in nondimensional, strong conservation form as [24]

$$\frac{\partial U}{\partial t} + \frac{\partial(E - E_v)}{\partial x} + \frac{\partial(F - F_v)}{\partial y} + \frac{\partial(G - G_v)}{\partial z} = 0 \quad (3.1)$$

where

$$\begin{aligned} U &= \{\rho, \rho u, \rho v, \rho w, \rho e_t\}^T \\ E &= \{\rho u, \rho u^2 + p, \rho uv, \rho uw, (\rho e_t + p)u\}^T \\ E_v &= \{0, \sigma_{xx}, \tau_{xy}, \tau_{xz}, \sigma_{xx}u + \tau_{xy}v + \tau_{xz}w + q_x\}^T \\ F &= \{\rho v, \rho vu, \rho v^2 + p, \rho vw, (\rho e_t + p)v\}^T \\ F_v &= \{0, \tau_{xy}, \sigma_{yy}, \tau_{yz}, \tau_{xy}u + \sigma_{yy}v + \tau_{yz}w + q_y\}^T \end{aligned}$$

$$\begin{aligned}
G &= \{\rho w, \rho w u, \rho w v, \rho w^2 + p, (\rho e_t + p)w\}^T \\
G_v &= \{0, \tau_{xz}, \tau_{yz}, \sigma_{zz}, \tau_{xz}u + \tau_{yz}v + \sigma_{zz}w + q_z\}^T \\
\sigma_{xx} &= \frac{2\mu}{3Re} \left(2\frac{\partial u}{\partial x} - \frac{\partial v}{\partial y} - \frac{\partial w}{\partial z} \right) \\
\sigma_{yy} &= \frac{2\mu}{3Re} \left(2\frac{\partial v}{\partial y} - \frac{\partial u}{\partial x} - \frac{\partial w}{\partial z} \right) \\
\sigma_{zz} &= \frac{2\mu}{3Re} \left(2\frac{\partial w}{\partial z} - \frac{\partial u}{\partial x} - \frac{\partial v}{\partial y} \right) \\
\tau_{xy} &= \frac{\mu}{Re} \left[\frac{\partial u}{\partial y} + \frac{\partial v}{\partial x} \right] \\
\tau_{xz} &= \frac{\mu}{Re} \left[\frac{\partial v}{\partial z} + \frac{\partial w}{\partial x} \right] \\
\tau_{yz} &= \frac{\mu}{Re} \left[\frac{\partial u}{\partial z} + \frac{\partial w}{\partial y} \right] \\
q_x &= \frac{\mu}{M_\infty^2 Re_l Pr(\gamma - 1)} \frac{\partial T}{\partial x} \\
q_y &= \frac{\mu}{M_\infty^2 Re_l Pr(\gamma - 1)} \frac{\partial T}{\partial y} \\
q_z &= \frac{\mu}{M_\infty^2 Re_l Pr(\gamma - 1)} \frac{\partial T}{\partial z}
\end{aligned}$$

and

$$e_t = e + \frac{u^2 + v^2 + w^2}{2} \quad (3.2)$$

$$p = (\gamma - 1)\rho e \quad (3.3)$$

These equations are nondimensionalized with respect to freestream values [9]. The coefficient of viscosity μ is obtained using the Sutherland's law

$$\mu = T^{\frac{3}{2}} \left(\frac{1 + T_{ref}}{T + T_{ref}} \right) \quad (3.4)$$

where $T_{ref} = \frac{110.4K}{T_\infty}$. For perfect gas calculations, Prandtl number is taken as 0.72. The computed entropy profiles are presented in this study. The entropy change $\Delta\bar{S}$ is computed assuming a perfect gas as

$$\Delta\bar{S} = \frac{\gamma}{\gamma - 1} \ln \frac{T}{T_\infty} - \ln \frac{P}{P_\infty} \quad (3.5)$$

where $\Delta\bar{S} = \frac{S - S_\infty}{R}$.

For the spherical nose region of the body, the flow is analyzed by the code SOFIA [25]. The code solves the complete set of NS equations using an explicit, finite volume, alternating two-step scheme, and uses local time stepping to accelerate the convergence to steady state. It also incorporates time dependent adaptive grid to properly resolve the flow gradients without increasing the grid points. Once the flow field is obtained over the nose section, it is used to provide an initial plane solution to initialize the PNS equations.

In the present investigation, a parabolized Navier-Stokes code developed by Vigneron et al. [9] is used for analyzing the downstream flow over the bodies. The PNS equations are a subset of the complete NS equations and can be used to predict many complex three-dimensional, steady, supersonic, viscous flow fields. These equations can be solved using a space marching technique instead of the time marching procedure which is usually employed for the NS equations. As discussed earlier, they are valid in both viscous and inviscid regions, and thus unlike boundary layer equations no special effort is needed for viscous/inviscid interactions. They can be obtained by

1. neglecting unsteady terms.
2. neglecting all viscous gradients in the streamwise direction.
3. modifying the streamwise pressure gradient term in the subsonic region to permit stable marching of the equations from the initial data plane.

Technically, it is not necessary to drop the unsteady terms in order to “parabolize” the equations (i.e., make the equations hyperbolic/parabolic in the streamwise direction). Some iterative space marching methods actually retain the time derivative term.

For space marching of these equations to be applicable, the majority of the flow field should be supersonic in the streamwise direction and the streamwise velocity component should be positive. Typically space marching of these equations will become unstable and fail in the presence of streamwise separation, although regions of crossflow separation present no special difficulties. In addition, regions of subsonic flow (immediately adjacent to the solid walls due to the no-slip boundary condition) should be thin, and the streamwise pressure gradient in these subsonic regions should not be strong. Otherwise, results could be poor. The following two independent variable transformations are applied to allow for conical effects and stretching between the body and shock

$$a = x \quad b = \frac{y}{x} \quad c = \frac{z}{x} \quad (3.6)$$

$$\xi = a \quad \eta = \eta(a, b, c) \quad \zeta = \zeta(b, c) \quad (3.7)$$

Upon combining Eqs. (3.1), (3.6) and (3.7), neglecting unsteady terms and viscous derivatives in the ξ direction, the PNS equations are expressed as [9]

$$\frac{\partial E_1}{\partial \xi} + \frac{\partial F_1}{\partial \eta} + \frac{\partial G_1}{\partial \zeta} = 0 \quad (3.8)$$

where

$$\begin{aligned} E_1 &= \frac{a^2 E}{J} \\ F_1 &= \frac{a}{J} \left[\left(a \frac{\partial \eta}{\partial a} - b \frac{\partial \eta}{\partial b} - c \frac{\partial \eta}{\partial c} \right) (E - E_v) + \frac{\partial \eta}{\partial b} (F - F_v) + \frac{\partial \eta}{\partial c} (G - G_v) \right] \\ G_1 &= \frac{a}{J} \left[\left(-b \frac{\partial \zeta}{\partial b} - c \frac{\partial \zeta}{\partial c} \right) (E - E_v) + \frac{\partial \zeta}{\partial c} (G - G_v) \right] \\ J &= \frac{\partial(\eta, \zeta)}{\partial(b, c)} \end{aligned}$$

The flux vector E_1 in Eq. (3.8) includes the pressure and, therefore, the streamwise pressure gradient appears in $\frac{\partial E_1}{\partial \xi}$. With no modification of the streamwise pressure gradient within the subsonic regions, the equations are elliptic in these regions, and thus the downstream flow field is allowed to influence the upstream flow. Therefore, a space marching procedure to solve the system cannot be incorporated unless this elliptic influence is suppressed. If a marching procedure is used, exponential growth or decay in the solution near the surface can occur, which in turn will cause failure of the numerical scheme. This failed solution is known as the departure solution. To overcome this difficulty, the streamwise pressure gradient is modified in the subsonic regions. One approach is to split the inviscid flux vector E_1 as

$$E_1 = E_1^* + P \quad (3.9)$$

where

$$\begin{aligned} E_1^* &= \{\rho u, \rho u^2 + \Omega p, \rho uv, \rho uw, (\rho e_t + p)u\}^T \\ P &= \{0, (1 - \Omega)p, 0, 0, 0\}^T \end{aligned}$$

In the supersonic portion of the flow field, $\Omega=1$ and no modification of the pressure gradient is required; but in the subsonic regions of the flow the streamwise pressure gradient is to be treated specially.

3.3 Streamwise Pressure Gradient

Numerous schemes have been introduced to handle the pressure gradient in subsonic regions, some of which are reviewed in this section.

1. The obvious and simplest approximation is to drop the pressure gradient within the subsonic portion of the flow. This crude approximation will introduce inaccuracies in the solution of the flow fields where large pressure gradients are present and therefore has limited use.

2. The pressure gradient is evaluated explicitly by a backward difference approximation evaluated at the previous plane, i.e.,

$$\frac{\partial p}{\partial \xi}|_{i+1} = \frac{p_i - p_{i-1}}{\Delta \xi}$$

When this approximation is used, the stability requirement imposes a lower limit on the selection of the marching step size, i.e., $\Delta \xi$ must be larger than some $(\Delta \xi)_{\min}$ which is provided by the stability analysis [24].

3. In the development of the boundary layer equations it is assumed that the normal gradient of pressure within the boundary layer is negligible. Consistent with this assumption, the streamwise pressure gradient in the PNS equations is computed at the first supersonic point and imposed upon the subsonic portion. This procedure is known as sublayer approximation. It has been observed that this approximation introduces instability in some cases.
4. Earlier the flux vector E_1 , which includes the pressure, was decomposed by introducing a parameter “ Ω ”. If one is interested in using a space marching method for integrating the PNS equation set, then the inviscid eigenvalues have to be real and the viscous eigenvalues have to be positive and real. Based on eigenvalue stability analysis, a fraction Ω of the streamwise pressure gradient may be retained and evaluated implicitly while the remaining $(1-\Omega)$ fraction is evaluated explicitly. Therefore,

$$\frac{\partial p}{\partial \xi} = \Omega \frac{\partial p}{\partial \xi}|_{\text{implicit}} + (1 - \Omega) \frac{\partial p}{\partial \xi}|_{\text{explicit}}$$

Vigneron et al. [9] determined from stability analysis that

$$\Omega = \sigma \left[\frac{\gamma M_\xi^2}{1 + (\gamma - 1)M_\xi^2} \right] \quad (3.10)$$

where σ is a safety factor, usually assigned a value of 0.8 and M_ξ is the local Mach number in ξ direction. In the regions where the flow is supersonic, $M_\xi > 1$, $\Omega=1$, also $\sigma=1$ and no approximation is incorporated.

In the present study the fourth approximation for the streamwise pressure gradient has been incorporated.

3.4 Freestream and Boundary Conditions

The freestream and the boundary conditions are dependent on specific physical model considered for investigations. Discussions on typical boundary conditions are provided in Chap. 4, and information on specific freestream conditions is given in Chap. 5.

Chapter 4

METHOD OF SOLUTION

The PNS equations are a mixed set of hyperbolic-parabolic equations in the streamwise direction. Equation (3.8) is solved with a finite difference method using the Beam and Warming [26] algorithm. It is an implicit, non-iterative (i.e., non-iterative at a fixed marching station) algorithm with approximate factorization in delta form. The choice of an implicit algorithm is justified when the limit imposed on marching step by the stability condition of an explicit method is smaller than the limit required for accuracy. The Vigneron technique is used to suppress the numerical instabilities due to streamwise pressure gradients in subsonic regions. The non-iterative character of the present method is expected to provide better efficiency than the iterative schemes of Rubin and Lin [27] and Lubard and Helliwell [28].

For the governing Eq. (3.8) written as

$$\frac{\partial E_1^*}{\partial \xi} + \frac{\partial P}{\partial \xi} + \frac{\partial F_1}{\partial \eta} + \frac{\partial G_1}{\partial \zeta} = 0 \quad (4.1)$$

the delta form of the algorithm for constant step size $\Delta\xi$ is [9]

$$\begin{aligned} & \left[\frac{\partial E_1^*}{\partial U_1} + \frac{\theta_1 \Delta \xi}{1 + \theta_2} \frac{\partial}{\partial \zeta} \left(\frac{\partial G_1}{\partial U_1} \right) \right] \left(\frac{\partial E_1^*}{\partial U_1} \right)^{-1} \left[\frac{\partial E_1^*}{\partial U_1} + \frac{\theta_1 \Delta \xi}{1 + \theta_2} \frac{\partial}{\partial \eta} \left(\frac{\partial F_1}{\partial U_1} \right) \right] \Delta^i U_1 \\ &= -\frac{\Delta \xi}{1 + \theta_2} \left(\frac{\partial F_1}{\partial \eta} + \frac{\partial G_1}{\partial \zeta} \right)^i + \frac{\theta_2}{1 + \theta_2} \Delta^{i-1} E_1 - \Delta_e P \end{aligned} \quad (4.2)$$

where the superscript i refers to the current known level $\xi=i \Delta\xi$, $i+1$ is the next or unknown marching plane and $U_1 = \frac{a^2 U}{J}$, $\Delta^i U_1 = U_1^{i+1} - U_1^i$ and the derivatives $\partial\eta$ and $\partial\zeta$ are approximated with central difference operators. This algorithm has been factored

in terms of U_1 rather than E_1^* because the computation of the Jacobians $\frac{\partial F_1}{\partial U_1}$, $\frac{\partial G_1}{\partial U_1}$ is easier than the computation of $\frac{\partial F_1}{\partial E_1^*}$, $\frac{\partial G_1}{\partial E_1^*}$ as well as other reasons of computational convenience. The Jacobians $\frac{\partial F_1}{\partial U_1}$, $\frac{\partial G_1}{\partial U_1}$ and $\frac{\partial E_1^*}{\partial U_1}$ are evaluated in Appendix A. Since the vectors E_1 , F_1 and G_1 are homogenous functions of degree one in U , the conservative form of the governing equations is maintained. For first order accuracy in ξ , the Euler implicit scheme is used ($\theta_1 = 1$ and $\theta_2 = 0$). The Jacobians are evaluated at level i and $\Delta_e P = \Delta^{i-1} P$. In the present study results were obtained with the first order scheme. If second order accuracy in ξ is desired, one can use the Crank Nicolson scheme ($\theta_1 = \frac{1}{2}$, $\theta_2 = 0$) or the three point backward implicit scheme ($\theta_1 = 1$, $\theta_2 = \frac{1}{2}$).

Two approximations are made in the computation of viscous Jacobians. The viscosity μ is assumed independent of vector U_1 and is a function of position only. The cross derivative terms in the (η, ζ) plane are neglected from the Jacobians. In practice, Eq. (4.2) is solved in the following four steps:

Step 1:

$$\left[\frac{\partial E_1^*}{\partial U_1} + \frac{\theta_1 \Delta \xi}{1 + \theta_2} \frac{\partial}{\partial \zeta} \left(\frac{\partial G_1}{\partial U_1} \right) \right] \Delta^i \bar{U}_1 = \text{RHS of (4.2)} \quad (4.3)$$

Step 2:

$$\Delta^i \tilde{U}_1 = \left(\frac{\partial E_1^*}{\partial U_1} \right) \Delta^i \bar{U}_1 \quad (4.4)$$

Step 3:

$$\left[\frac{\partial E_1^*}{\partial U_1} + \frac{\theta_1 \Delta \xi}{1 + \theta_2} \frac{\partial}{\partial \eta} \left(\frac{\partial F_1}{\partial U_1} \right) \right] \Delta^i U_1 = \Delta^i \tilde{U}_1 \quad (4.5)$$

Step 4:

$$U_1^{i+1} = U_1^i + \Delta^i U_1 \quad (4.6)$$

In step 1, $\Delta^i \bar{U}_1$ represents the vector quantity

$$\left(\frac{\partial E_1^*}{\partial U_1} \right)^{-1} \left[\frac{\partial E_1^*}{\partial U_1} + \frac{\theta_1 \Delta \xi}{1 + \theta_2} \frac{\partial}{\partial \eta} \left(\frac{\partial F_1}{\partial U_1} \right) \right] \Delta^i U_1$$

which is determined by solving the system of equations given by Eq. (4.3). This system of equations has the block tridiagonal structure which can be solved using the Thomas algorithm, where in fact, a set of uncoupled block tridiagonal systems of the type given by Eq. (4.3) must be solved at step 1. Once $\Delta^i \bar{U}_1$ is determined, it is multiplied by $\left(\frac{\partial E_1^*}{\partial U_1}\right)$ in step 2. As a result of this multiplication, the inverse matrix $\left(\frac{\partial E_1^*}{\partial U_1}\right)^{-1}$ does not have to be determined in the solution process. In step 3, a second set of the block tridiagonal systems of equations in the η direction are solved. Finally, in step 4, the vector of unknowns at station $i+1$ (i.e., U_1^{i+1}) is determined by simply adding $\Delta^i U_1$ to the vector of unknowns at station i . The primitive variables can then be easily obtained from U_1^{i+1} . In order to damp the spurious numerical oscillations due to central differencing in the cross plane, second order implicit and fourth order explicit damping terms are added. After adding the dissipation terms, the truncation error of the algorithm is consistent with the first order Euler scheme. The final algorithm is expressed (with the fourth order explicit smoothing [26] terms) as [9]

$$\begin{aligned} & \left[\frac{\partial E_1^*}{\partial U_1} + \frac{\theta_1 \Delta \xi}{1 + \theta_2} \partial \zeta \left(\frac{\partial G_1}{\partial U_1} \right) - \epsilon_I J^{-1} \nabla \zeta \Delta \zeta J \right] \left(\frac{\partial E_1^*}{\partial U_1} \right)^{-1} \times \\ & \left[\frac{\partial E_1^*}{\partial U_1} + \frac{\theta_1 \Delta \xi}{1 + \theta_2} \partial \eta \left(\frac{\partial F_1}{\partial U_1} \right) - \epsilon_I J^{-1} \nabla \eta \Delta \eta J \right] \Delta^i U_1 \\ & = -\frac{\Delta \xi}{1 + \theta_2} \left(\frac{\partial F_1}{\partial \eta} + \frac{\partial G_1}{\partial \zeta} \right)^i + \frac{\theta_2}{1 + \theta_2} \Delta^{i-1} E_1 - \Delta_e P \\ & - \epsilon_E J^{-1} \left[(\nabla \eta \Delta \eta)^2 + (\nabla \zeta \Delta \zeta)^2 \right] J U_1^i \end{aligned} \quad (4.7)$$

where ∇ and Δ are the conventional backward and forward difference operators, respectively, and ϵ_E and ϵ_I are the coefficients of explicit and implicit dissipation.

Due to symmetry of the flow field, only one half of the flow field is computed. The generalized coordinates η and ζ are defined such that the computational plane has a square shape of side unity with uniform spacing in both directions. Therefore, the correspondence between physical and computational plane is, for $1 \leq j \leq NJ$ and $1 \leq k \leq NK$, as follows

$$\eta = (k - 1)\Delta\eta$$

$$\zeta = (j - 1)\Delta\zeta$$

$$y(j, k) = y_B(j) + s(i, j, \beta) \cos [\phi(j)]$$

$$z(j, k) = z_B(j) + s(i, j, \beta) \sin [\phi(j)]$$

where

$$\Delta\eta = \frac{1}{NK - 1}, \quad \Delta\zeta = \frac{1}{NJ - 1}$$

The variable s is the stretching function depending upon η , δ and a stretching parameter β , and is expressed as

$$s(i, j, \beta) = \delta \left\{ 1 - \beta \frac{\left[\left(\frac{\beta+1}{\beta-1} \right)^{\eta} - 1 \right]}{\left[1 + \left(\frac{\beta+1}{\beta-1} \right)^{\eta} \right]} \right\} \quad (4.8)$$

The outer boundary corresponds to the shock and the inner boundary to the body. The grid points are clustered near the body to properly resolve the gradients. In the present study, a grid of 30×50 points was used, with 30 points in the circumferential direction, and 50 points in the normal direction. Figure 4.1 shows the grid for the biconic geometry at 0° AOA and Fig. 4.2 shows the grid at 12° AOA for the same geometry.

4.1 Boundary Conditions

Boundary conditions are to be specified at the body surface and at the outer boundary which in the present study is a bow shock. At the body no slip, zero pressure gradient and constant wall temperature conditions are imposed. These equations are analyzed mathematically in this section, following the procedure outlined in [29].

One may note that

$$(\Delta\rho e_t)_{i,1} = (\rho e_t)_{i+1,1} - (\rho e_t)_{i,1} \quad (4.9a)$$

At the surface, $\rho e_t = \rho e$ because the velocity at the wall is zero. In addition,

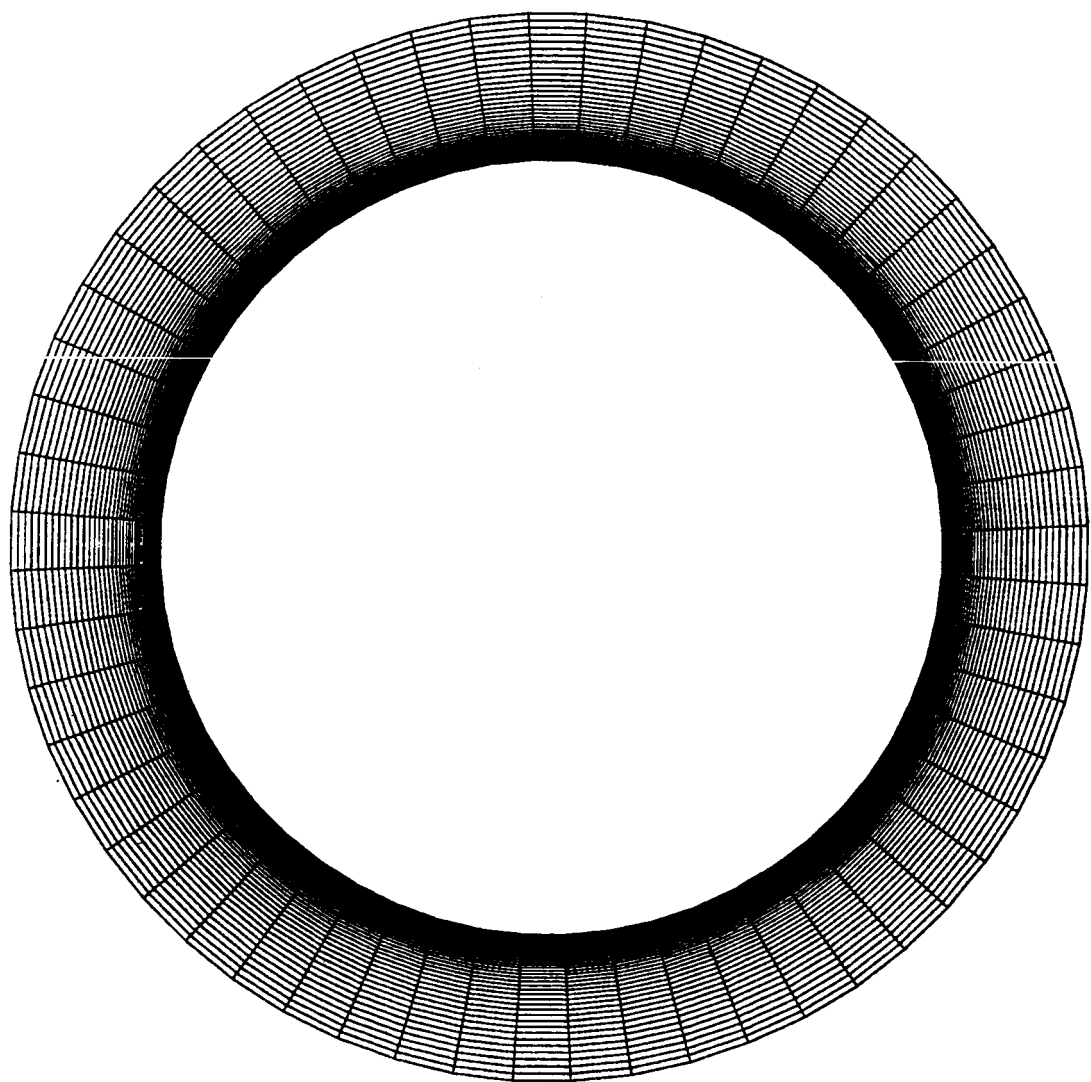


Fig. 4.1 Grid for $12.84^\circ / 7^\circ$ biconic configuration at 0° AOA.

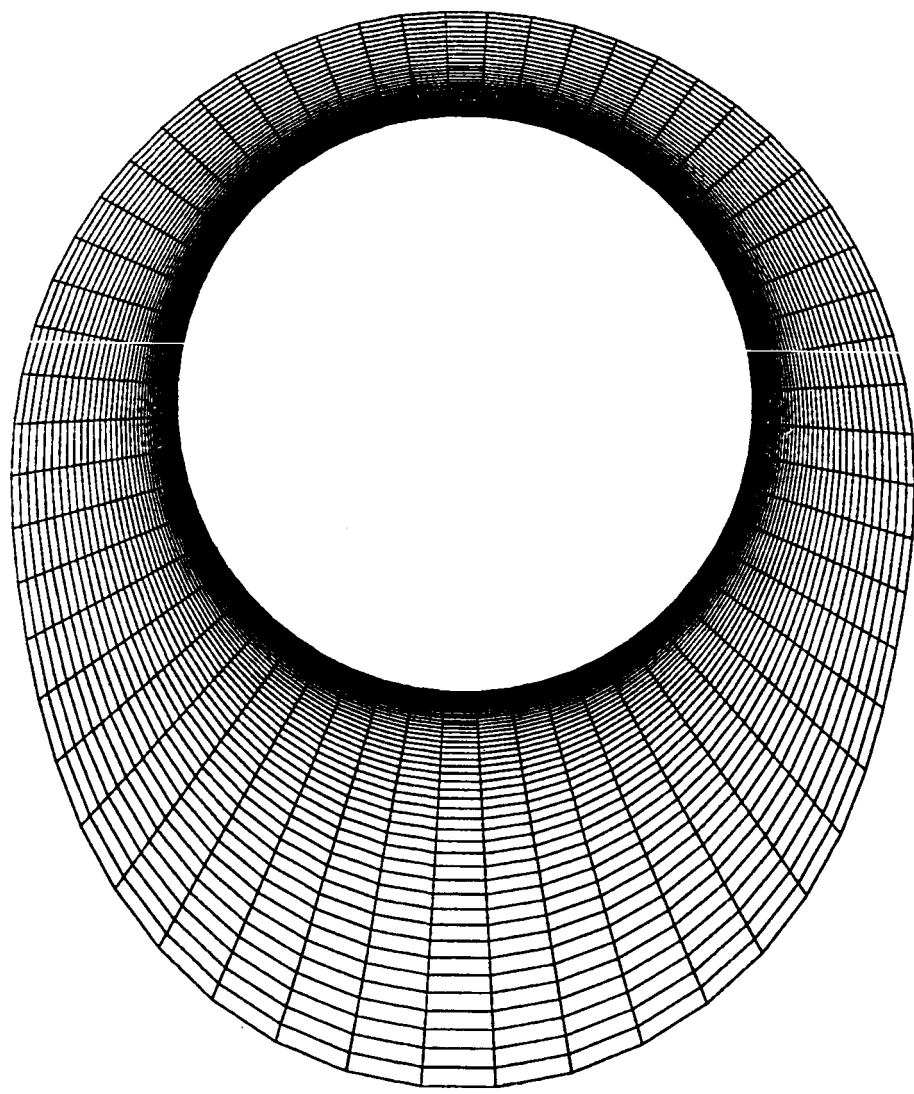


Fig. 4.2 Grid for $12.84^\circ / 7^\circ$ biconic configuration at 12° AOA.

$$e = \frac{T_w}{\gamma(\gamma - 1)M_\infty^2}$$

Therefore,

$$(\Delta\rho_{et})_{i,1} = \rho_{i+1,1} \frac{T_{w(i+1)}}{\gamma(\gamma - 1)M_\infty^2} - \rho_{i,1} \frac{T_{w(i)}}{\gamma(\gamma - 1)M_\infty^2} \quad (4.9b)$$

For a uniform surface temperature, $T_{w(i+1)} = T_{w(i)} = T_w$. Therefore,

$$(\Delta\rho_{et})_{i,1} = \phi'(\rho_{i+1,1} - \rho_{i,1}) \quad (4.10a)$$

where ϕ' is defined as $\phi' = \frac{T_w}{\gamma(\gamma - 1)M_\infty^2}$. Equation (4.10a) may be rearranged as

$$\frac{1}{\phi'}(\Delta\rho_{et})_{i,1} = \rho_{(i+1,1)} - \rho_{(i,1)} \quad (4.10b)$$

or

$$\phi(\Delta\rho_{et})_{i,1} = \rho_{(i+1,1)} - \rho_{(i,1)} \quad (4.10c)$$

where

$$\phi = \frac{1}{\phi'} = \frac{\gamma(\gamma - 1)M_\infty^2}{T_w}$$

By definition, one may also write

$$(\Delta\rho)_{i,1} = \rho_{(i+1,1)} - \rho_{(i,1)} \quad (4.11)$$

Equation (4.10c) is subtracted from Eq. (4.11) to yield

$$(\Delta\rho)_{i,1} - \phi(\Delta\rho_{et})_{i,1} = \rho_{(i+1,1)} - \rho_{(i,1)} - (\rho_{(i+1,1)} - \rho_{(i,1)}) = 0$$

Thus, the required boundary conditions at the body for constant surface temperature can be summarized as

$$(\Delta\rho)_{i,1} - \phi(\Delta\rho_{et})_{i,1} = 0 \quad (4.12a)$$

$$(\Delta\rho u)_{i,1} = 0 \quad (4.12b)$$

$$(\Delta\rho v)_{i,1} = 0 \quad (4.12c)$$

$$(\Delta\rho w)_{i,1} = 0 \quad (4.12d)$$

$$\begin{aligned} & (\Delta\rho e_t)_{i,1} - \psi_{i+1} \left[\frac{1}{2} (u_{i,2}^2 + v_{i,2}^2 + w_{i,2}^2) (\Delta\rho)_{i,2} - u_{i,2} (\Delta\rho u)_{i,2} \right. \\ & \quad \left. - v_{i,2} (\Delta\rho v)_{i,2} - w_{i,2} (\Delta\rho w)_{i,2} + (\Delta\rho e_t)_{i,2} \right] \\ & = \frac{1}{\gamma - 1} (\psi_{i+1} - \psi_i) \frac{P_{i,2}}{J_{i,2}} \end{aligned} \quad (4.13)$$

where $\psi_{i+1} = \frac{J_{i+1,2}}{J_{i+1,1}} = \left(\frac{J_2}{J_1} \right)_{i+1}$.

At the outer boundary, a shock fitting technique is used and the flow variables behind the shock are calculated from the Rankine-Hugoniot relations. The plane of symmetry boundary conditions are computed by reflection and they are imposed explicitly as well as implicitly. In addition to the boundary conditions, initial conditions are also necessary. As mentioned earlier, near the nose tip the initial plane solution to initiate the marching procedure is provided by the Navier-Stokes equations.

4.2 Shock Fitting Procedure

The bow shock generated by a slender body in a supersonic/hypersonic flow field may be selected as the outer boundary of the domain and determined as a part of the overall solution. Obviously this procedure has some advantages compared to an outer boundary set at the free stream where the bow shock must be captured. First, the number of grid points in the domain may be decreased. This is due to the fact that additional grid points must be located in the free stream if the bow shock is to be captured. Second, shock smearing, which is a consequence of shock capturing, will not appear in the solution when shock fitting is used. Of course, these advantages are accompanied by some disadvantages. Most shock fitting procedures are explicit, and therefore some additional

stability requirements are imposed. Furthermore, additional sets of equations must be used to determine the shock location. Usually the Rankine-Hugoniot relations are used for this purpose.

The initial conditions at “i=1” provide all the required data including the shock slope. To generate the grid at the next station, i.e., at “i=2, the shock is linearly extrapolated. Therefore, the grid system at “i=2” is generated and the PNS equations are solved for j=1 (at the surface) to j=jmax (at the shock, i.e., jmax is the grid point just behind the shock). The finite difference form of the PNS equations are modified and a one sided difference approximation is employed at the shock. Once the PNS equations at “i=2” are solved, all the flow properties including the pressure are known. However, the shock location at “i=2” was extrapolated from the previous station. Therefore an updating procedure must be used to modify the shock properties and compute a new shock slope at “i=2”. The procedure is described in two steps. First, an equation for the shock shape is derived, and subsequently the Rankine-Hugoniot equations are introduced.

The shock standoff distance δ is obtained from the values at ξ through an Euler integration as [9]

$$\delta(\xi + \Delta\xi) = \delta(\xi) + \frac{\partial\delta}{\partial\xi}\Delta\xi \quad (4.14)$$

The problem is to determine the slope $\frac{\partial\delta}{\partial\xi}$ at the station ξ . The inward unit normal to the shock is given by

$$N_s = \frac{\vec{l}_i - \frac{\partial z}{\partial \zeta} \vec{j} + \frac{\partial y}{\partial \zeta} \vec{k}}{\sqrt{l^2 + \left(\frac{\partial y}{\partial \zeta}\right)^2 + \left(\frac{\partial z}{\partial \zeta}\right)^2}} \quad (4.15)$$

where

$$l = \frac{\partial\delta}{\partial\xi} \left(\frac{\partial z}{\partial \zeta} \cos \phi - \frac{\partial y}{\partial \zeta} \sin \phi \right) + \left(\frac{\partial z}{\partial \zeta} b_B - \frac{\partial y}{\partial \zeta} c_B \right)$$

and the derivatives with respect to ζ are taken along the shock. If V_1 denotes the upstream flow velocity normal to the shock, then

$$V_1^2 = \left(\vec{N}_s \cdot \vec{V}_\infty \right)^2 \quad (4.16)$$

Upon substituting for \vec{V}_∞ and \vec{N}_s , this equation can be solved for $\frac{\partial \delta}{\partial \xi}$ as

$$\frac{\partial \delta}{\partial \xi} = \frac{\left[u_\infty t_1 + v_1 \sqrt{t_2 t_3 + t_1^2} \right]}{(t_2 t_4)} - \frac{\partial r_b}{\partial \xi} \quad (4.17)$$

where

$$\begin{aligned} t_1 &= v_\infty \left(\frac{\partial z}{\partial \zeta} \right) - w_\infty \left(\frac{\partial y}{\partial \zeta} \right) \\ t_2 &= u_\infty^2 - V_1^2 \\ t_3 &= \left(\frac{\partial y}{\partial \zeta} \right)^2 + \left(\frac{\partial z}{\partial \zeta} \right)^2 \\ t_4 &= \cos \phi \left(\frac{\partial z}{\partial \zeta} \right) - \sin \phi \left(\frac{\partial y}{\partial \zeta} \right) \\ u_\infty &= \cos \alpha, \quad v_\infty = -\sin \alpha, \quad w_\infty = 0 \end{aligned}$$

The normal component of velocity behind the shock, V_1 and the density, ρ_1 are expressed by (Rankine-Hugoniot relations)

$$V_1 = \sqrt{\frac{\gamma+1}{2\gamma M_\infty^2} \left(\bar{P} + \frac{\gamma-1}{\gamma+1} \right)} \quad (4.18)$$

$$\rho_1 = \frac{\bar{P} + \frac{\gamma-1}{\gamma+1}}{1 + \bar{P} \left(\frac{\gamma-1}{\gamma+1} \right)} \quad (4.19)$$

where,

$$\bar{P} = \gamma M_\infty^2 P_1$$

The pressure behind the shock P_1 can be calculated by the application of a one-sided version of the finite difference algorithm, once the new shock position is determined.

The metric coefficient $\frac{\partial\eta}{\partial a}$ is obtained by differentiating Eq. (4.8)

$$\frac{\partial\eta}{\partial a} = \frac{2\beta}{\left\{ \beta^2 - \left(\frac{\delta-s}{\delta} \right)^2 \right\} \ln\left(\frac{\beta+1}{\beta-1}\right)} \frac{s}{\delta^2} \left(\frac{\partial\delta}{\partial\xi} - \frac{\delta}{\xi} \right) \quad (4.20)$$

Chapter 5

RESULTS AND DISCUSSION

The numerical schemes described in Chap. 4 were used to obtain results for two different geometries, slender blunted cones and on-axis biconics. All calculations were performed under the assumption of a laminar flow and perfect gas. For the forebody, the flow is calculated by the parabolized Navier-Stokes equations with the starting solution for the nose section provided by the full Navier-Stokes equations. The parametric studies were conducted to determine the effect of nose bluntness and AOA on surface quantities and flow field variables for straight biconics. The effect of AOA on surface quantities and shock stand-off distance for a blunted cone was also investigated to check the PNS code. The freestream conditions for the blunted cone and on-axis biconic considered for this study are given in Tables 5.1 and 5.2 respectively. These conditions were obtained from [10].

The results for slender blunted cone are presented first and this is followed by the results for the straight biconic. The results obtained for the biconic configuration are subdivided into several subsections, and these are presented in a somewhat logical order.

5.1 Results for Slender Cone

The effect of nose bluntness on flow field and surface quantities was investigated extensively in [2, 19] for blunted slender cones and ogives at $\alpha=0^\circ$. Here , selected results obtained for $\alpha=0^\circ$ and 2° are presented to demonstrate the influence of AOA on different quantities.

Figures 5.1–5.4 show the variation of surface quantities with the axial distance for a 5° cone at 0° and 2° AOA for freestream Mach number 20. The Reynolds number

Table 5.1 Freestream flow conditions for 5° cone, $\alpha=0^\circ$ and 2°

Quantity	$M_\infty = 20$
P_∞ , N/m ²	171.0
T_{wall} , k	1000
T_∞ , k	261.3
Pr	0.72
$Re(R_n)$	22303
R_n , m	0.025
γ	1.4

Table 5.2 Freestream flow conditions for $12.87^\circ / 7^\circ$ bicone; $\alpha=0^\circ$, 8° and 12°

Quantity	$M_\infty = 6.89$
P_∞ , N/m ²	2182
T_{wall} , k	300
T_∞ , k	1604
Pr	0.72
Re_∞	4.5×10^5
R_n , m	0.00383
γ	1.3

$Re (R_n)$ considered is based upon the nose radius. The nose radius considered is $R_n=0.025$ m. A ray at $\phi=0^\circ$ is considered to be most windward and the one at $\phi=180^\circ$ is considered to be most leeward.

The surface pressure distributions are presented in Fig. 5.1. The pressure has been non-dimensionalized with respect to the freestream value. The x distance is measured from the virtual tip of the cone. The results are plotted from the tangency point onward. Consider the incoming flow at 0° incidence, in the stagnation region, the pressure is very high but as the flow moves downstream, the shock strength decreases, thereby decreasing the pressure. The high pressure flow continues to expand along the cone frustum producing a favorable pressure gradient as evident from the figure. The favorable pressure gradient region for present conditions extends to about $x=60 R_n$. However, by now the flow has overexpanded and must recompress in order to attain the conical wall pressure value far downstream of the nose. This recompression then results in an adverse pressure gradient region. The extent of overexpansion and recompression is a function of bluntness and freestream conditions. The surface pressure reaches the conical value at about $x=160 R_n$.

At Mach 20, even if the incoming flow is at small incidence $\alpha=2^\circ$, it has significant effects on surface pressure on windward and leeward planes. For the windward plane the favorable pressure gradient extends to about $x=48 R_n$. The pressure attains a constant value at about $x=188 R_n$, which is approximately 66% higher than the conical value at $\alpha=0^\circ$. On the leeward plane, the favorable pressure gradient extends to about $x=84 R_n$. The overexpanded flow compresses very slightly and almost becomes constant at approximately $x=136 R_n$. This is about 63% lower than the conical value at $\alpha=0^\circ$. On the sideward meridian $\phi=90^\circ$, the surface pressure behaves in the same fashion as at 0° AOA.

Figure 5.2 shows the variation of shock stand-off distance as a function of the axial distance. The shock stand-off distances are measured from the body surface. The shock stand-off distance is nondimensionalized with respect to nose radius. At 0° AOA,

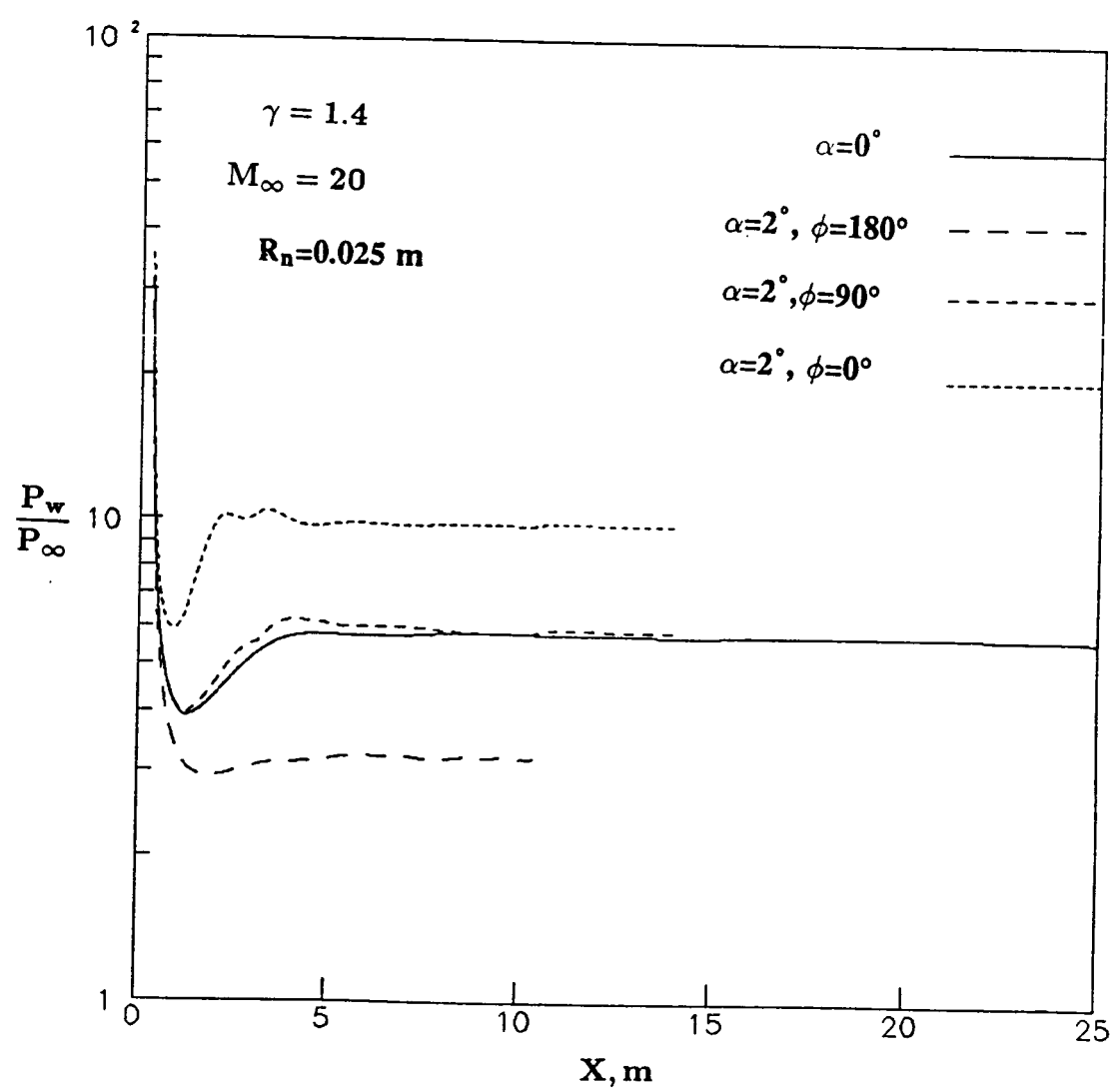


Fig. 5.1 Variation of wall pressure with axial distance for blunted cone at 0° and 2° AOA.

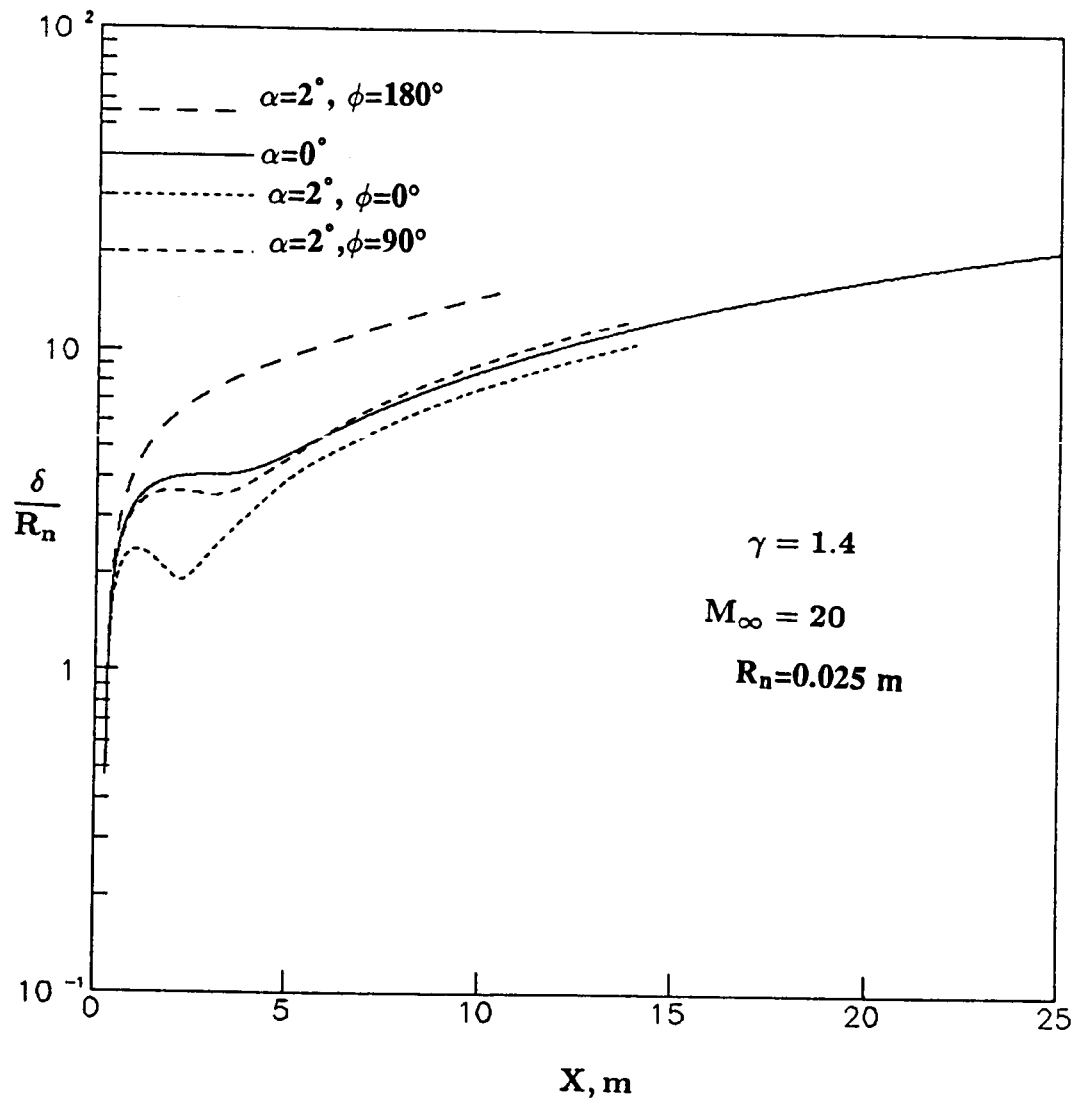


Fig. 5.2 Variation of shock standoff distance with axial distance for blunted cone at 0° and 2° AOA.

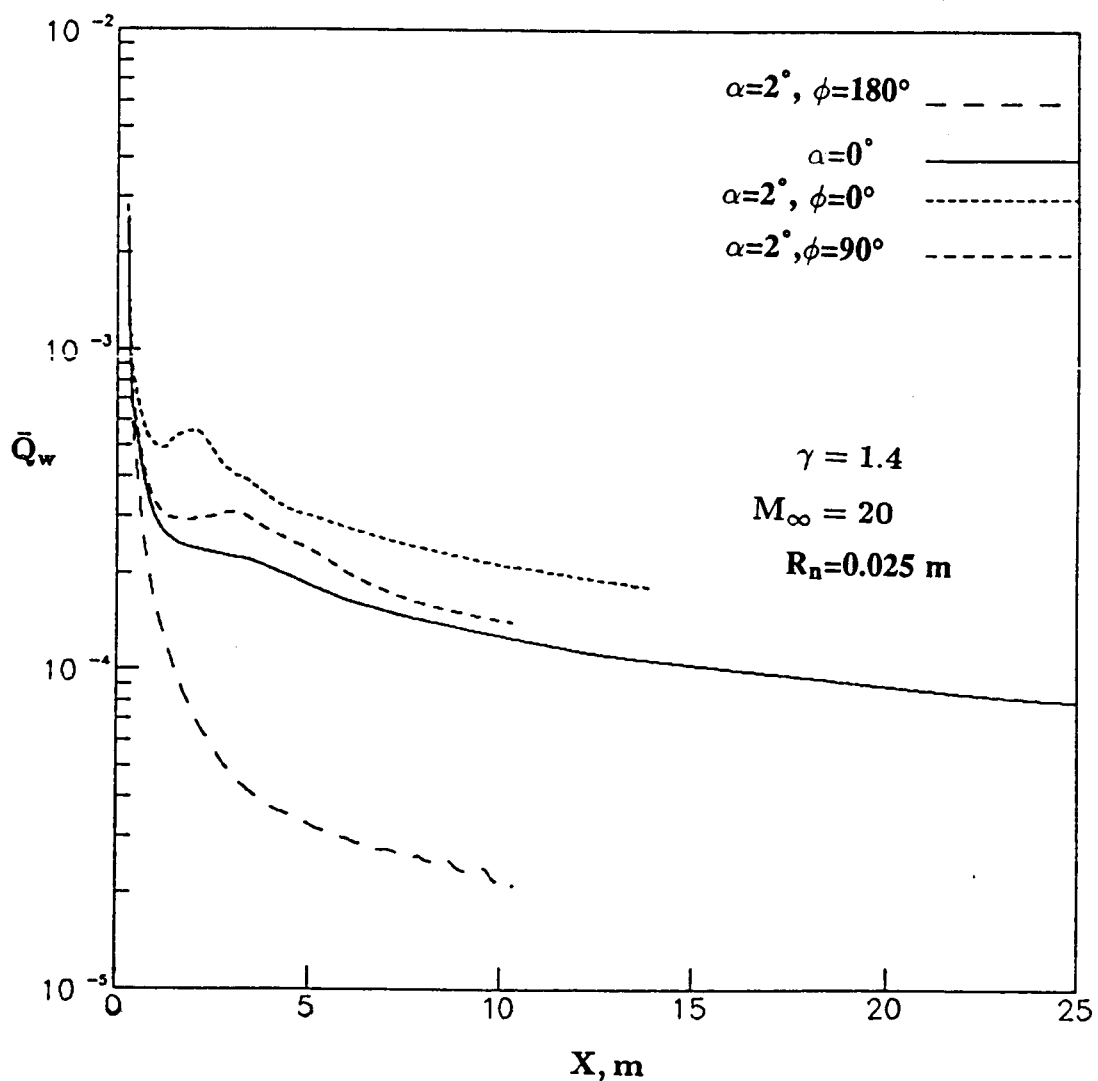


Fig. 5.3 Variation of wall heat transfer with axial distance for blunted cone at 0° and 2° AOA.

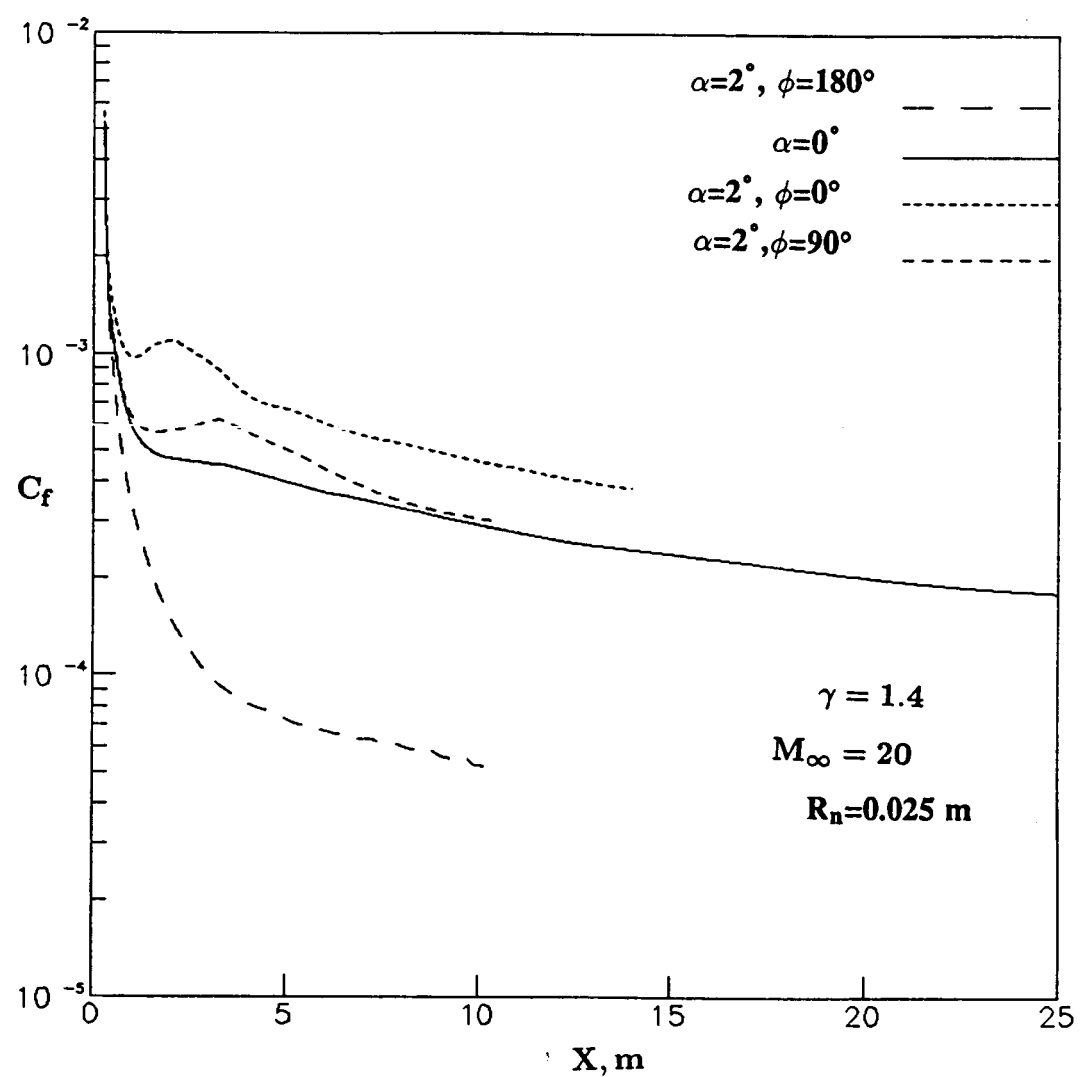


Fig. 5.4 Variation of skin friction coefficient with axial distance for blunted cone at 0° and 2° AOA.

the point of inflection occurs at about 170 nose radii downstream. At 2° AOA the shock gets displaced towards the leeward meridian. On the leeward side the shock is totally curved and inflection point disappears. On the windward side the shock gets compressed and the measured stand-off distances fall below the 0° AOA case. On the windward meridian the inflection point is about $96 R_n$ downstream. On the sideward plane ($\phi=90^\circ$) the shock shape lies very close to 0° AOA curve.

The variation of wall heat flux with axial distance is illustrated in Fig. 5.3. The wall heat flux has been nondimensionalized by $\rho_\infty V_\infty^3$. The heating rates are very high in the nose region and decrease continuously over the afterbody due to lower pressure. Because of the favorable and adverse pressure gradients near the nose region, the heat flux variation show a similar behavior to that of the surface pressure. Even at small incidence ($\alpha=2^\circ$), the wall heat flux increases on the windward plane considerably. On the leeward side there is a large decrease in the heat flux in comparison to 0° AOA case. On the sideward plane ($\phi=90^\circ$ and $\alpha=2^\circ$) the heating rates are little higher as compared to the $\alpha=0^\circ$ case.

Variation of skin friction coefficient with axial distance at 0° and 2° AOA is shown in Fig. 5.4. It follows the same general trend as the wall heat flux. This similarity can be explained qualitatively on the basis of Reynolds analogy. The skin friction on the leeward side decreases by an order of magnitude compared to the windward side at $\alpha=2^\circ$. The reason is that , on the leeward side, the entropy and boundary layers are very thick, and gradients of velocity near the wall are small.

5.2 Results for the Straight Biconic

The various results obtained for $12.84^\circ/7^\circ$, straight biconic configuration are presented in this section. All the results were obtained for a freestream Mach number of 6.89, $\gamma=1.3$, cold wall condition ($\frac{T_w}{T_\infty} = 0.187$) and the free stream Reynolds number per unit length, $Re_\infty = 4.5 \times 10^5$ (Table 5.2). For numerical calculations, the Reynolds

number based on nose radius was considered. Two nose radii were considered to study the bluntness effects; $R_n=0.00383$ m and 0.04 m. The AOA was varied from 0° to 8° and 12° to study its influence on the flow field and surface quantities.

5.2.1 Experimental Verification

A few important results obtained by PNS code are validated by the experimental results of Miller et al. [10] for the same geometry and freestream conditions. Figure 5.5 shows the variation of wall heat flux Q_w (MW/m^2) as a function of nondimensionalized axial distance at $\alpha=0^\circ$. The experimental result is accurately predicted by the PNS code. Figure 5.6 shows the variation of Q_w with x/L at 12° AOA. The PNS code slightly underpredicts the windward and leeward heating. This is due to the fact that at $\alpha=12^\circ$, the boundary layer is thinner on windward side which requires more number of grid points to accurately model the temperature distribution through the boundary layer. Also the flow separates on the leeward side.

5.2.2 Nose Bluntness Effects

The effect of nose bluntness on wall quantities at 0° and 12° AOA are presented in Figs. 5.7–5.14. The results shown in Figs. 5.7–5.11 correspond to $\alpha=0^\circ$. Figure 5.7 shows the variation of nondimensionalized surface pressure, $\frac{P_w}{P_\infty}$ with dimensional axial distance, X in meters. There is no appreciable change in surface pressure even if the nose bluntness is increased by one order of magnitude for the present biconic geometry.

In Fig. 5.8 the effect of nose bluntness on wall heat flux Q_w (MW/m^2) is shown. If the nose bluntness is increased by an order of magnitude, heating on the fore-cone section decreases four times and approximately two times on the aft-cone section. This behavior was also observed for the skin friction coefficient which is shown in Fig. 5.9.

In Fig. 5.10 the variation of dimensional shock stand-off distance δ , in meters as a function of dimensional axial distance X, in meters at $R_n = 0.00383$ m and 0.04 m are

shown. Blunting of the sharp nose, causes an increase in the shock stand-off distance by an order of magnitude.

Figures 5.11–5.14 correspond to $\alpha=12^\circ$. The surface pressure variation for leeward and windward meridian is shown in Fig. 5.11 and the result looks similar to $\alpha=0^\circ$ case. The bluntness effect on fore-cone and aft-cone heating is presented in Fig. 5.12. The fore-cone heating is more sensitive to nose bluntness than aft-cone heating. Heating on the most windward ray decreases by four times for the fore-cone section and about two times for the aft-cone section. Heating on the most leeward ray decreases by five times for the fore-cone section, but there is a little change for aft-cone heating. The bluntness effect on skin friction coefficient shown in Fig. 5.13 is analogous to wall heat flux. In Fig. 5.14, the dimensional shock shape r_{sh} , m is plotted as a function of dimensional axial distance X , m. The two sets of curves correspond to $R_n=0.00383$ m and 0.04 m, respectively. The distance r_{sh} is measured from the axis of the biconic. The leeward and windward shock shapes increase by an order of magnitude with the increase in nose bluntness.

Figures 5.15–5.17 represent the circumferential variation of wall quantities at 0° , 8° , and 12° AOA. These curves are plotted for nose bluntness, $R_n=0.00383$ m and axial location $x/R_n=18.016$. Figure 5.15 shows the variation of the coefficient of pressure, C_p , with meridian angle ϕ . It is seen that the value of C_p increases on the windward side and decreases on the leeward side with increase in AOA. The value of C_p is maximum on the windward side ($\phi=0^\circ$) and decreases monotonically towards the leeward side ($\phi=180^\circ$). At 0° AOA, C_p remains constant in the circumferential plane. The circumferential plot of wall heat transfer (Fig. 5.16) and skin friction coefficient (Fig. 5.17) exhibit a similar behavior as the coefficient of pressure.

In Figs. 5.18 and 5.19, the circumferential variation of C_p and wall heat transfer are shown at 0° and 12° AOA for $R_n=0.04$ m and axial distance $x/R_n=30.89$. In Fig. 5.18 the value of C_p starts increasing slightly on the leeward side between $\phi=150^\circ$ to $\phi=180^\circ$.

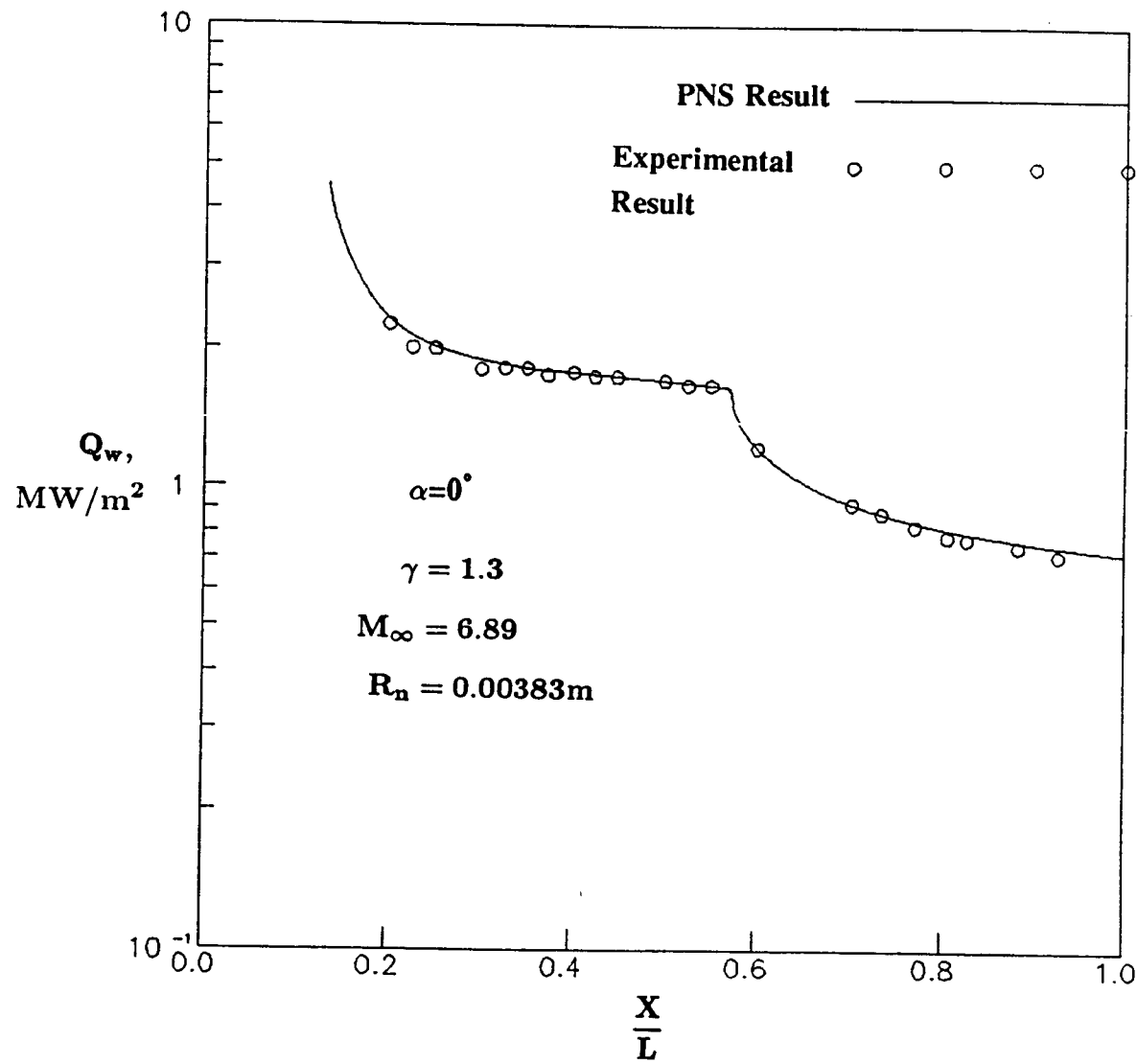


Fig. 5.5 Comparison of experimental and numerical results of variation of wall heat flux with axial distance for straight biconic at 0° AOA.

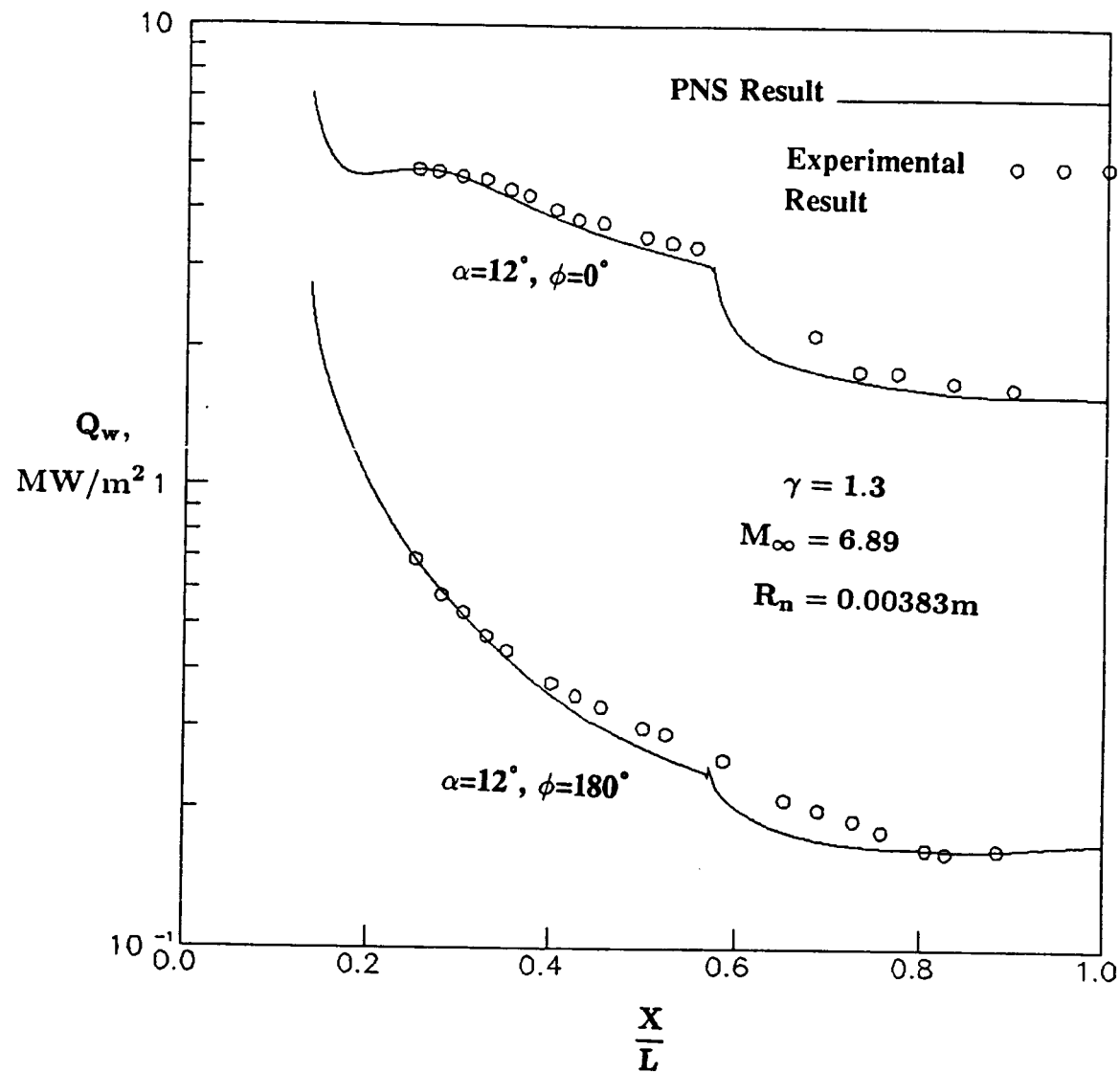


Fig. 5.6 Comparison of experimental and numerical results of variation of wall heat flux with axial distance for straight biconic at 12° AOA.

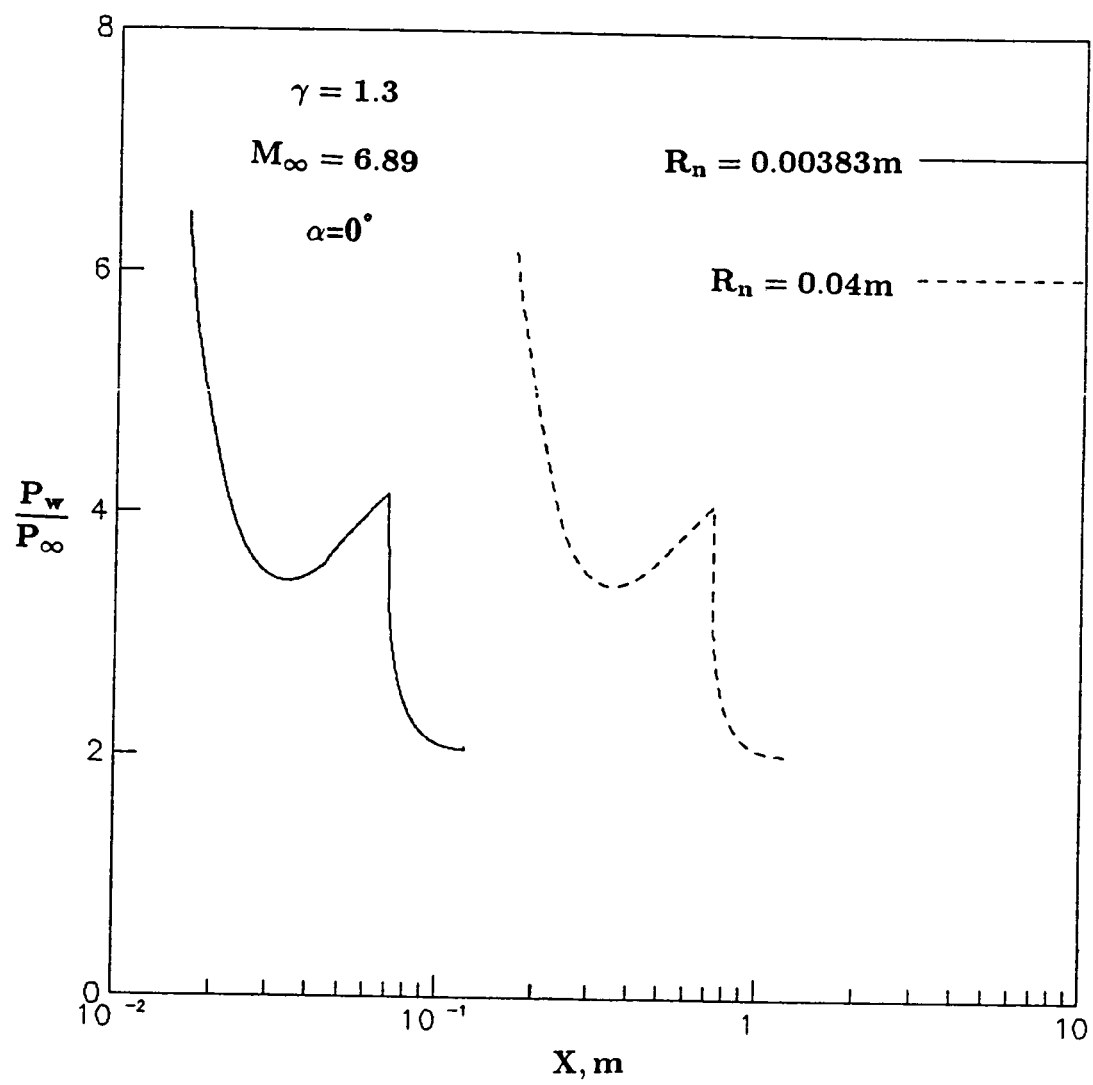


Fig. 5.7 Effect of nose bluntness on surface pressure for on-axis biconic at 0° AOA.

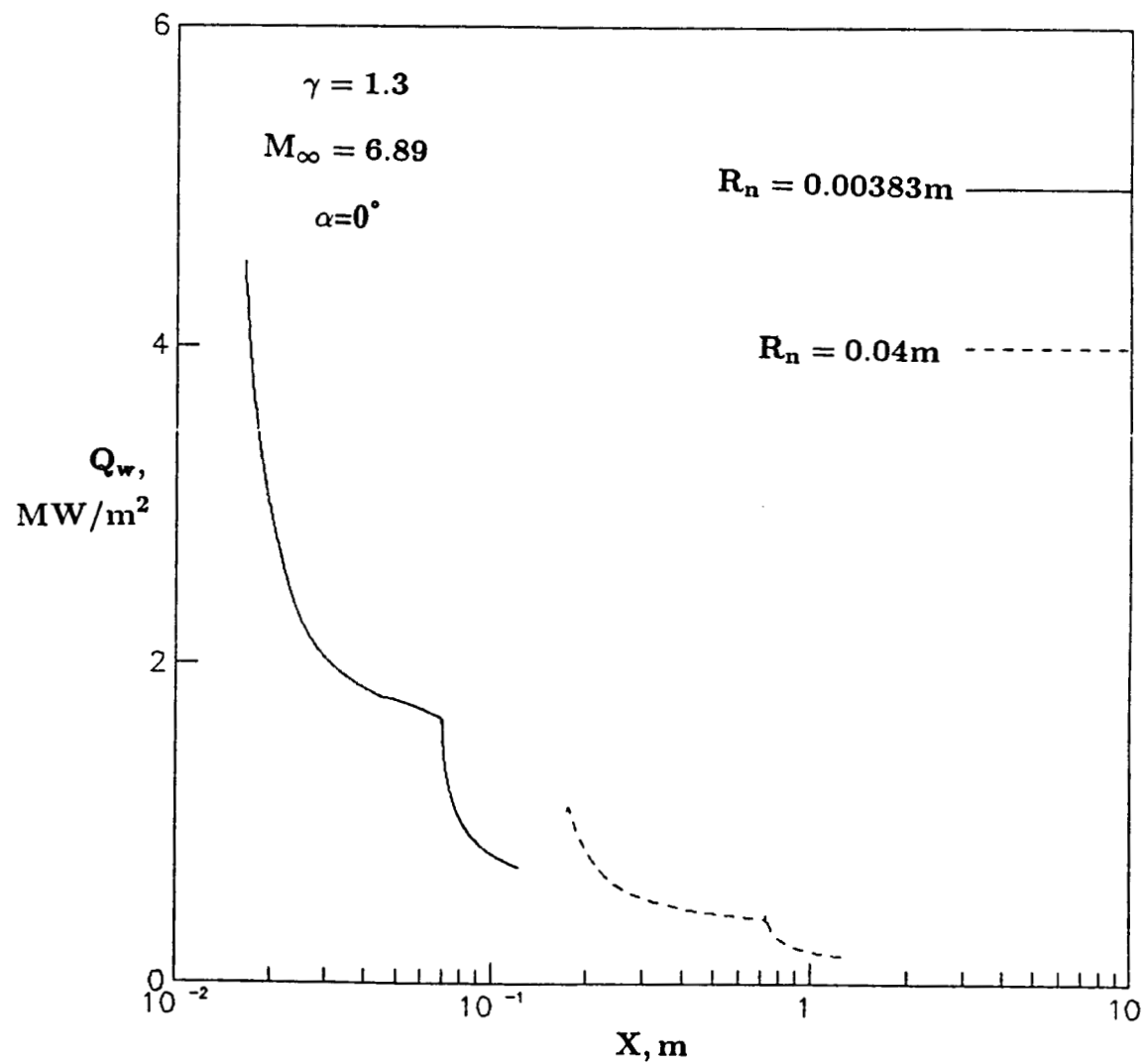


Fig. 5.8 Effect of nose bluntness on wall heat transfer for on-axis biconic at 0° AOA.

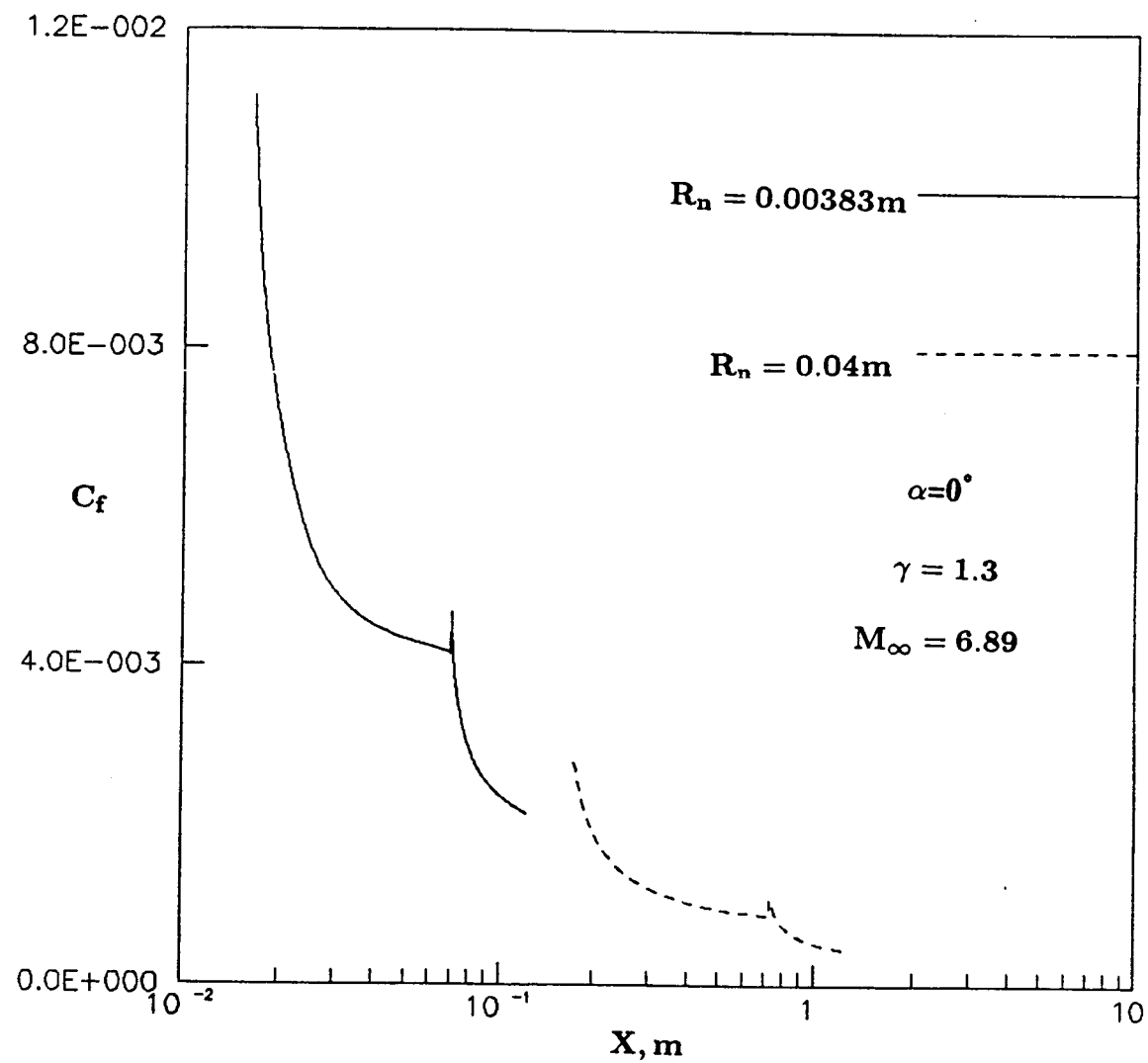


Fig. 5.9 Effect of nose bluntness on skin
friction coefficient for on-axis biconic at 0° AOA.

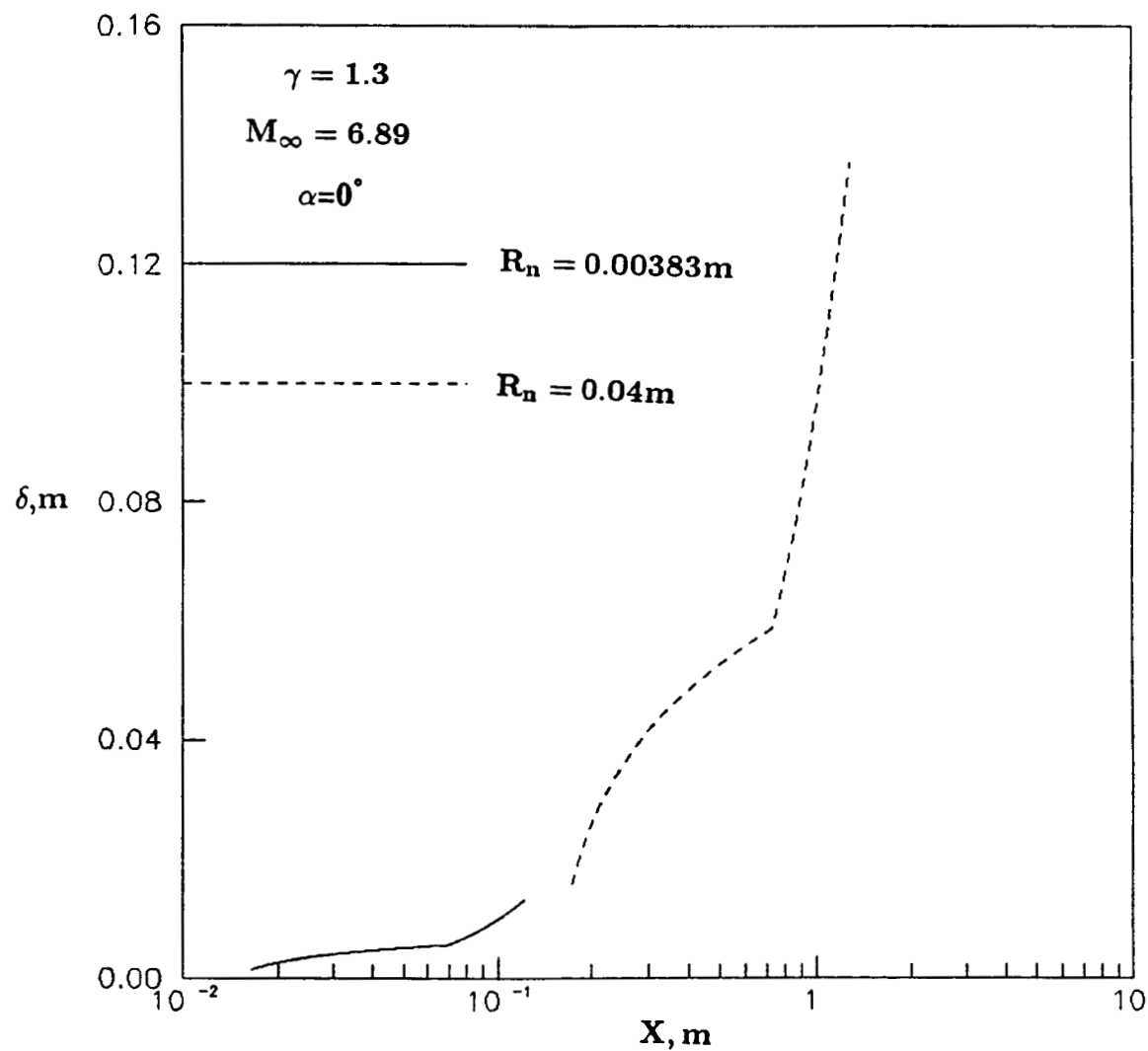


Fig. 5.10 Effect of nose bluntness on shock stand-off distance for on-axis biconic at 0° AOA.

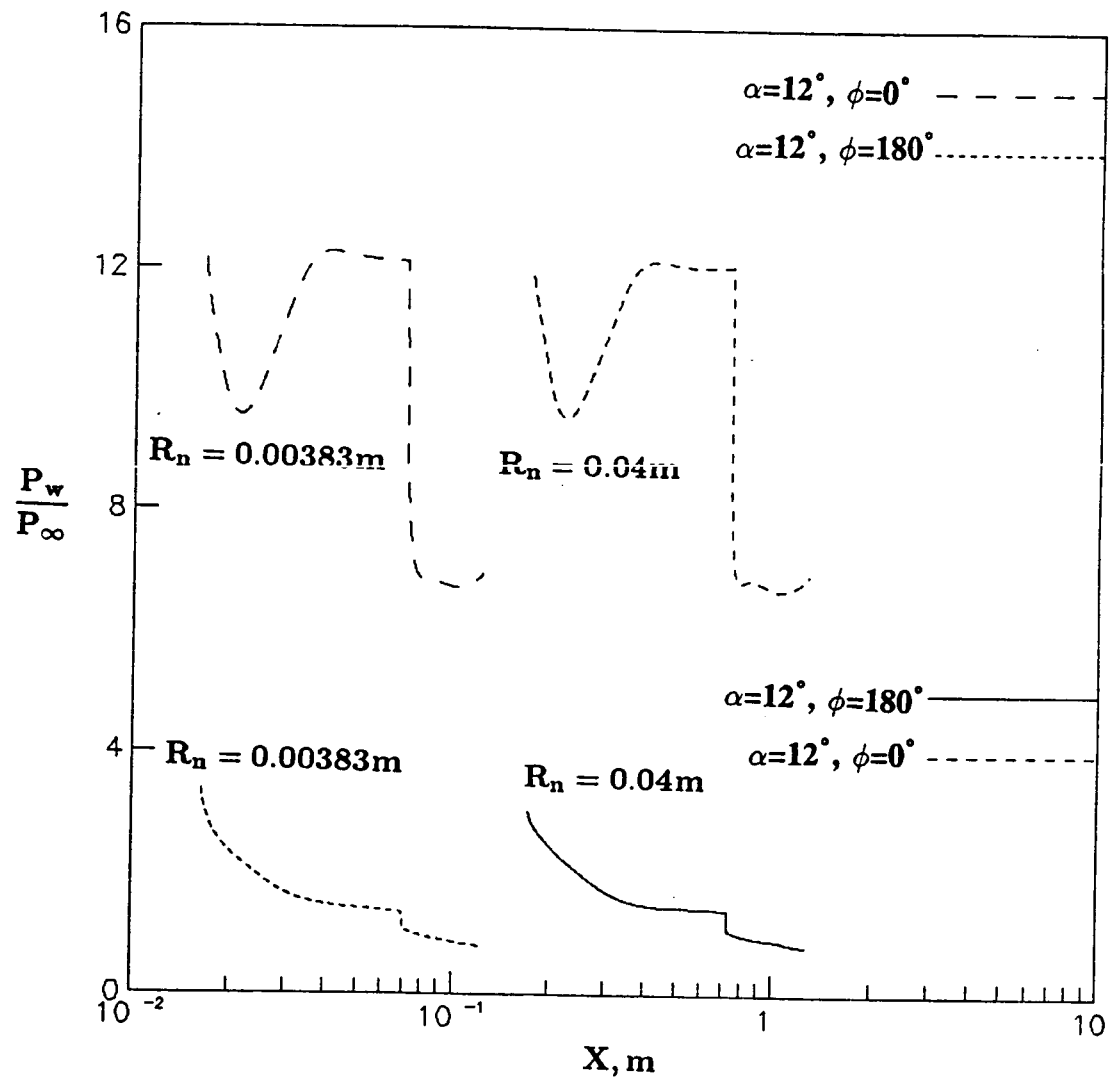


Fig. 5.11 Effect of nose bluntness on surface pressure for on-axis biconic at 12° AOA.

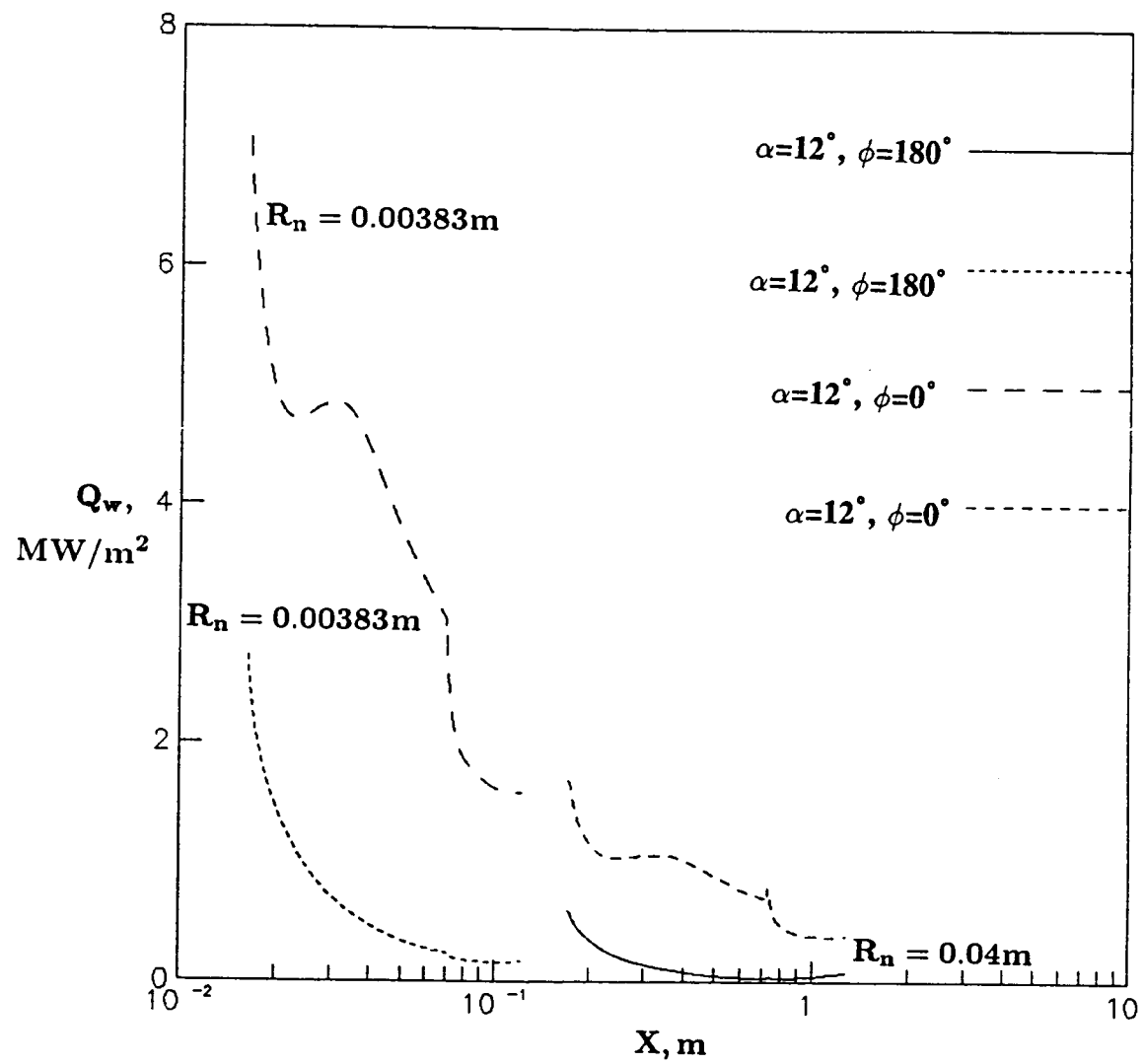


Fig. 5.12 Effect of nose bluntness on wall heat transfer for on-axis biconic at 12° AOA.

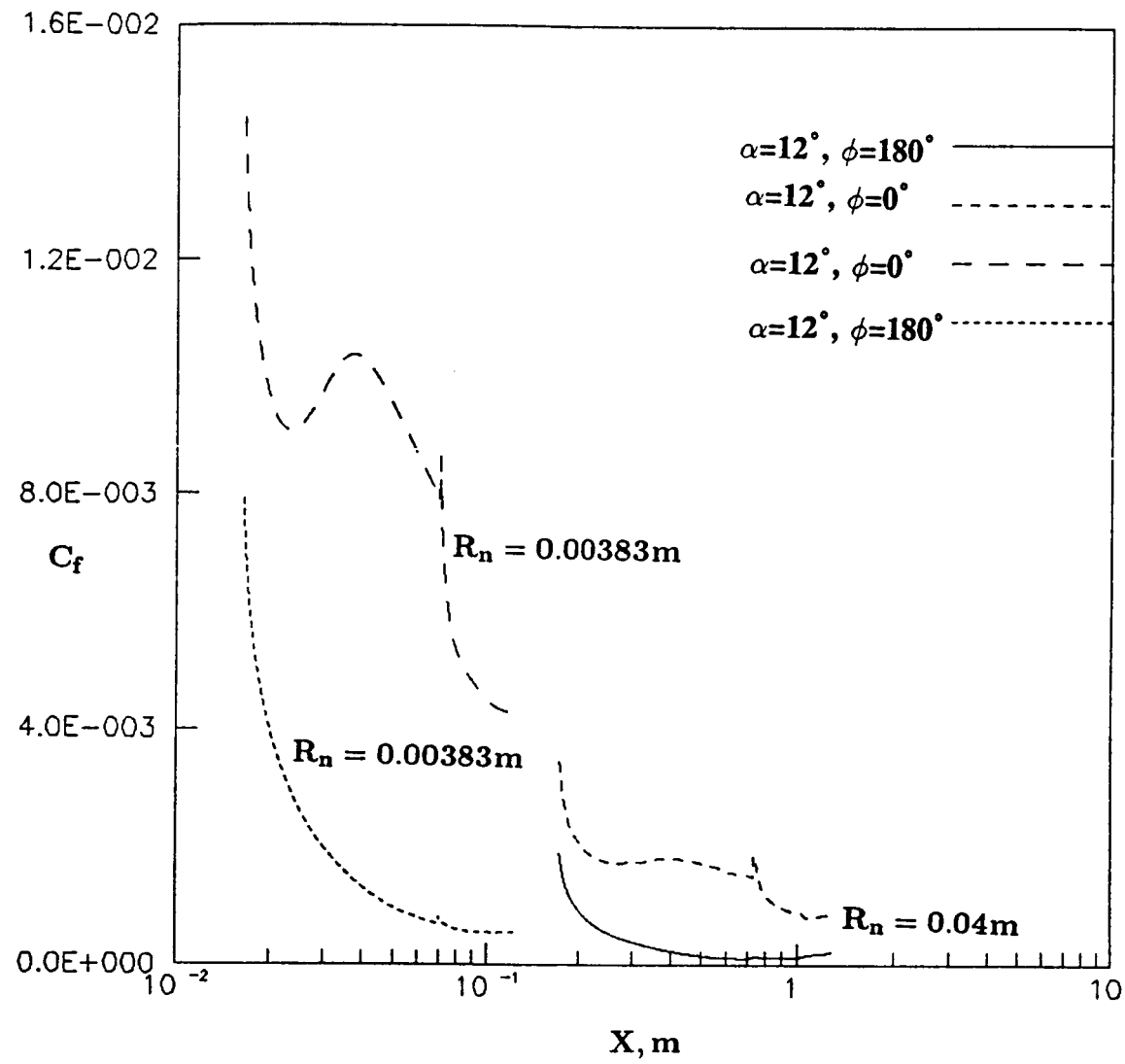


Fig. 5.13 Effect of nose bluntness on skin friction coefficient for on-axis biconic at 12° AOA.

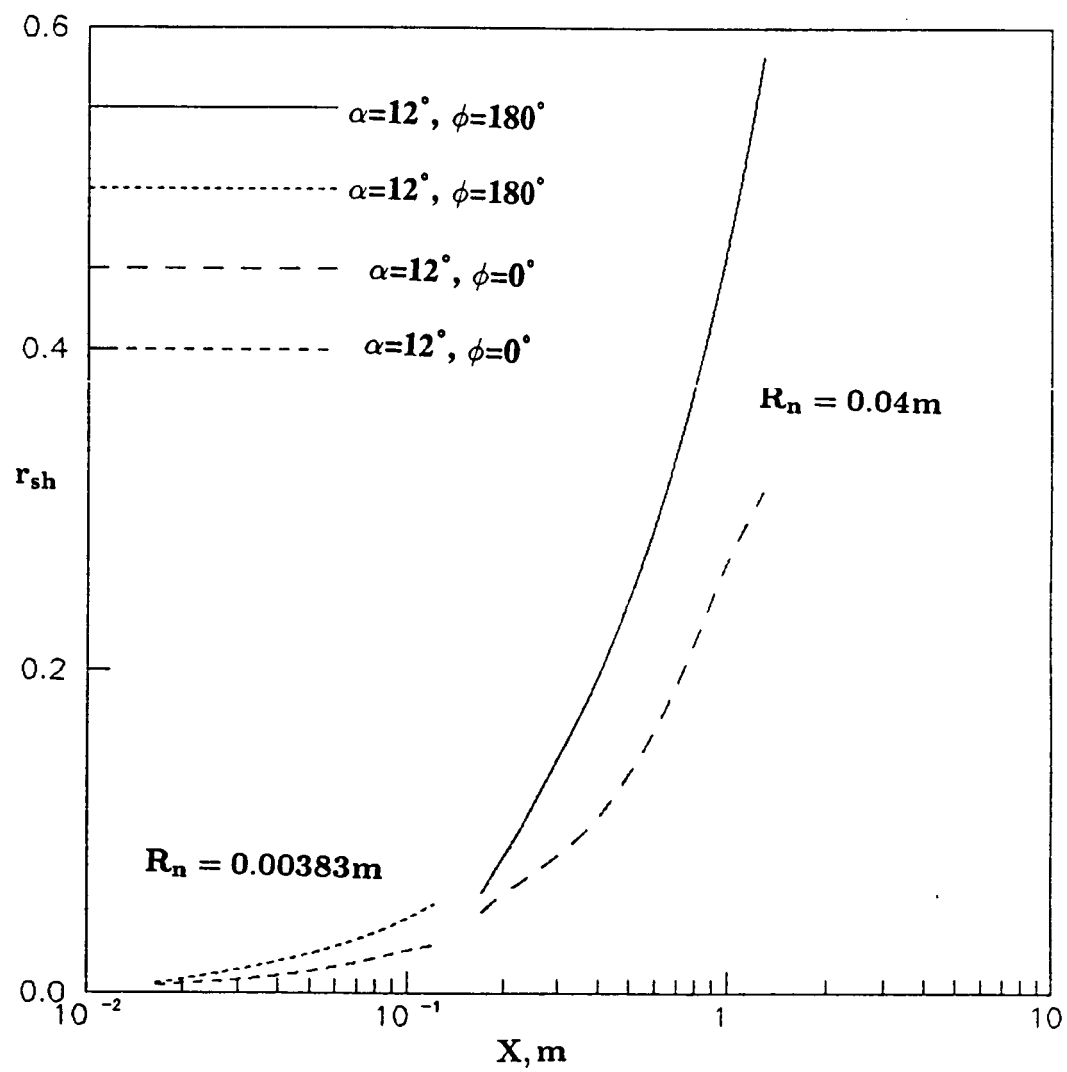


Fig. 5.14 Effect of nose bluntness on shock shape for on-axis biconic at 12° AOA.

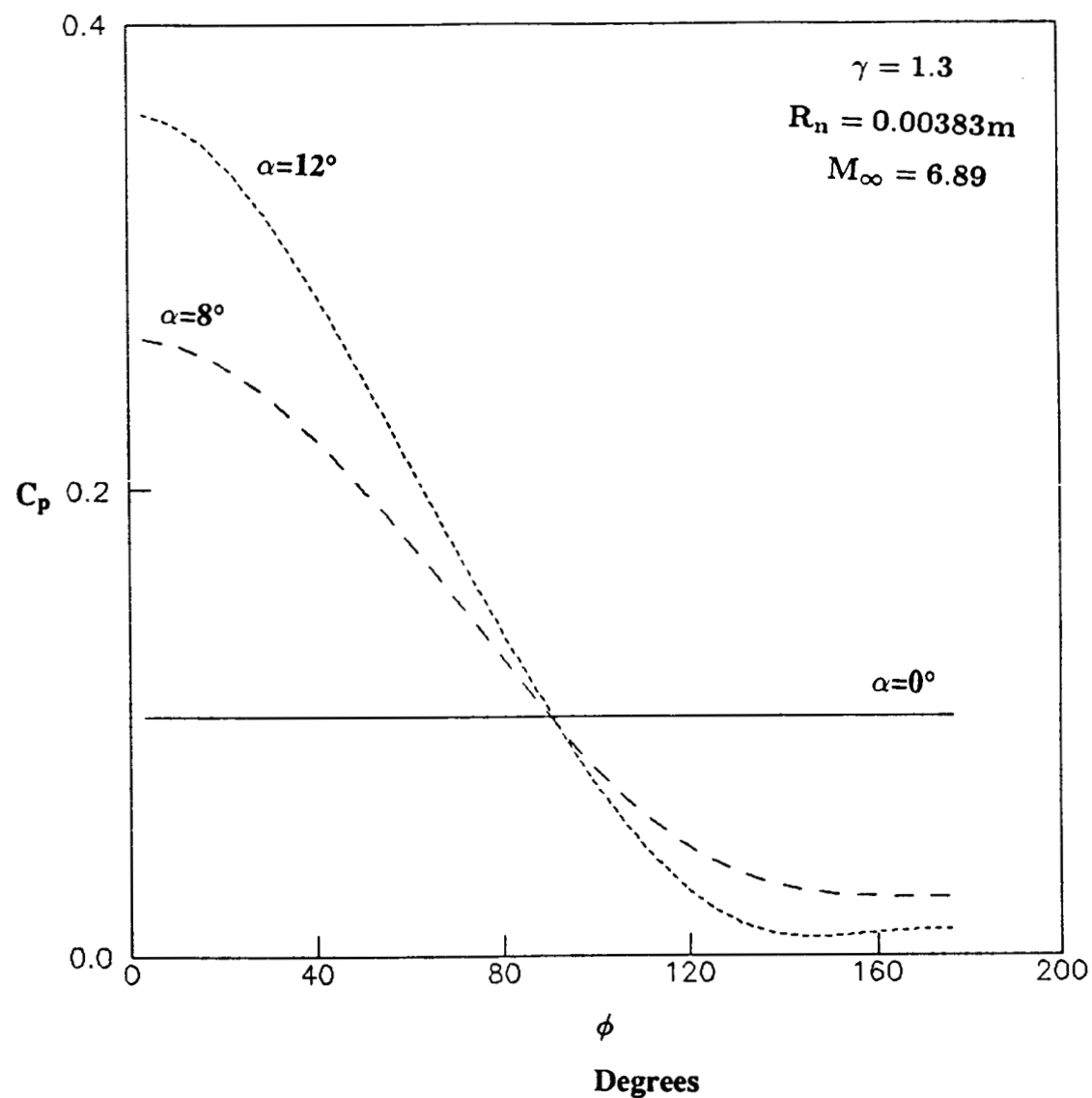


Fig. 5.15 Circumferential variation of coefficient of pressure
for on-axis biconic at 0° , 8° and 12° AOA, $x=18.016 R_n$.

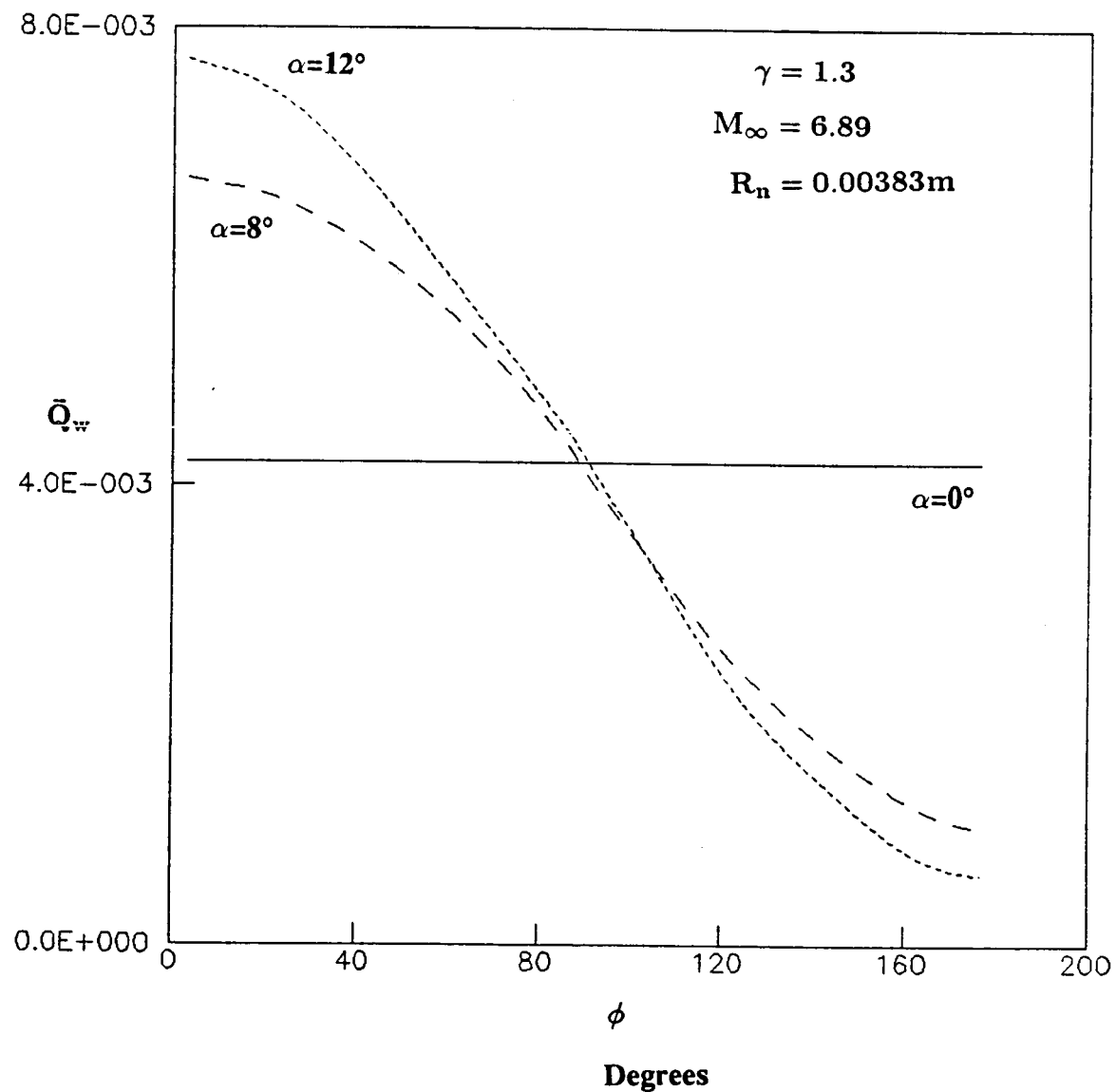


Fig. 5.16 Circumferential variation of wall heat transfer
for on-axis biconic at 0° , 8° and 12° AOA, $x=18.016 R_n$.

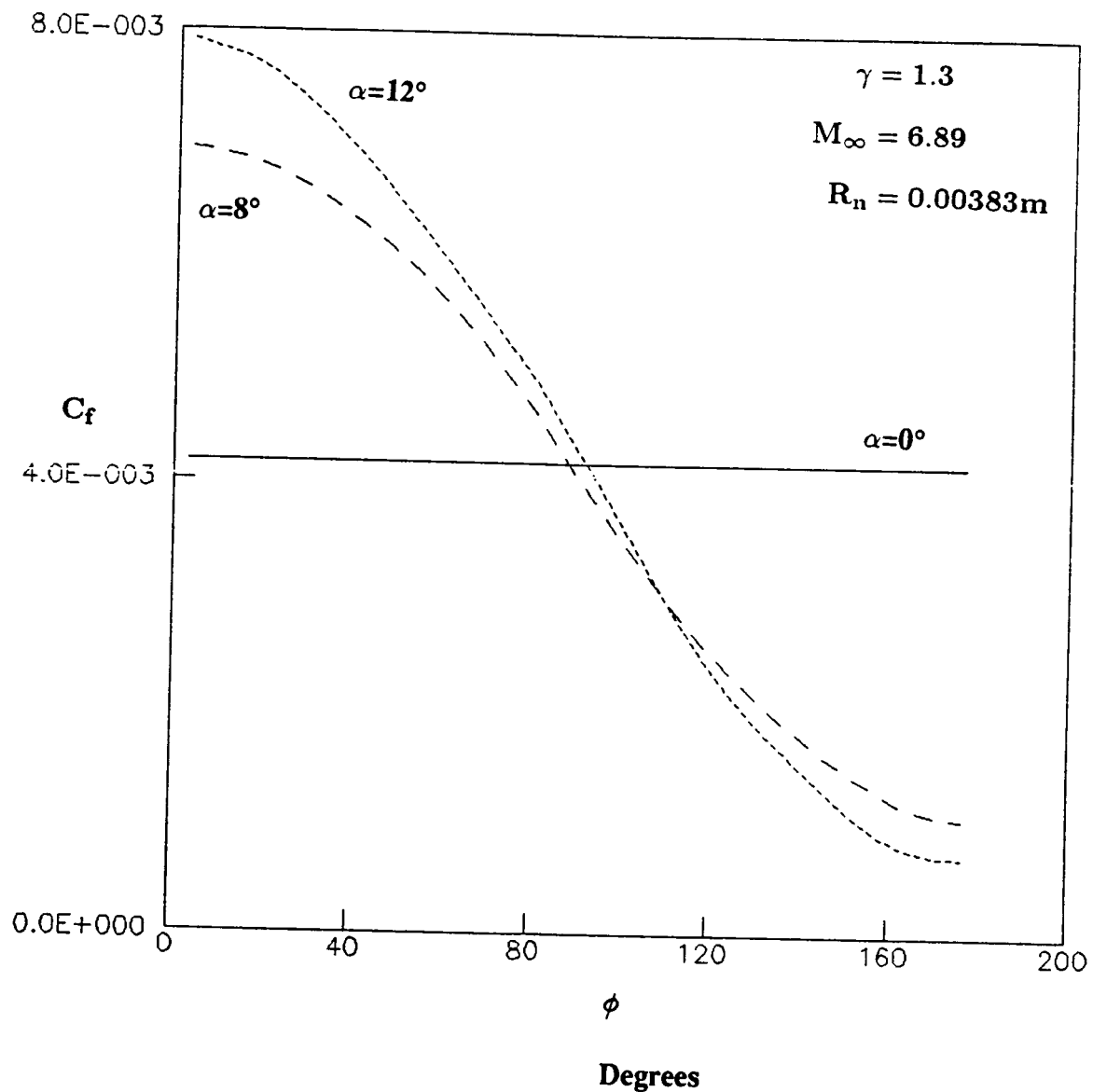


Fig. 5.17 Circumferential variation of skin friction coefficient
for on-axis biconic at 0° , 8° and 12° AOA, $x=18.016 R_n$.

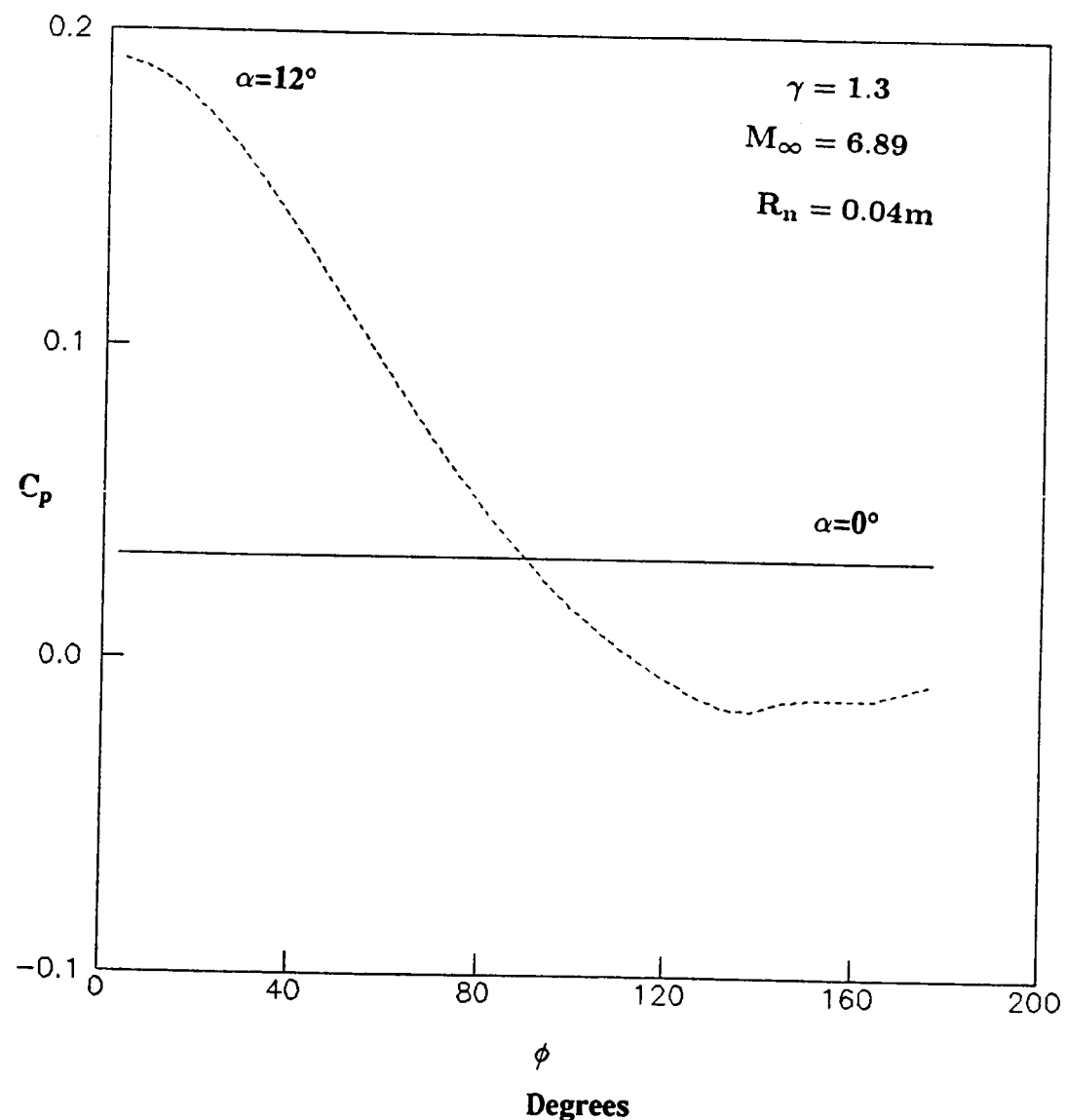


Fig. 5.18 Circumferential variation of coefficient of pressure for on-axis biconic at 0° and 12° AOA, $R_n = 0.04$ m, $x = 30.89 R_n$.

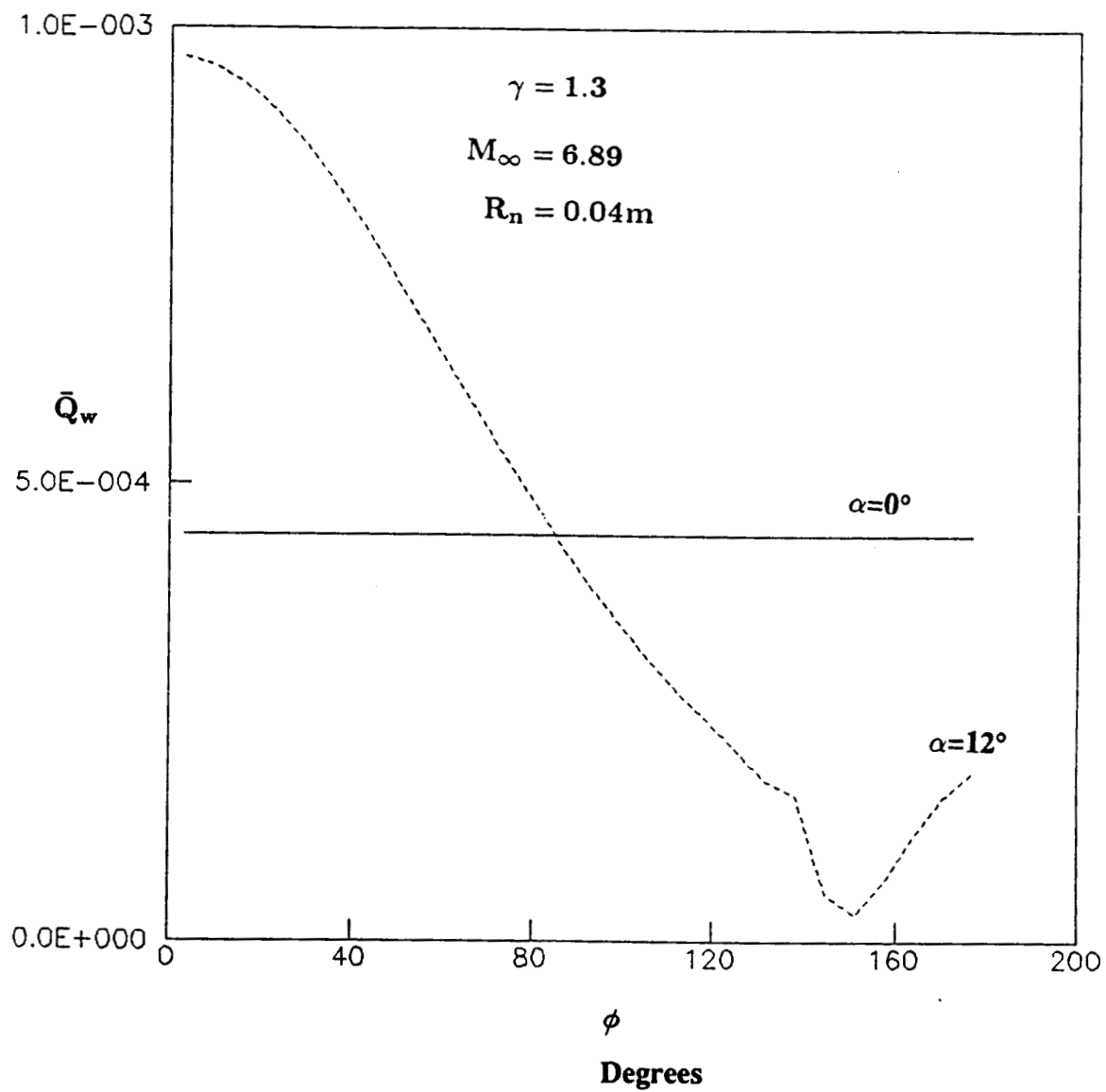


Fig. 5.19 Circumferential variation of wall heat transfer for on-axis biconic at 0° and 12° AOA, $R_n = 0.04\text{ m}$, $x = 30.89 R_n$.

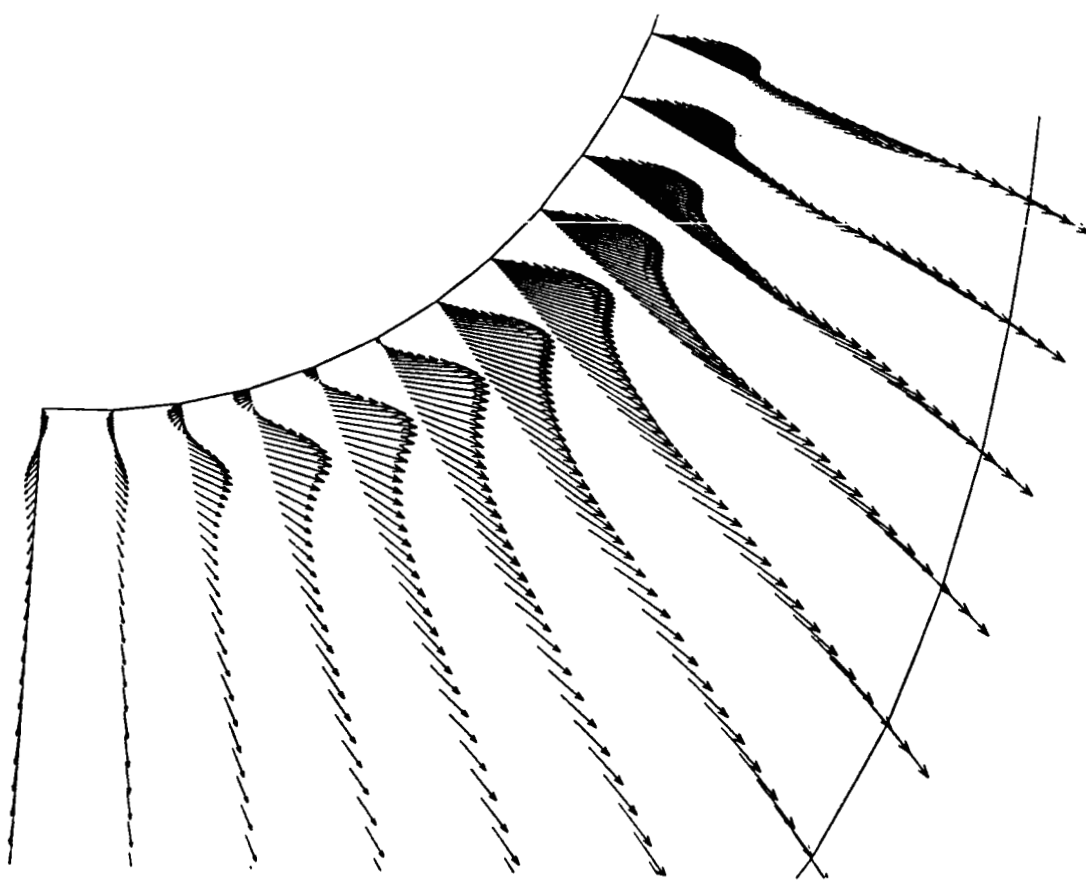


Fig. 5.20 Cross flow velocity vector plot for on-axis
biconic at 12° AOA, $R_n = 0.04$ m, $x = 30.89 R_n$.

The circumferential plot of Q_w (Fig. 5.19), follows the usual monotonic trend upto $\phi=140^\circ$, after that there is a sudden decrease in the value, and between $\phi=150^\circ$ to $\phi=180^\circ$ the value of Q_w starts increasing. As mentioned earlier this peculiar behavior is observed due to flow separation and formation of vortices on the leeward side. The flow separation in the cross flow plane can be observed clearly in Fig. 5.20 which shows the velocity vector plot in the circumferential plane.

5.2.3 Effects of Angle of Attack

Figures 5.21–5.30 show the variation of surface quantities with axial distance for on-axis biconic ($12.84^\circ / 7^\circ$) at different angles of incidence for free stream Mach number 6.89. In Figs. 5.21–5.25 the nose radius is 0.00383 m. Figure 5.21 shows the surface pressure distribution at 0° , 8° and 12° AOA. The surface pressure is nondimensionalized by the free stream static pressure P_∞ and plotted as a function of x/L . The variation of the windward surface pressure with x/L for the on-axis biconic illustrates the overexpansion of the flow from the spherical nose to the fore-cone section and the expansion of flow from fore-cone to aft-cone section. The region of this overexpansion-recompression of the windward flow from the nose diminishes with increasing AOA (effective cone half angle, which is equal to $\theta_c + \alpha$). The windward surface pressure distribution increases with AOA. At $\alpha=8^\circ$ the surface pressure is nearly constant for $0.36 \leq x/L \leq 0.57$ and at $\alpha=12^\circ$ for $0.28 \leq x/L \leq 0.57$. At the fore-cone aft-cone junction the pressure drops suddenly due to discontinuity, expands a little and then attains almost a constant value. At 8° and 12° AOA the surface pressure on the leeward side decreases monotonically on the fore-cone and aft-cone regions. With increasing AOA the surface pressure distribution on the leeward side decreases as is evident from the figure.

Figure 5.22 shows the variation of wall heat transfer (MW/m^2) distribution with the axial distance which has been nondimensionalized by the total length of the biconic at 0° , 8° and 12° AOA. Heating on the windward ray increases with AOA for the straight

biconic geometry. Leeward heating for the on-axis biconic decreases as α is increased. However, at $\alpha=12^\circ$ on the aft section the heating rate first decreases and then slightly increases. This can be attributed to the flow separation at high AOA and formation of vortices.

The variation of skin friction coefficient with nondimensionalized axial distance is shown in Fig. 5.23 for the straight biconic at 0° , 8° and 12° AOA. Skin friction coefficient behaves in the same way as wall heat transfer.

Figure 5.24 shows the variation of shock stand off distance with nondimensionalized axial distance x/L for the on-axis biconic at various angles of attack. As it is evident from the figure that, an inflection in the shock downstream of the spherical nose occurs on the windward side at 8° and 12° AOA. With increase in AOA the point of inflection shifts towards the nose section. The shock standoff distance on the leeward side is more sensitive to AOA than on the windward side. For straight and bent biconic geometry, Miller et al. [1] has given an empirical relation to measure shock standoff detachment distance on leeward side at the junction of aft-fore cone sections. On the leeward side the inflection point disappears. At 0° incidence the shock standoff distance increases more rapidly after the fore-cone aft-cone junction. This behavior is also observed on the windward side at 8° and 12° AOA. However, at 12° AOA, the shock standoff distance reach almost a constant value far downstream of the aft section. On the leeward side the shock stand off distance increases more linearly as the flow is marched downstream of the nose region.

Figure 5.25 shows the shock shape at 8° and 12° AOA for the straight biconic geometry. From the figure it is evident that on the leeward meridian the shock shape is more sensitive to AOA as compared to the windward meridian.

Figures 5.26–5.30 show the variation of surface quantities for the on-axis biconic at 0° and 12° AOA for $R_n = 0.04$ m. In Fig. 5.26 the surface pressure distribution is shown, which looks similar to Fig. 5.21. In Fig. 5.27 the variation of wall heat flux

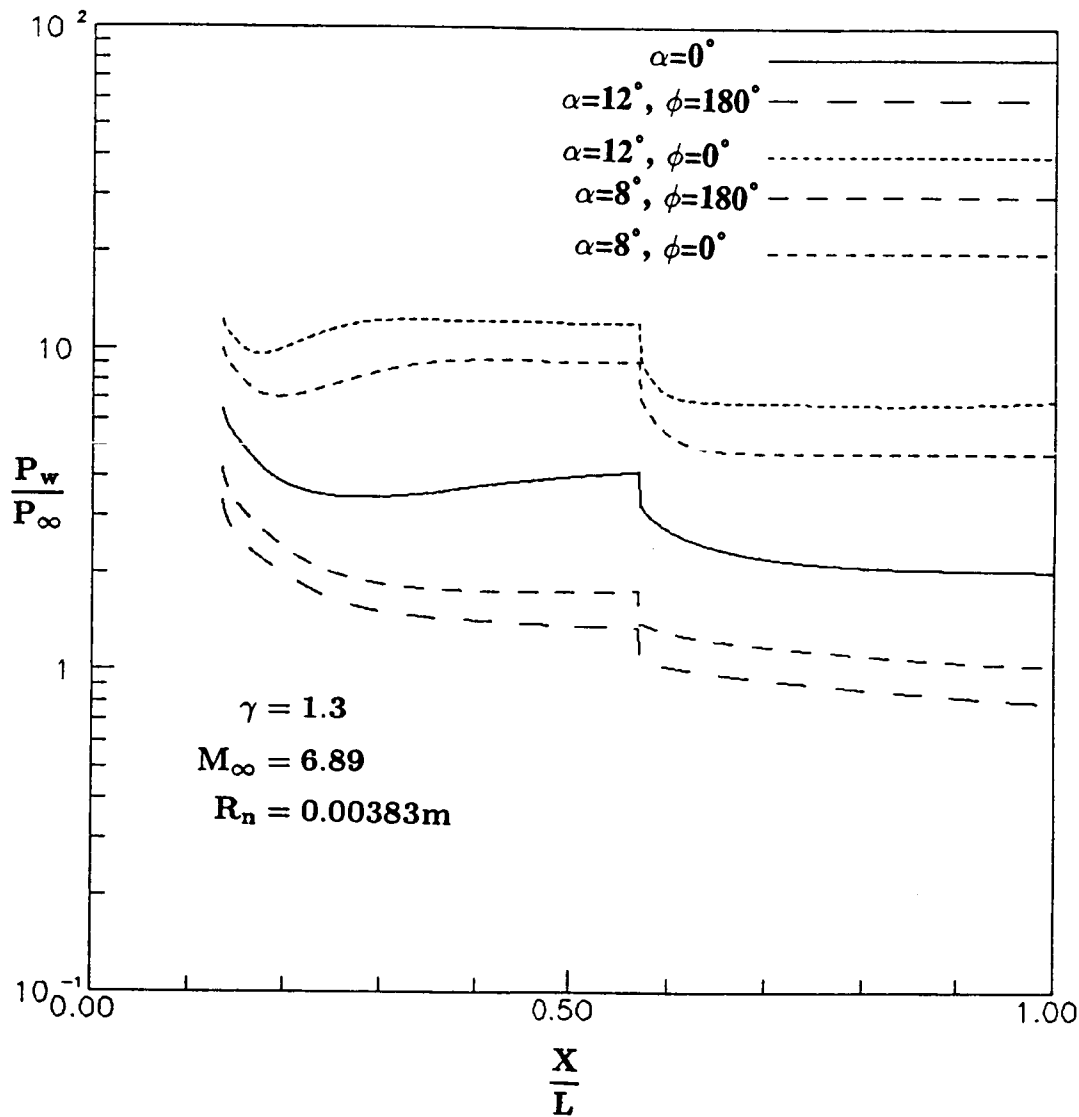


Fig. 5.21 Variation of surface pressure with axial distance
for $12.84^\circ / 7^\circ$ on-axis biconic at $0^\circ, 8^\circ$ and 12° AOA.

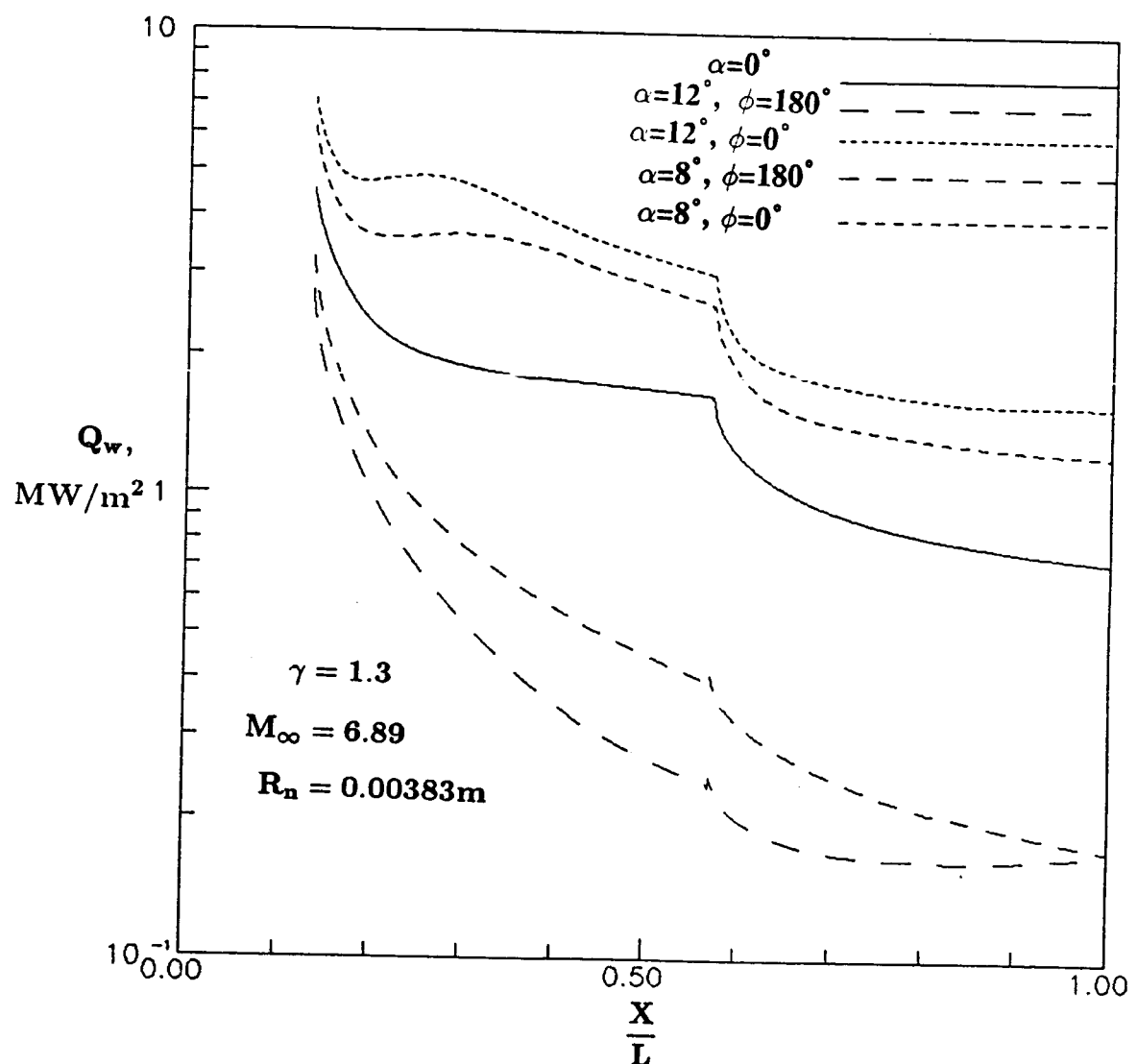


Fig. 5.22 Variation of wall heat transfer with axial distance for on-axis biconic at 0° , 8° and 12° AOA.

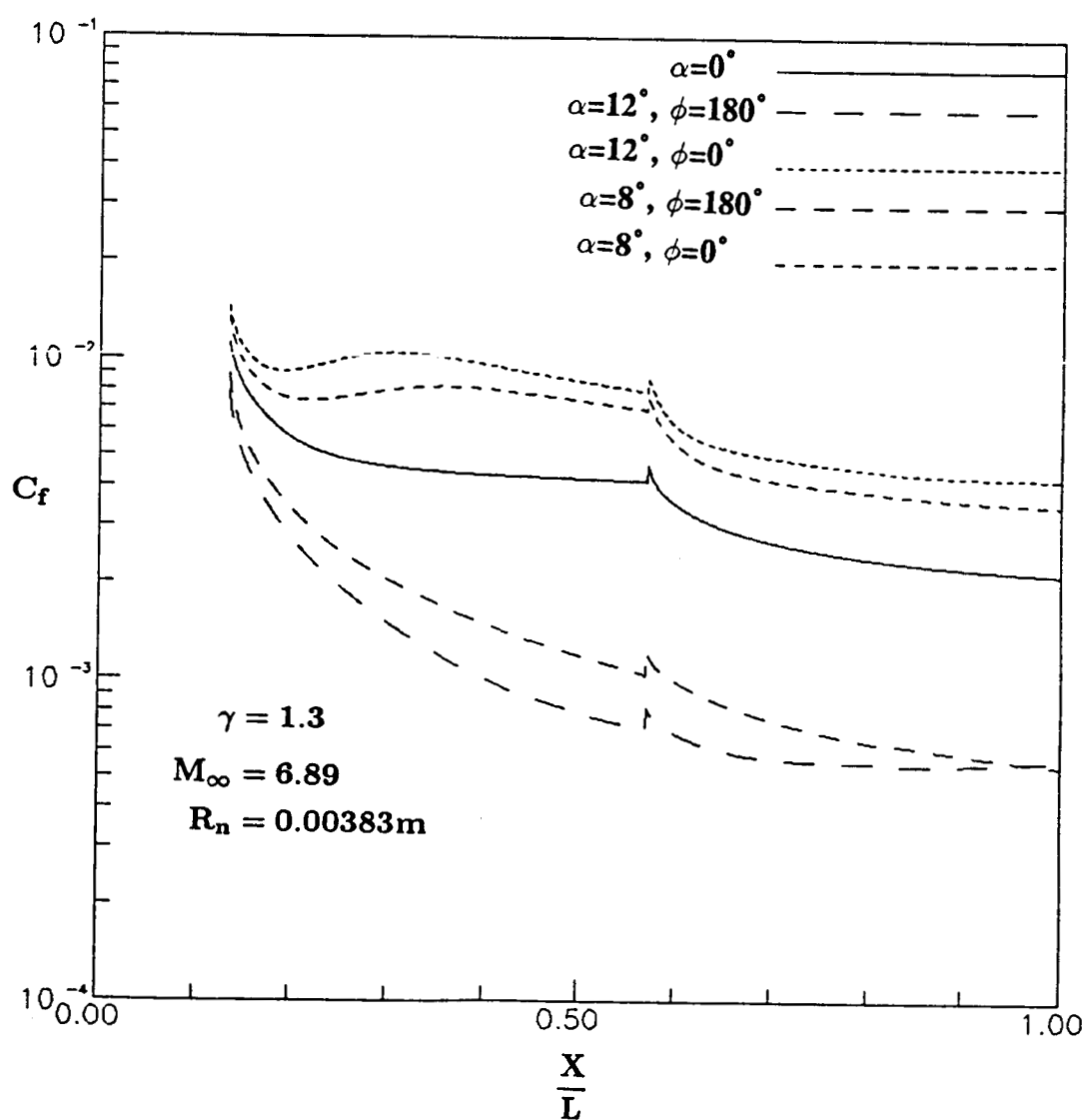


Fig. 5.23 Variation of skin friction coefficient with axial distance for on-axis biconic at 0° , 8° and 12° AOA.

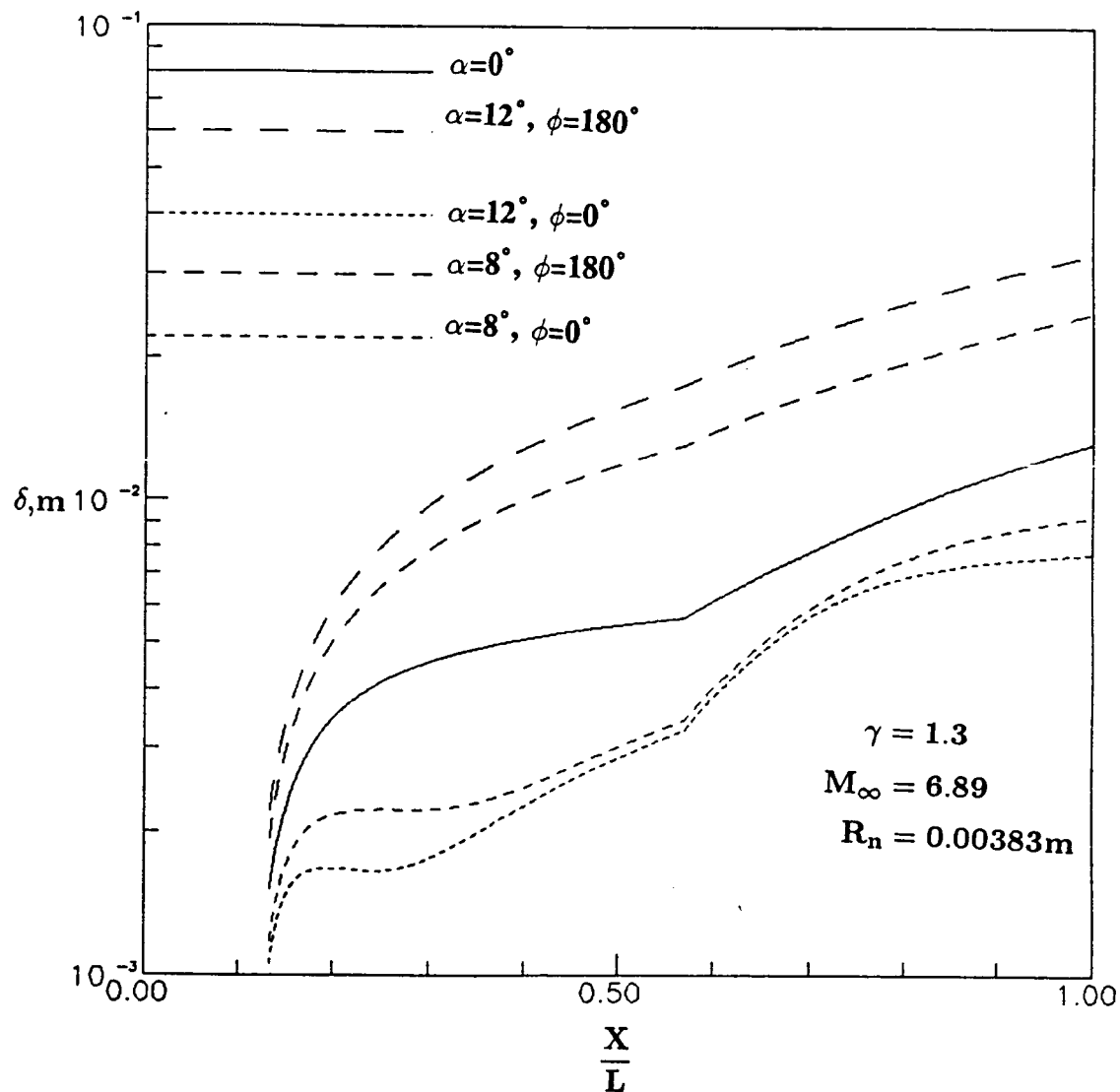


Fig. 5.24 Variation of shock stand-off distance with axial distance for on-axis biconic at 0° , 8° and 12° AOA.

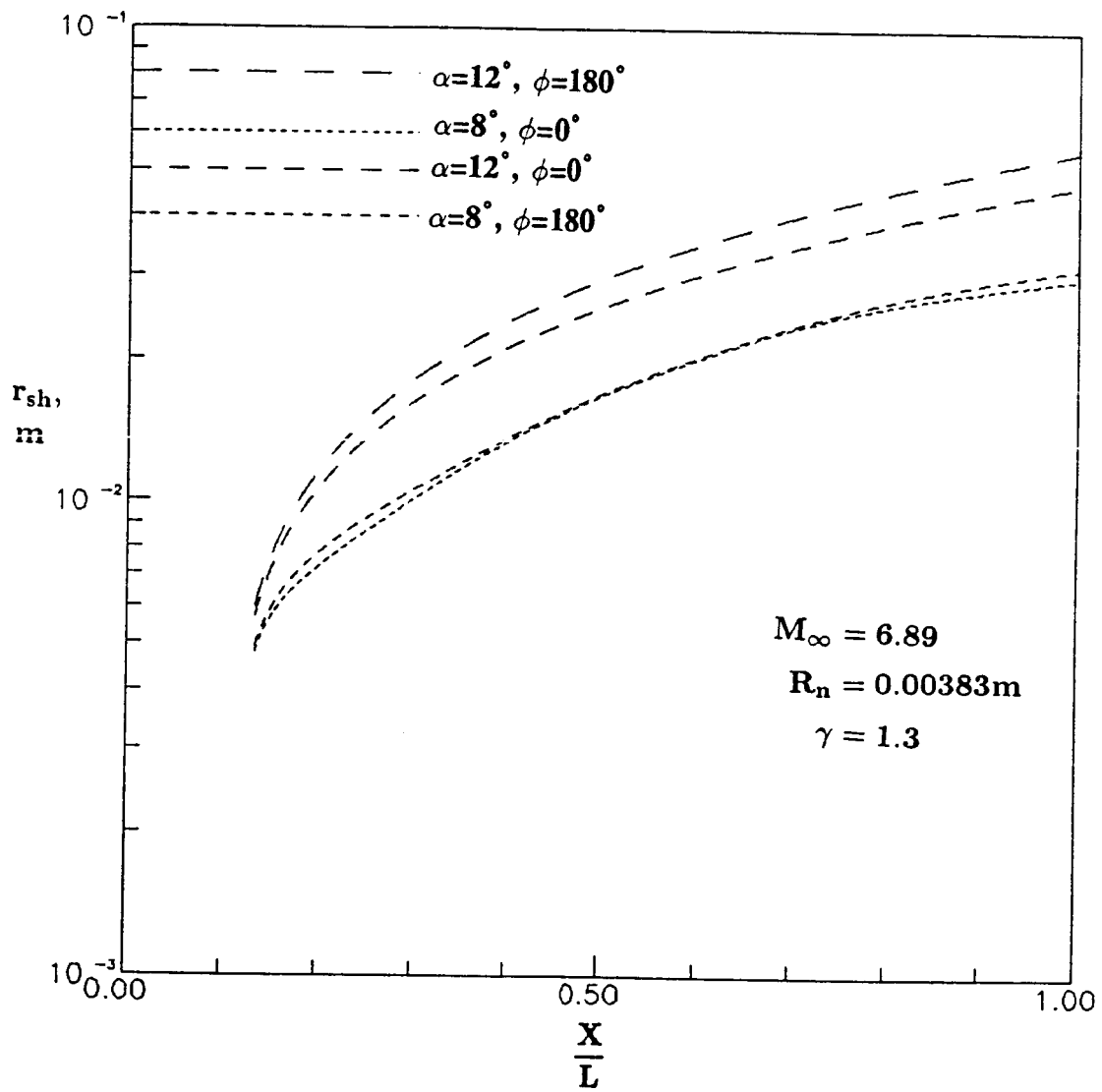


Fig. 5.25 Variation of shock shape with axial distance for on-axis biconic at 8° and 12° AOA.

(MW/m²) has been plotted as a function of nondimensionalized axial distance x/L . At 12° AOA, the leeward heating shows peculiar behavior. In the aft-section of the biconic, the heat flux increases as we march downstream. As mentioned earlier, at high AOA the leeward flow is characterized by flow separation and formation of two symmetrical counter rotating vortices that reattach on the most leeward ray [10]. At low Reynolds number, the leeward flow should be free of any secondary vortices [30]. This vortex reattachment results in the higher heating on the most leeward rays. Heating rates start increasing slightly on the windward side far downstream of the aft-cone section. The variation of skin friction coefficient with axial distance is presented in Fig. 5.28. It follows the same general trend as does the wall heat transfer.

Figures 5.29 and 5.30 show the variation of shock stand-off distance and shock shape as a function of axial distance x/L for the on axis biconic. The results are similar to one shown in Figs. 5.24 and 5.25, respectively, but with the increase in bluntness, the shock stand-off distance and shock shape increase by an order of magnitude.

5.2.4 Effects of Nose Bluntness and Angle of Attack on Flow field Quantities

Figures 5.31–5.33 show the variation of streamwise velocity as a function of normal distance r for Mach 6.89 perfect gas flow over straight biconic at different axial distances. The velocity has been nondimensionalized with respect to its free stream value. It should be noted that since the shock fitting procedure is used, the normal profiles are plotted within the shock layer only. There is a significant difference between the profile shape near the nose and that which is seen far downstream. The thickness of the boundary layer increases as the flow is marched in the axial direction downstream. In Fig. 5.31 the streamwise velocity profiles are shown at 0° AOA, whereas Fig. 5.32 shows the velocity profile at 12° AOA on leeward side. By comparison we find that in Fig. 5.31 the slope of the profile changes on the outer edge of the boundary layer between $x/R_n = 7.04$ and $x/R_n = 18.73$. This causes an appreciable influence on the wall quantities. Also, in Fig.

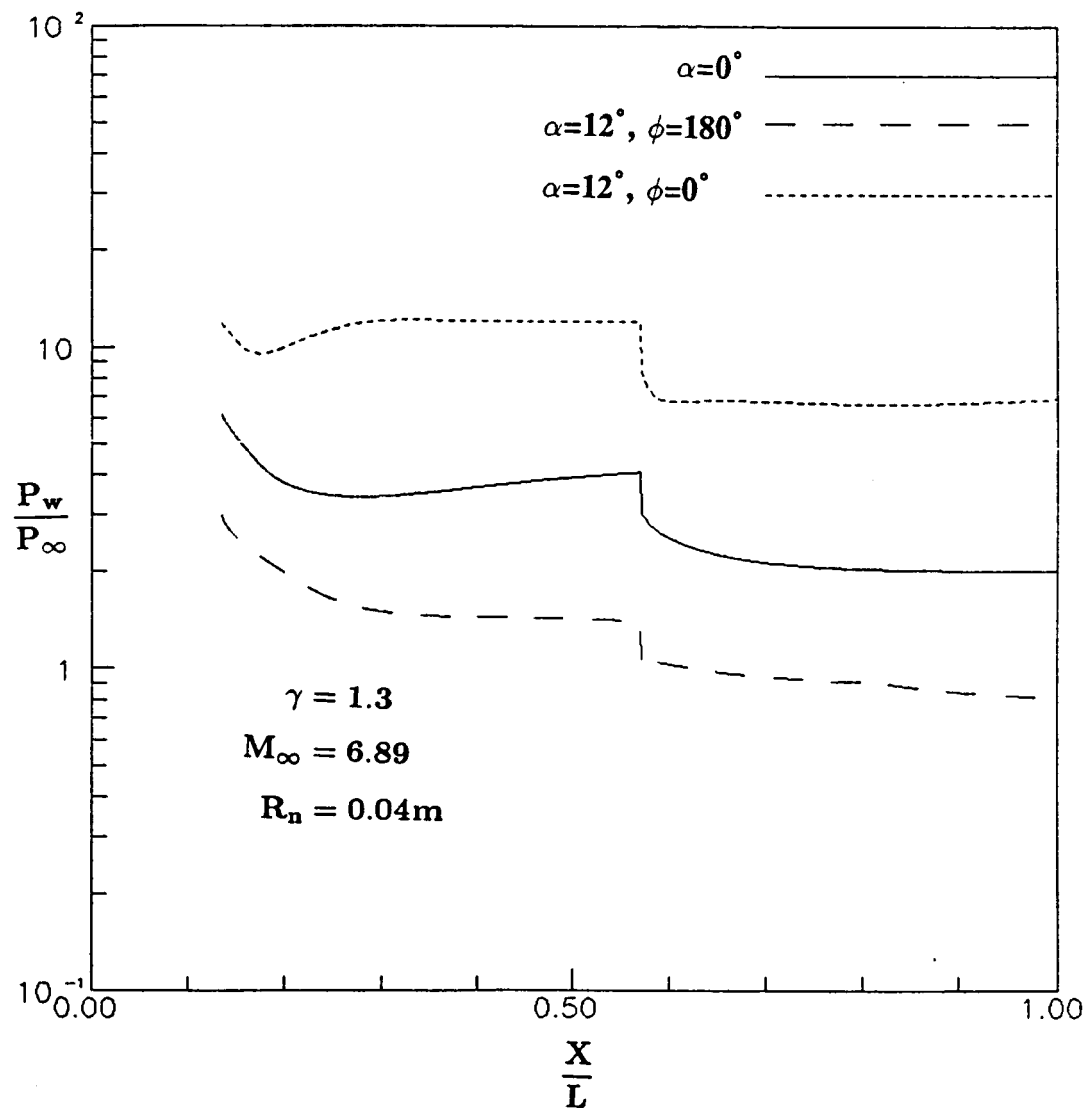


Fig. 5.26 Variation of surface pressure with axial distance
for on-axis biconic at 0° and 12° AOA, $R_n=0.04$ m.

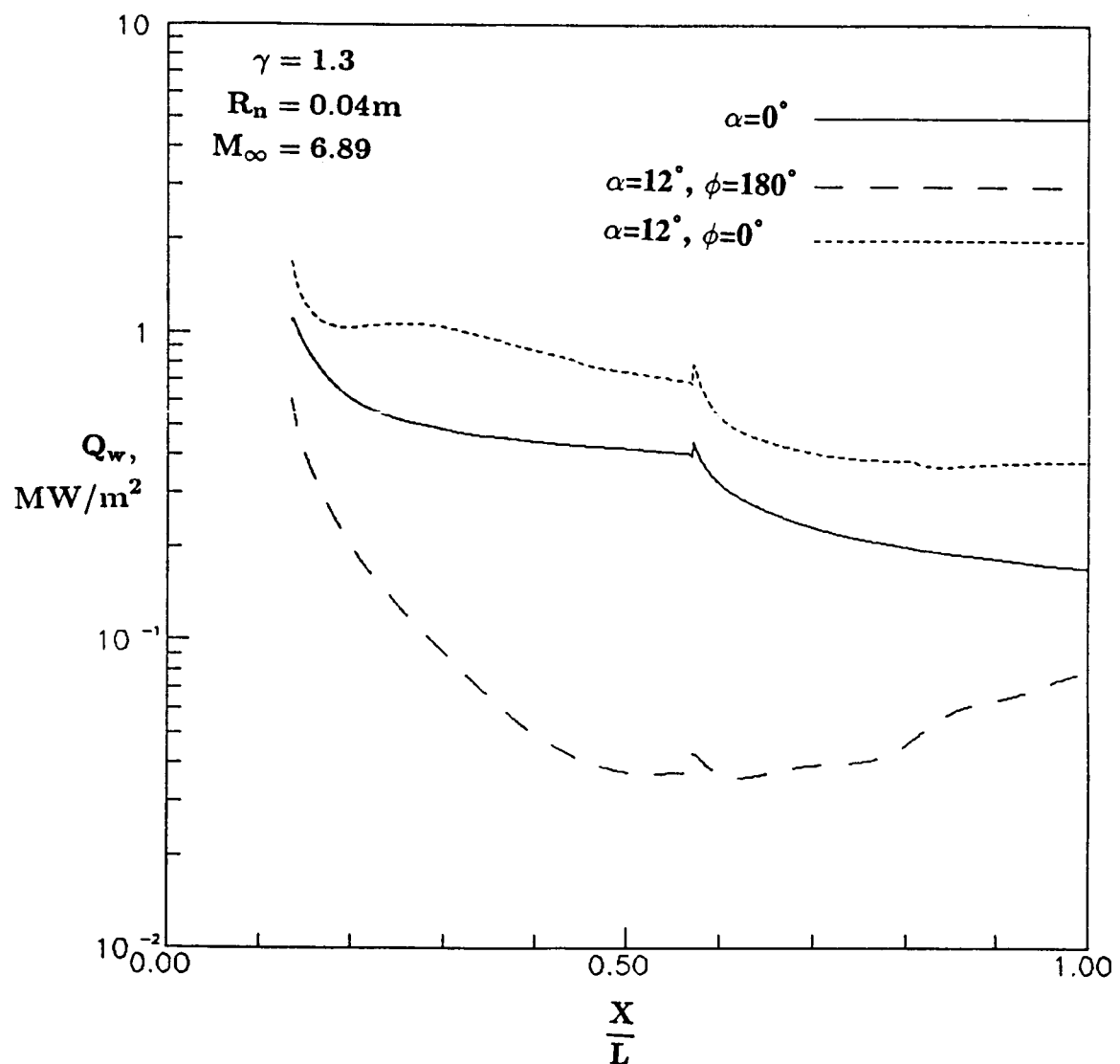


Fig. 5.27 Variation of wall heat transfer with axial distance
for on-axis biconic at 0° and 12° AOA, $R_n=0.04$ m.

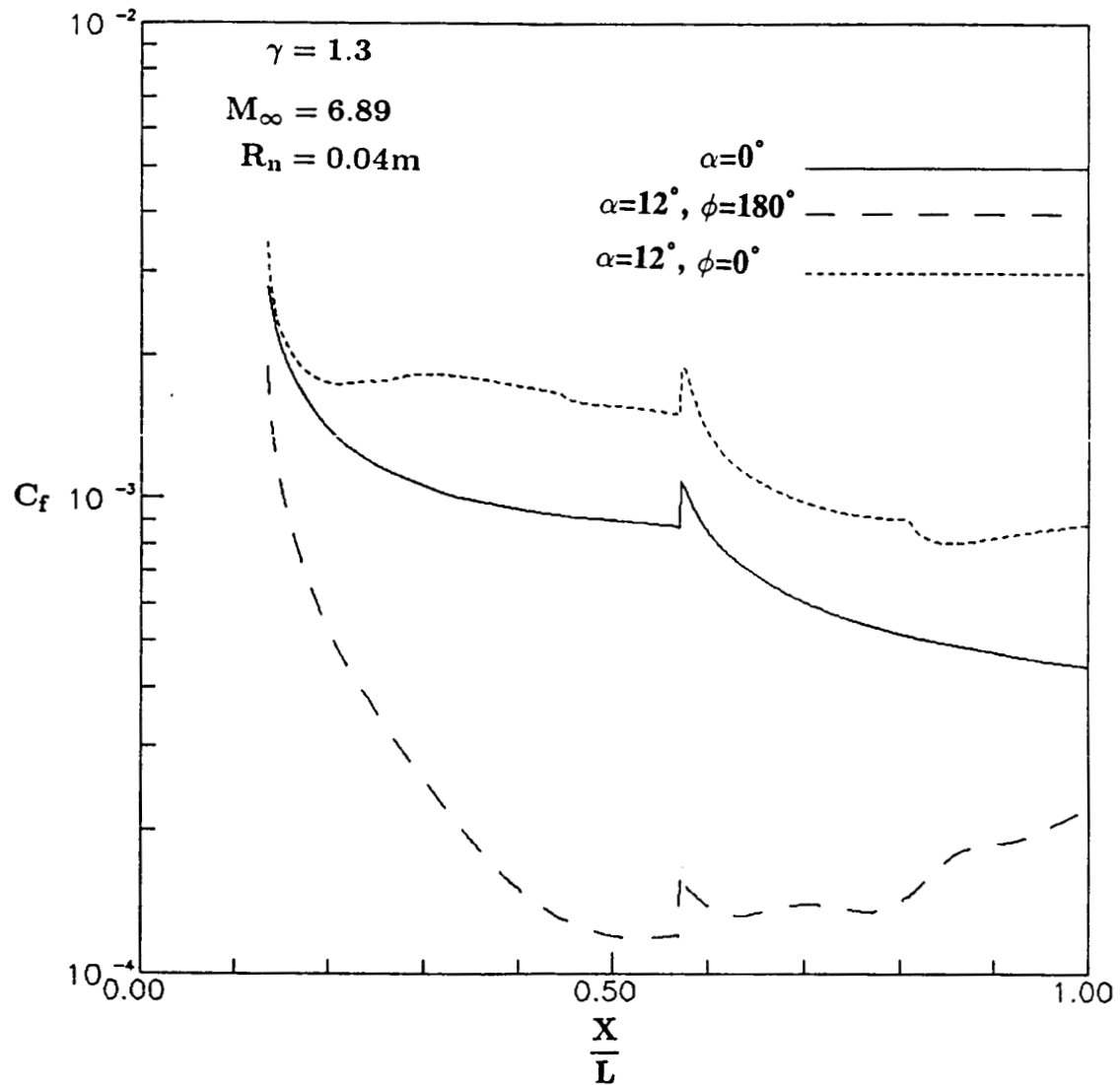


Fig. 5.28 Variation of skin friction coefficient with axial distance for on-axis biconic at 0° and 12° AOA, $R_n=0.04$ m.

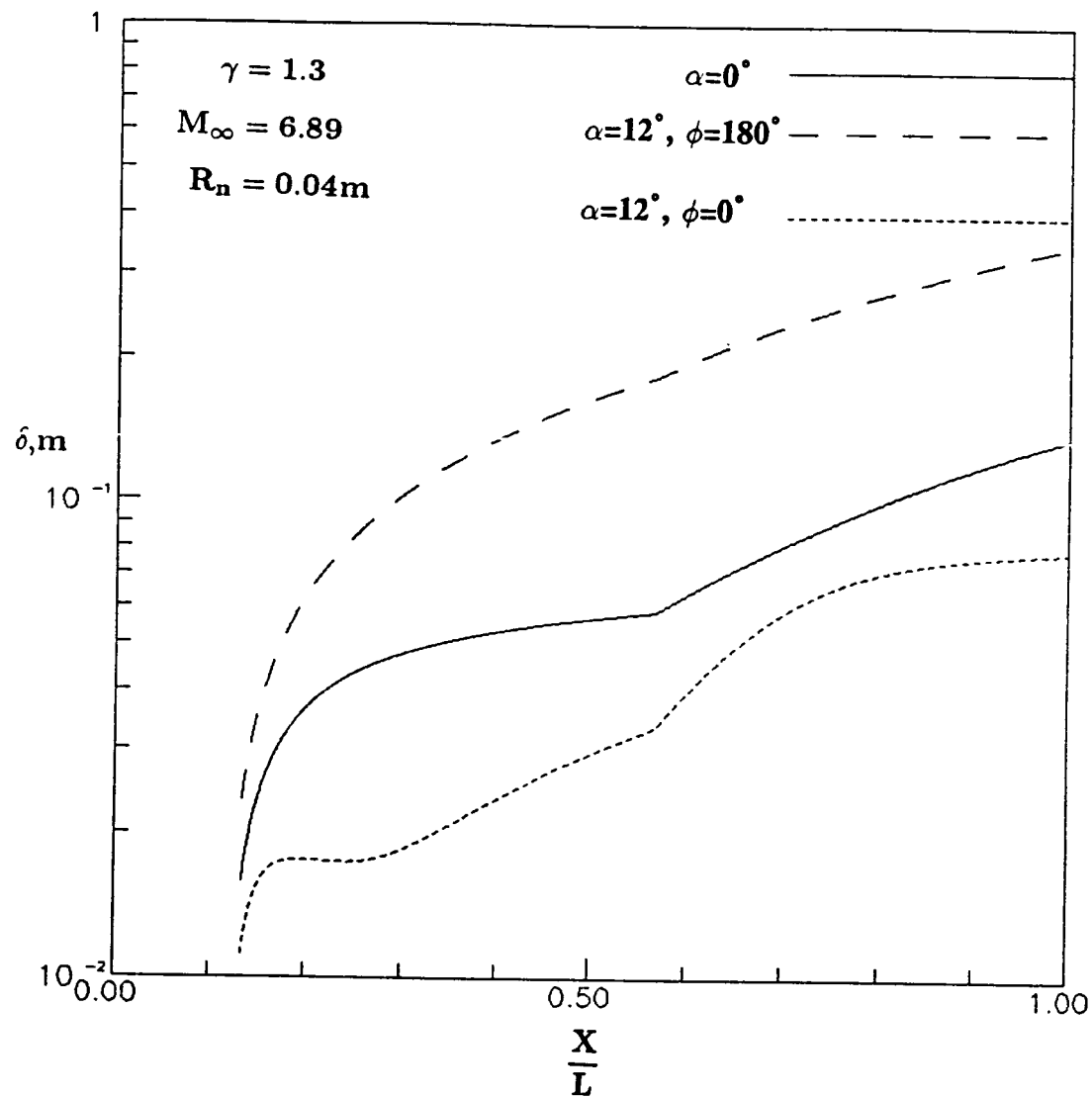


Fig. 5.29 Variation of shock standoff distance with axial distance for on-axis biconic at 0° and 12° AOA for $R_n=0.04$ m

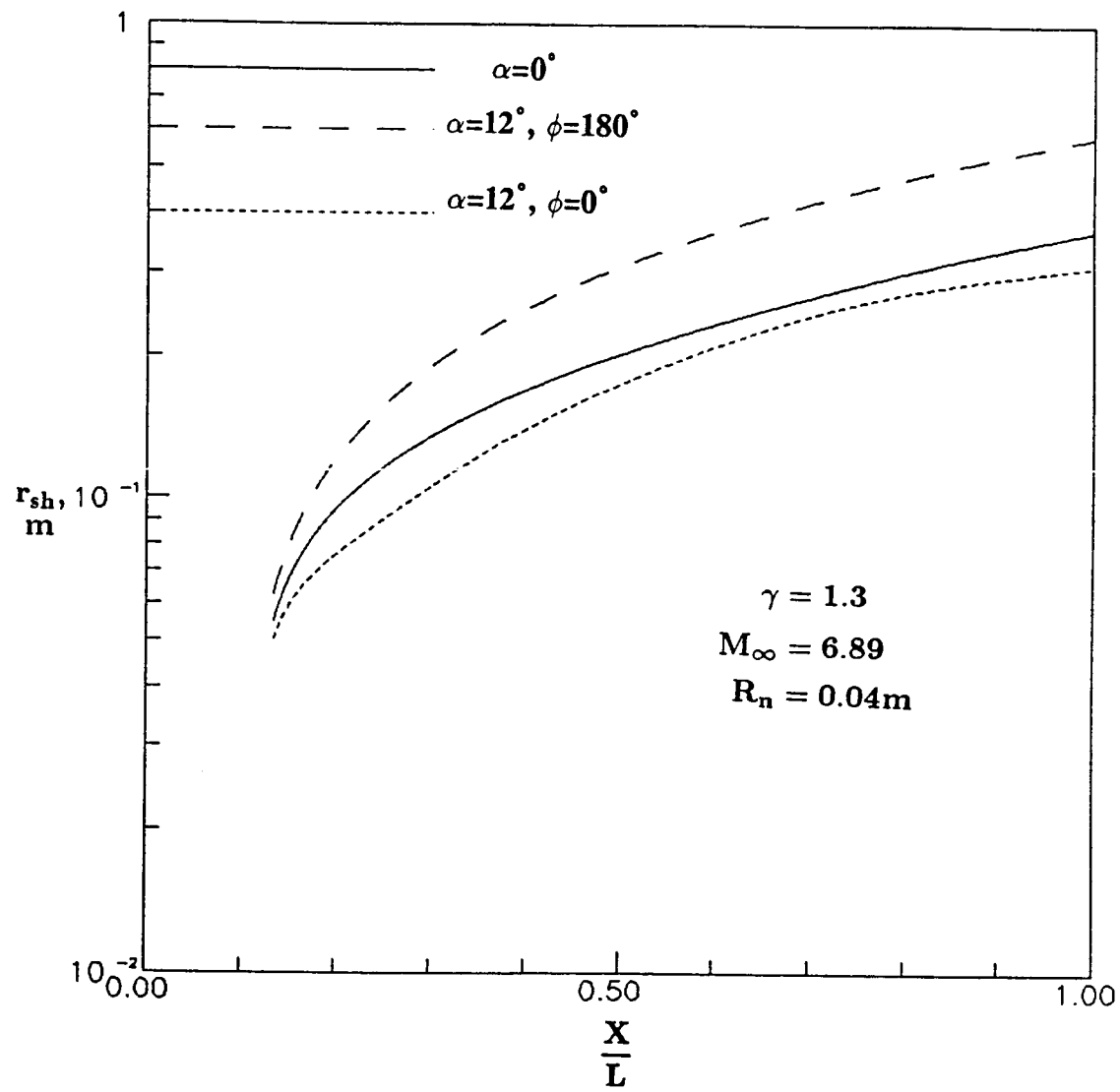


Fig. 5.30 Variation of shock shape with axial distance
for on-axis biconic at 0° and 12° AOA, $R_n=0.04$ m.

5.32, the presence of large velocity gradients at distances far downstream indicates that boundary layer is relatively thicker as compared to Fig. 5.31. Figure 5.33 shows the velocity profiles on windward side for 12° AOA. At any particular axial location the boundary layer is thin on the windward plane compared to the leeward plane. The shape of the velocity profiles also looks different in comparison to the leeward plane. This is because the corresponding entropy layer is very thin.

Figure 5.34 shows the temperature profiles for the straight biconic at 0° AOA. The temperature has been nondimensionalized with respect to its free stream value. These profiles have been plotted for the cold wall condition. The temperature starts rising as we move from the wall towards the bow shock because of the frictional heating or strong viscous dissipation within the thermal boundary layer. The peak temperature occurs in the thermal boundary layer. Although there is a temperature jump behind the bow shock, this increase in temperature is not so intense compared to the peak temperature in the boundary layer. Therefore, just outside the boundary layer or entropy layer the temperature starts decreasing until the bow shock is approached. The bow shock is stronger near the nose region and its strength decreases farther downstream. Correspondingly, the peak temperature observed is higher near the nose region compared to that at axial distances farther downstream. However, on the aft-section of the biconic, the shape of the temperature profiles at the outer edge change significantly due to the presence of a thick entropy layer. Figures 5.35 and 5.36 show the temperature profiles at 12° AOA for the leeward and windward meridians respectively. On the leeward plane, strong temperature gradients are observed at axial distances far downstream from the nose region. The temperature profiles become almost parallel to each other, a short distance downstream of the nose section. The thermal boundary layer thickness in the leeward plane is almost twice that which observed in the windward plane on the aft-section of the biconic. Because of a thin boundary layer in the windward plane, the peak temperature close to the nose region is high in comparison to what is observed in the leeward plane.

Figure 5.37 show the entropy profiles for the straight biconic at 0° AOA. Entropy change was computed according to Eq. (3.5). Figures 5.38 and 5.39 show the entropy profiles at 12° AOA for the leeward and windward planes respectively. These profiles follow the same general trend as the temperature profiles. Variation of pressure in the normal direction is experienced mostly in the vicinity of the nose region, and very close to the wall. As the flow is marched downstream in the axial direction, this effect diminishes. Hence in computing entropy change the flow field temperature has a dominating effect compared to the pressure. By comparing entropy and velocity profiles we can conclude that the entropy layer is not swallowed until $x=30 R_n$. For calculating the swallowing distance it is necessary to march further downstream, which requires the body geometry to be modified. Pressure profiles for the straight biconic at 0° and 12° AOA are shown in Figs. 5.40–5.42 respectively. The pressure has been nondimensionalized with respect to the freestream pressure. Only in the nose region are the pressure gradients strong (close to the wall), but as the flow is marched progressively towards the fore-cone section, the magnitude of these gradients decreases and Pitot pressure almost becomes constant in the normal direction. The magnitude of pressure on the leeward side is much less than the windward side, as can be seen clearly from Figs. 5.41 and 5.42.

Figures 5.43–5.46 show the contour plots for the on-axis biconic at 0° AOA. These contours are plotted within the body surface and bow shock at streamwise axial distance $x=11.9 R_n$ and for nose radius $R_n=0.00383$ m. Mach contours are shown in Fig. 5.43. The Mach number continuously decreases from the bow shock towards the body. Figure 5.44 shows the density contours. There is very slight change in the density within the shock layer. The reason is clear from the pressure contours shown in Fig. 5.45. Temperature contours are plotted in Fig. 5.46. Their behavior is clear from temperature profiles shown in Fig. 5.34.

Figures 5.47–5.50 show the contour plots at 12° AOA. These are plotted at axial location $x=26 R_n$ for $R_n = 0.00383$ m. Figure 5.47 shows the Mach contours. From

the figure it is clear that the shock is displaced on the leeward side and is no more concentric with the body. A viscous 'hump' appears on the leeward side which indicates that boundary layer is quite thick [3].

On the windward side the value of Mach number is low compared to that on the leeward side because the corresponding boundary layer is thin. In hypersonic regime, the compressible boundary layer thickness is directly proportional to the square of the Mach number. In the thermal boundary layer (Figs. 5.35 and 5.36) the temperature is very high. This affects the local velocity of sound and hence the Mach number. The density, pressure, and temperature contours are plotted in Figs. 5.48–5.50, respectively. Figures 5.51–5.54 show the contour plots of Mach number, density, pressure, and temperature respectively at 12° AOA and $R_n = 0.04$ m. These contours are also plotted at $x=26 R_n$. They look similar, as observed for the case of $R_n=0.00383$ m but physically they correspond to a different axial location, since the bluntness has been increased by one order of magnitude.

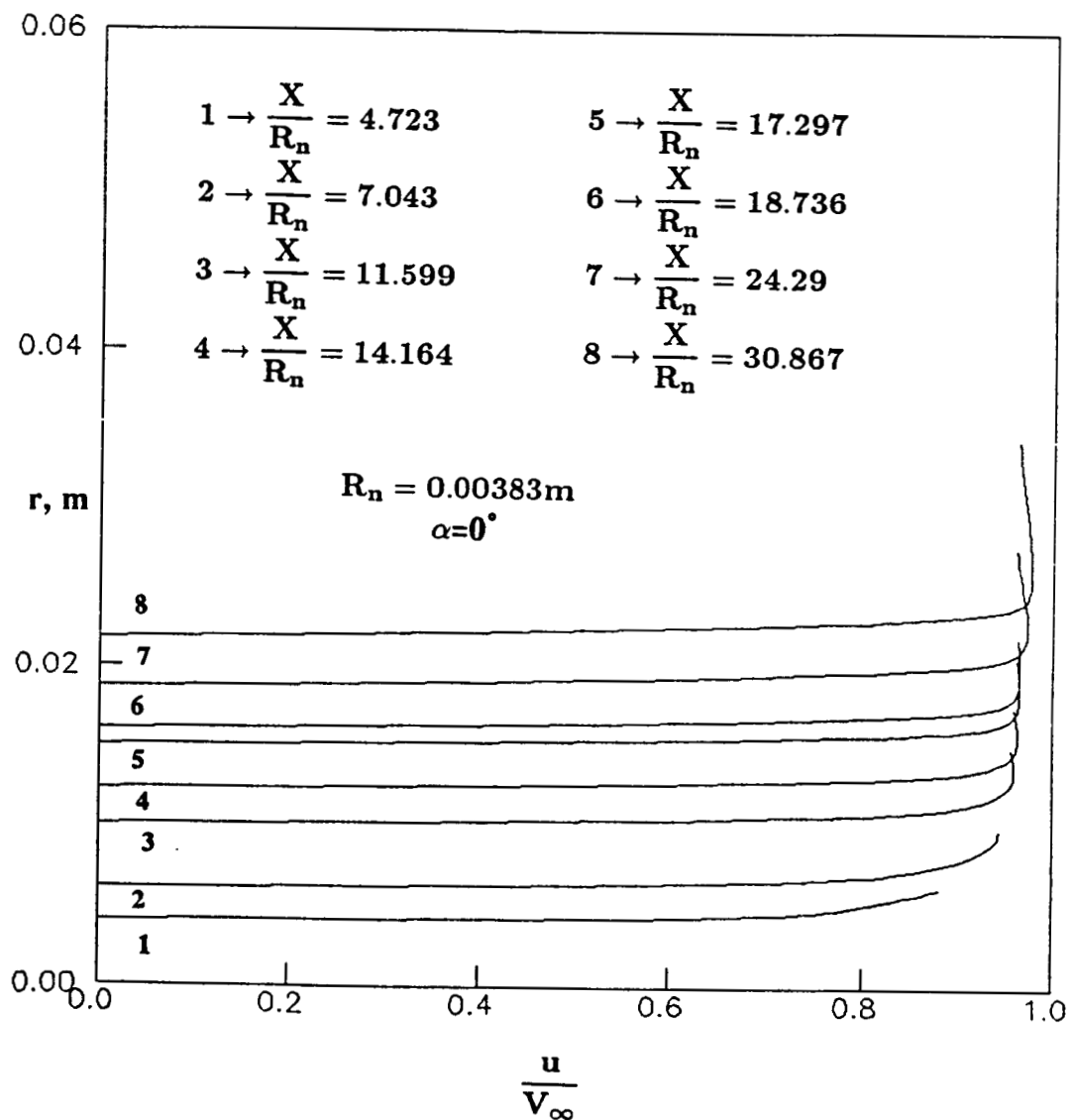


Fig. 5.31 u velocity profile for on-axis biconic at 0° AOA.

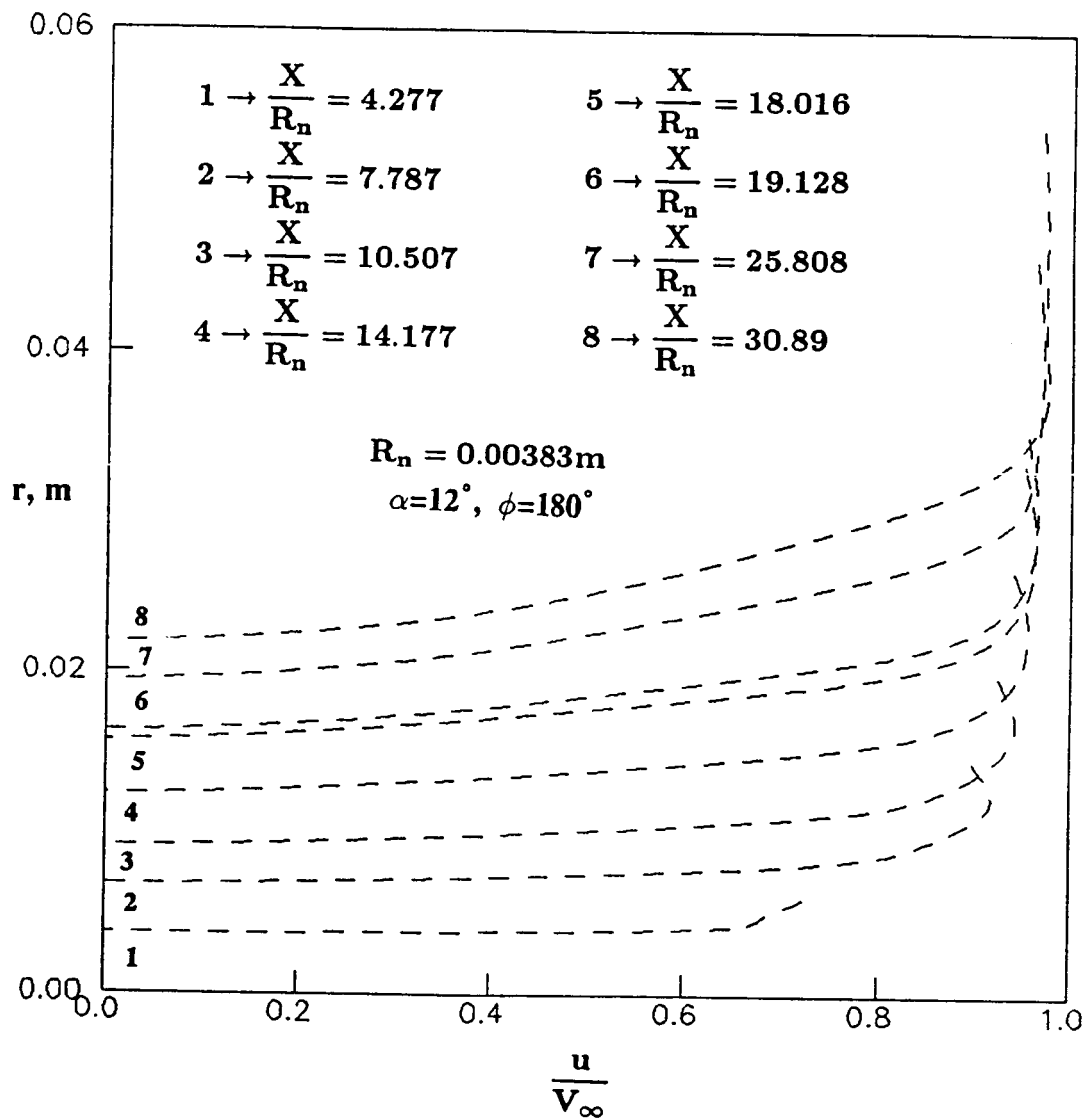


Fig. 5.32 u velocity profile at leeward side for on-axis biconic at 12° AOA.

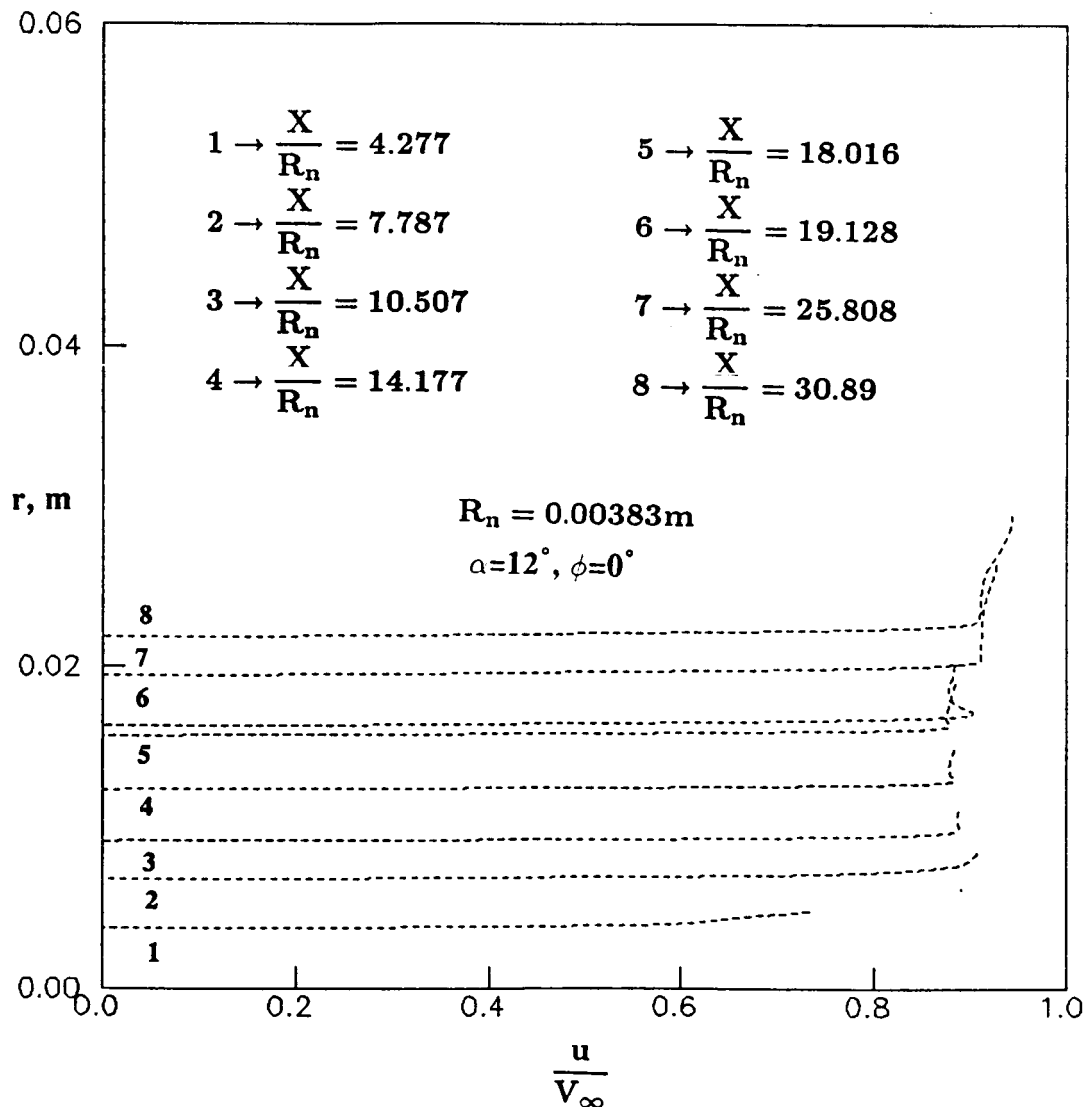


Fig. 5.33 u velocity profile at windward side for on-axis biconic at 12° AOA.

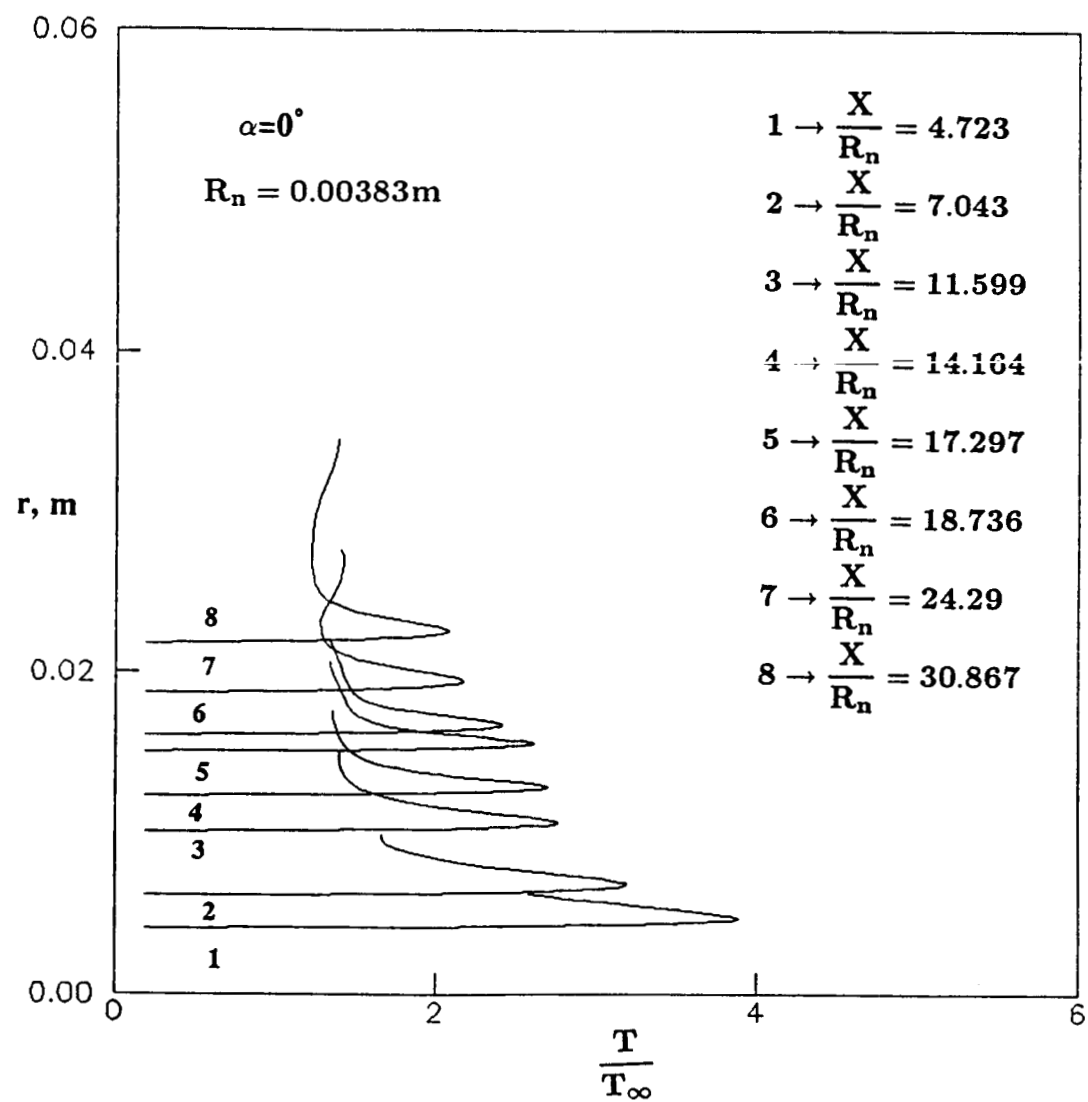


Fig. 5.34 Temperature profiles for on-axis biconic at 0° AOA.

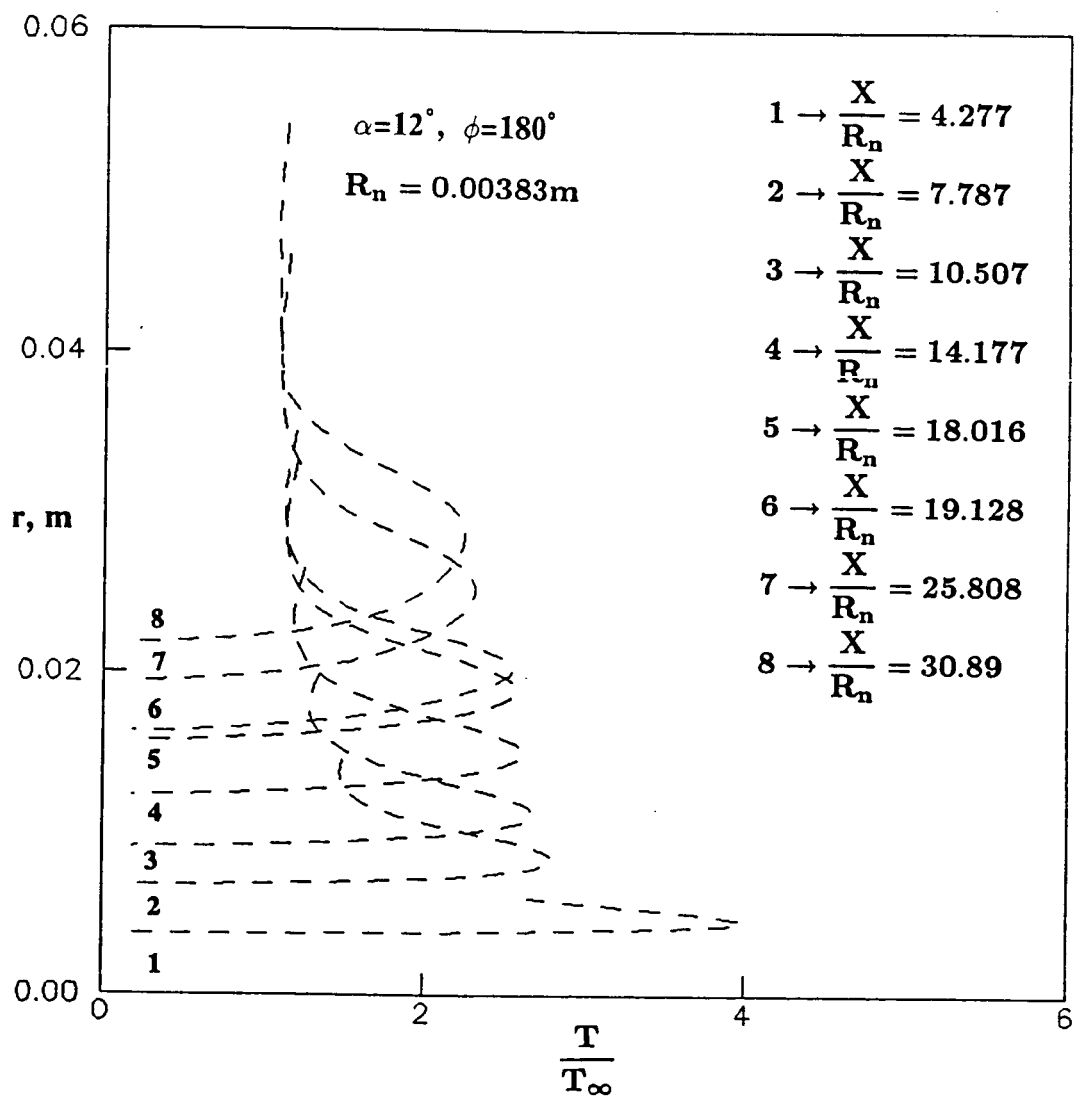


Fig. 5.35 Temperature profiles at leeward side for on-axis biconic at 12° AOA.

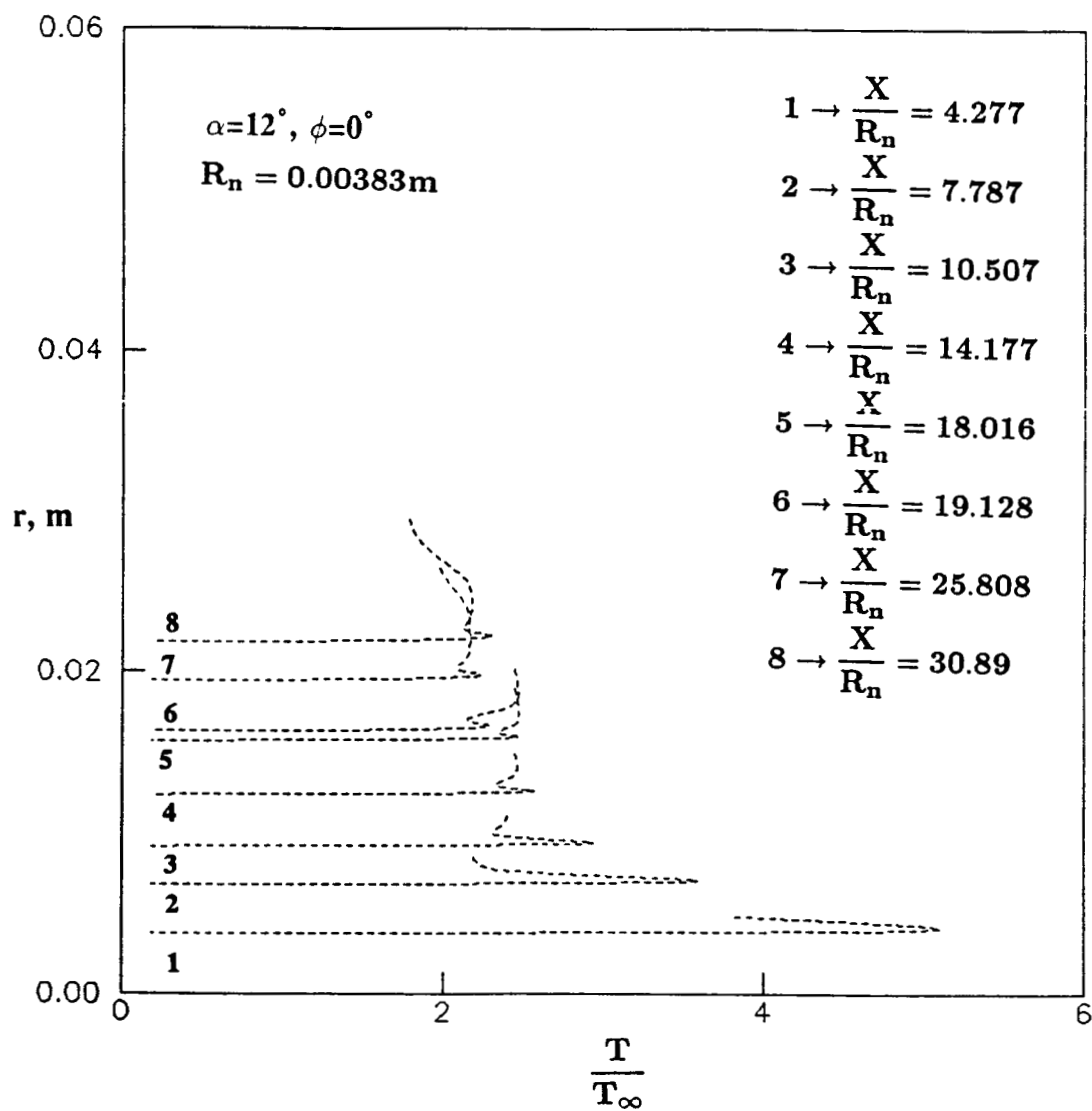


Fig. 5.36 Temperature profiles at windward side for on-axis biconic at 12° AOA.

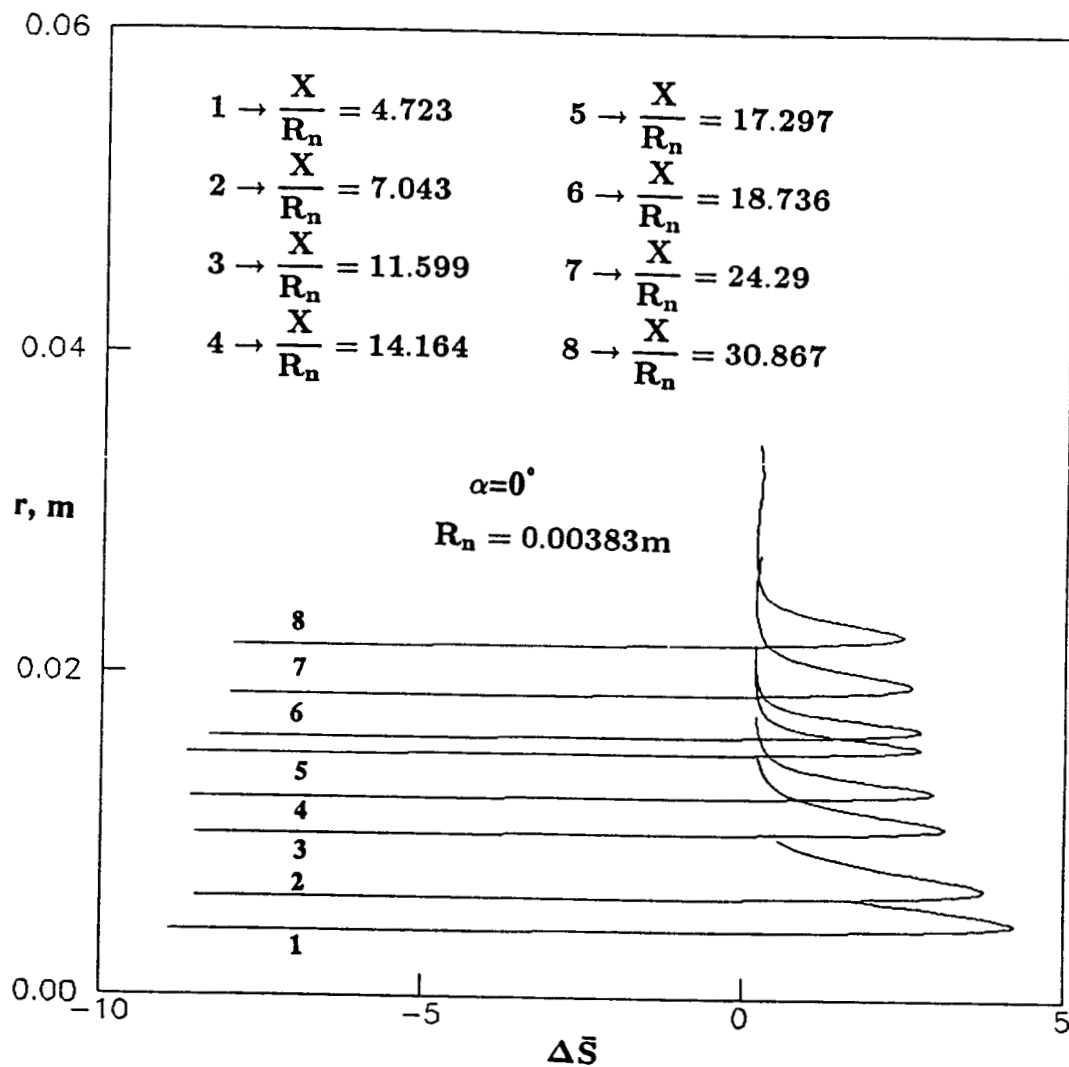


Fig. 5.37 Entropy profiles for on-axis biconic at 0° AOA.

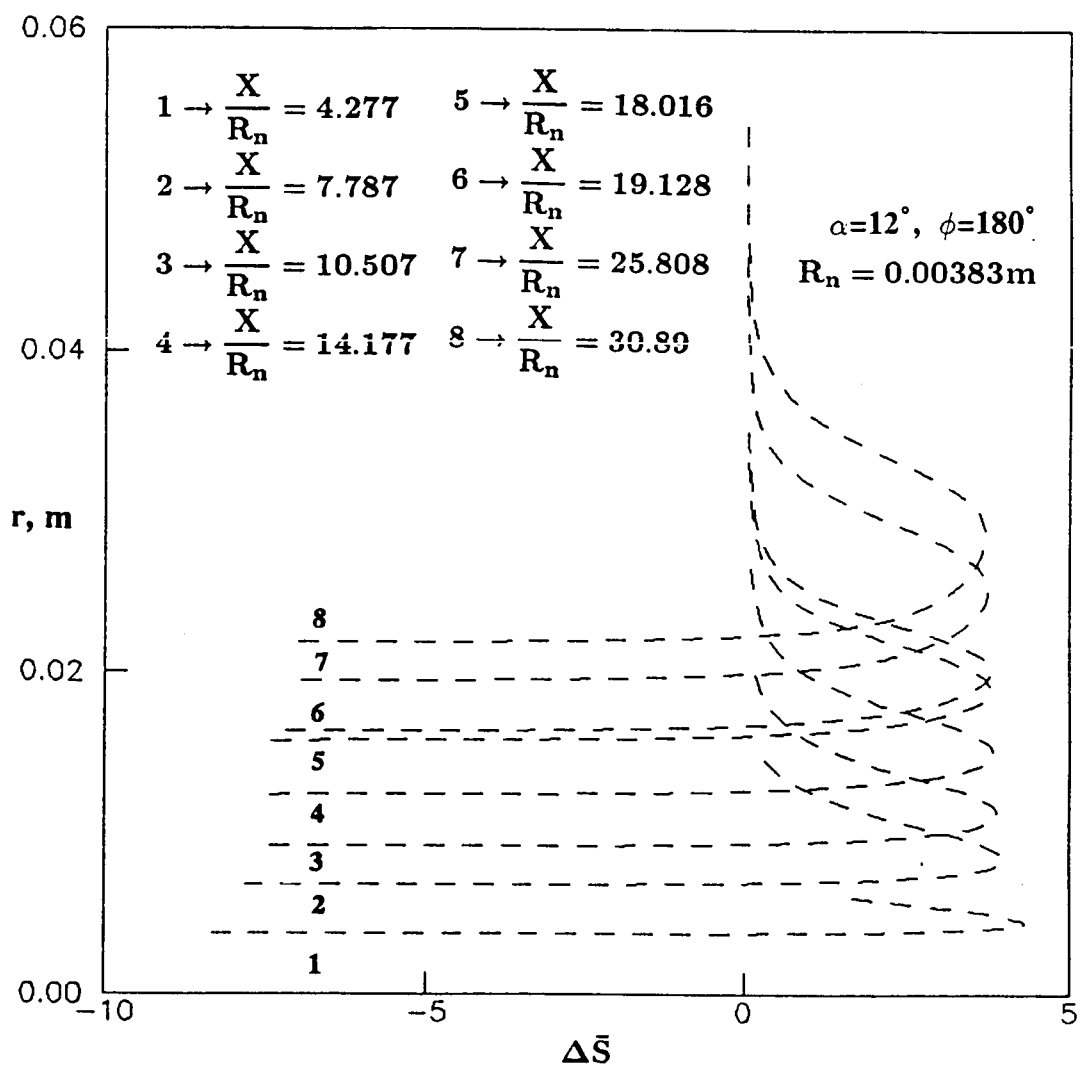


Fig. 5.38 Entropy profiles at leeward side for on-axis biconic at 12° AOA.

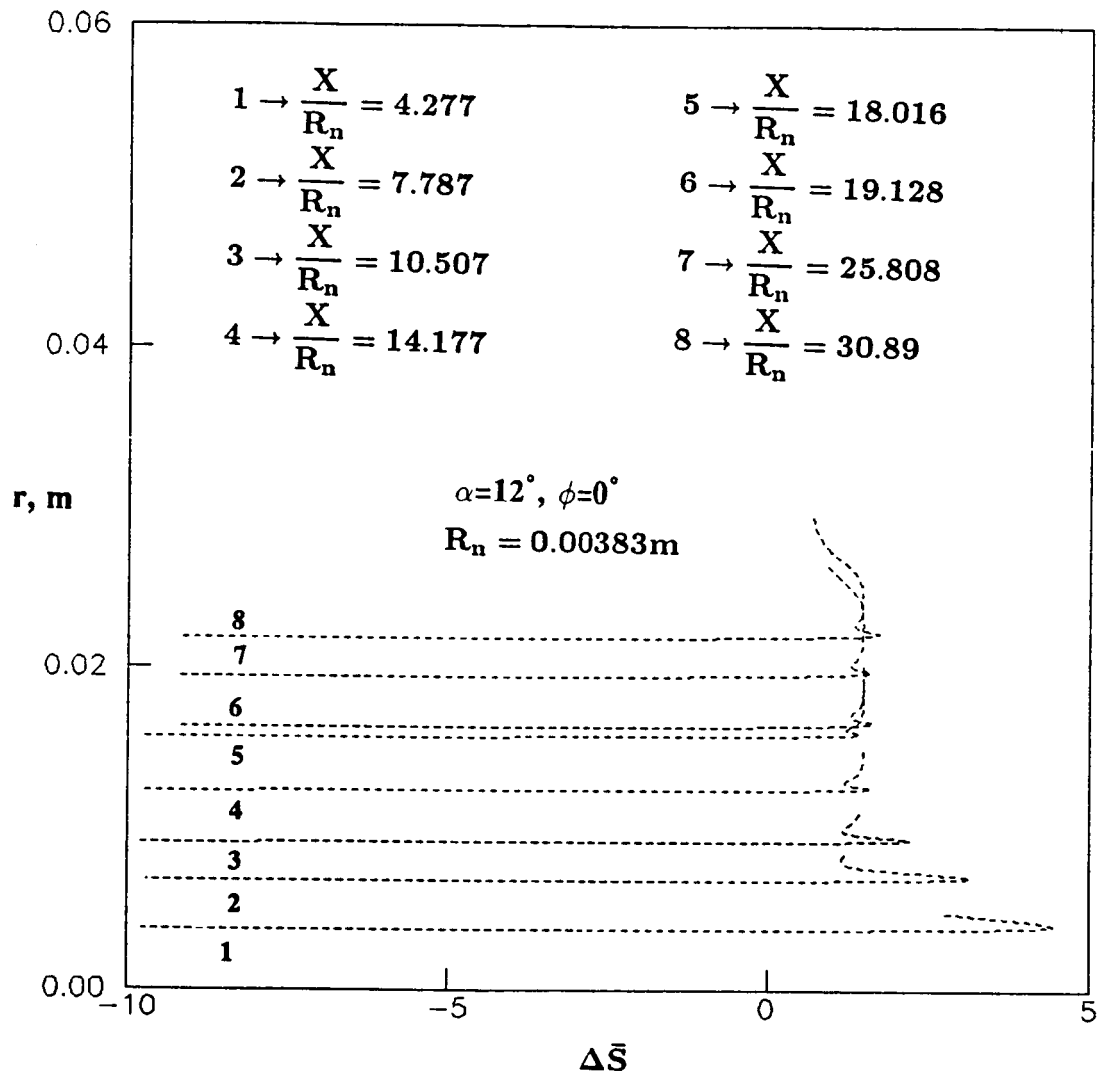


Fig. 5.39 Entropy profiles at windward side for on-axis biconic at 12° AOA.

C-2

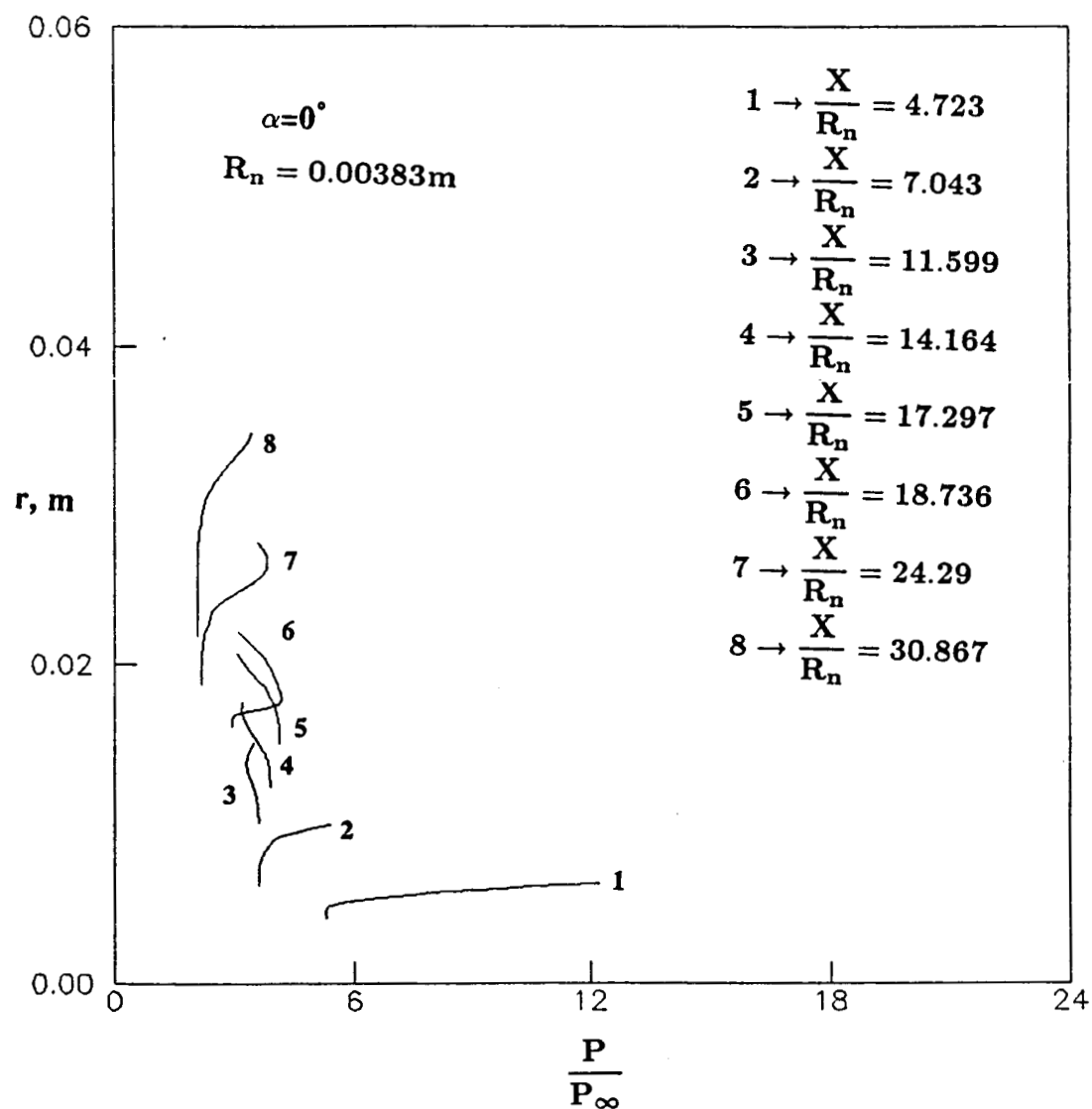


Fig. 5.40 Pressure profiles for on-axis biconic at 0° AOA.

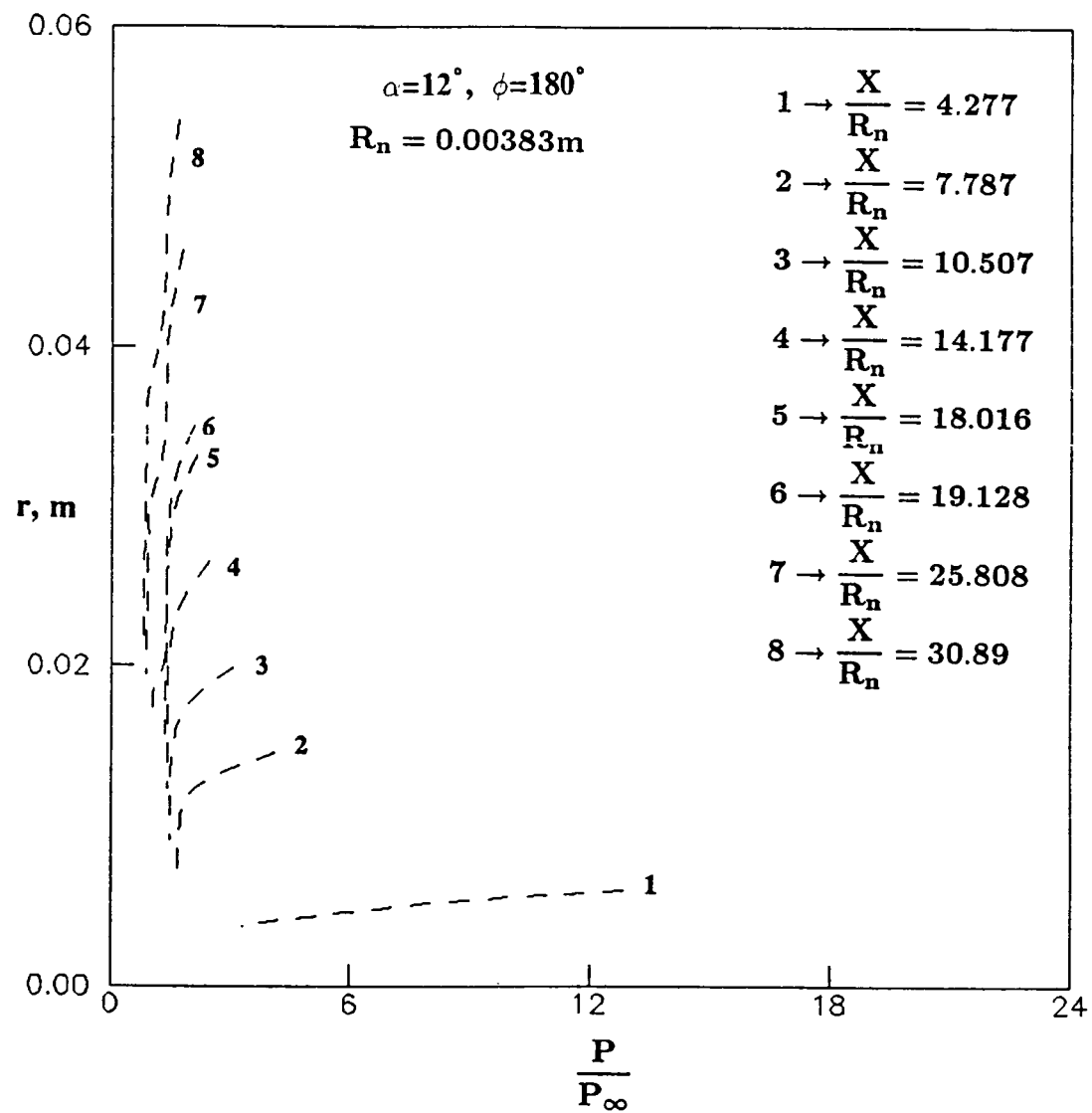


Fig. 5.41 Pressure profiles at leeward side for on-axis biconic at 12° AOA.

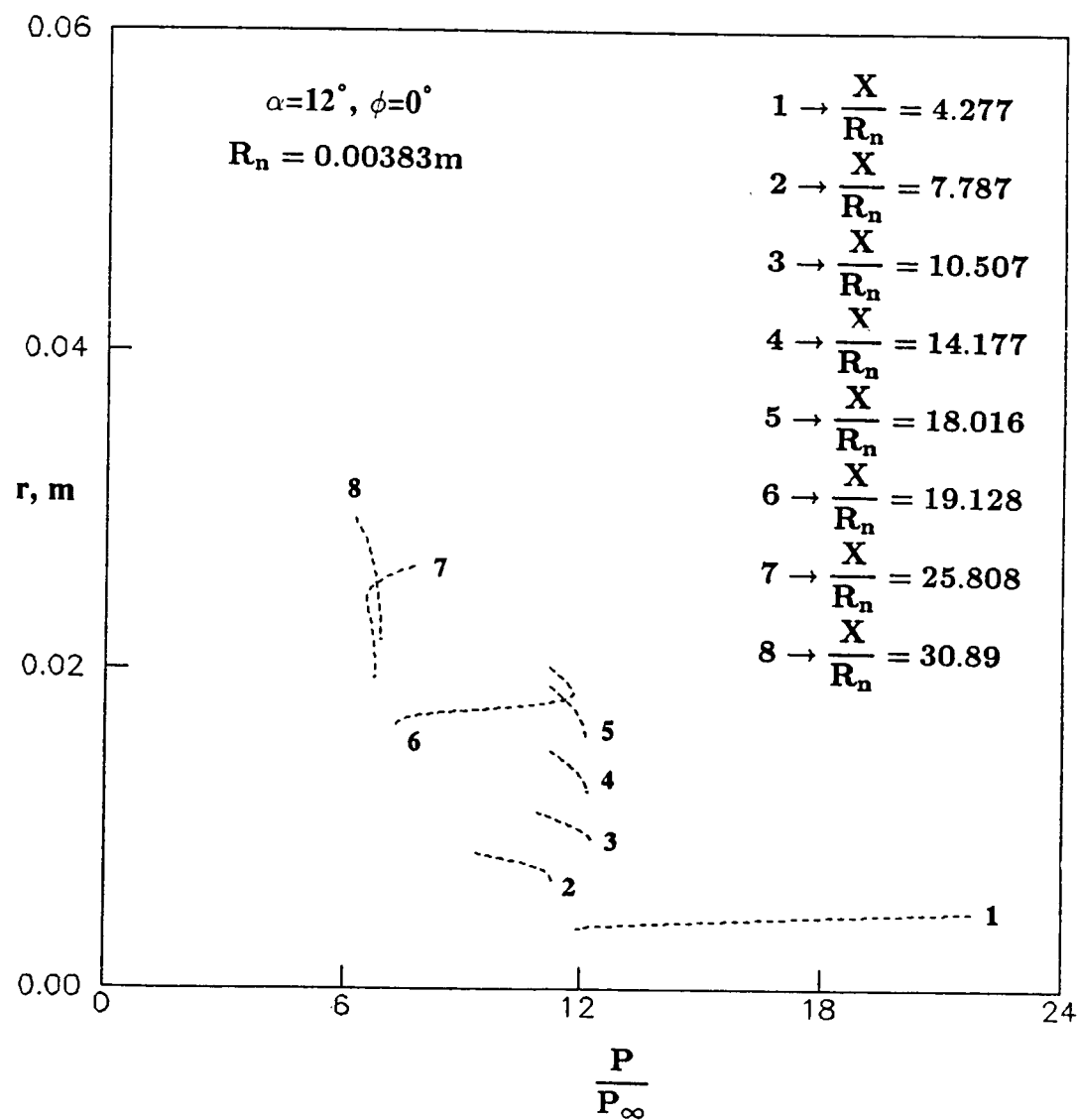


Fig. 5.42 Pressure profiles at windward side for on-axis biconic at 12° AOA.

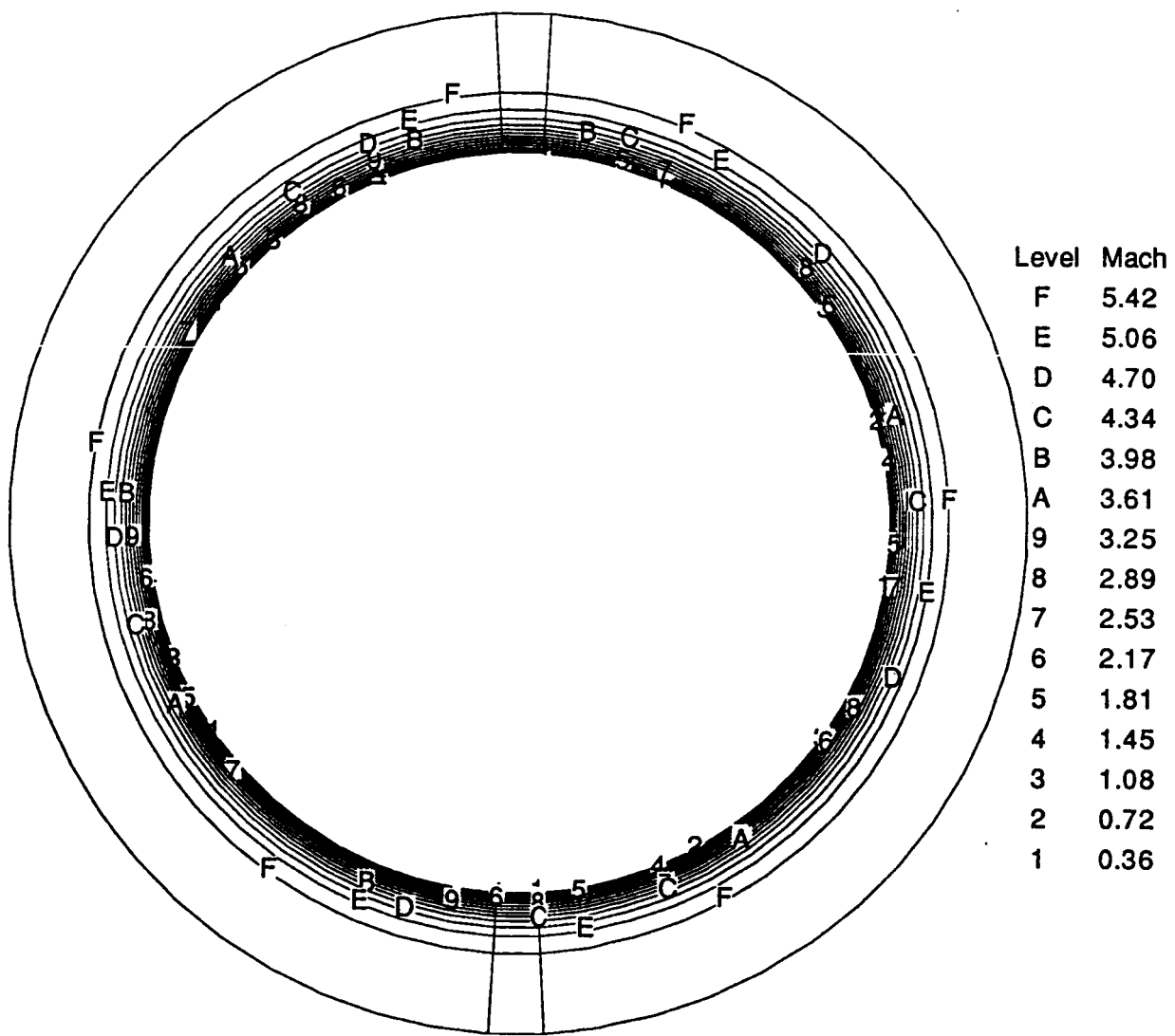


Fig. 5.43 Mach contours for on-axis biconic at 0° AOA, $R_n=0.00383$ m, $x=11.9 R_n$.

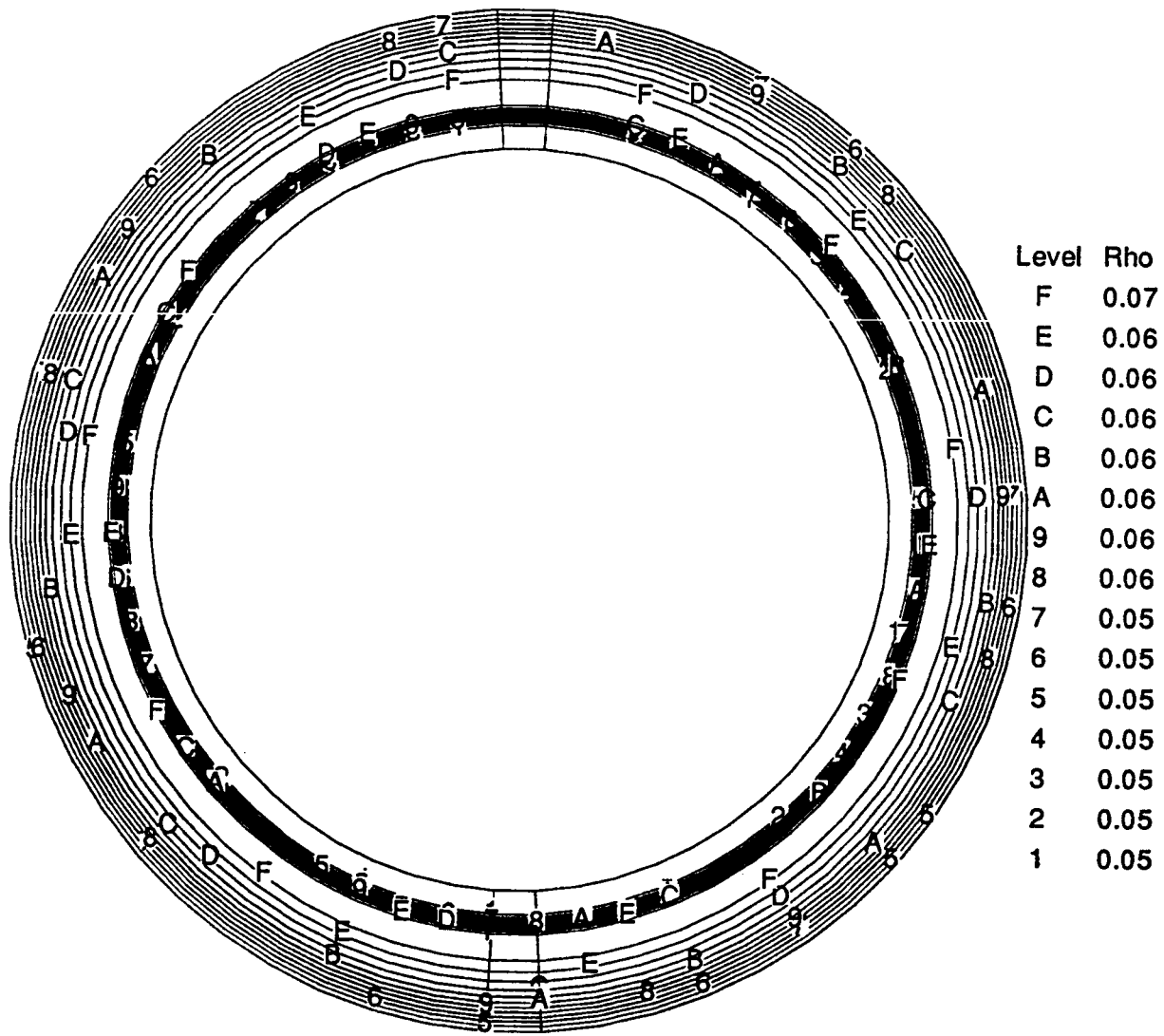


Fig. 5.44 Density contours for on-axis biconic at 0° AOA, $R_n=0.00383$ m, $x=11.9 R_n$.

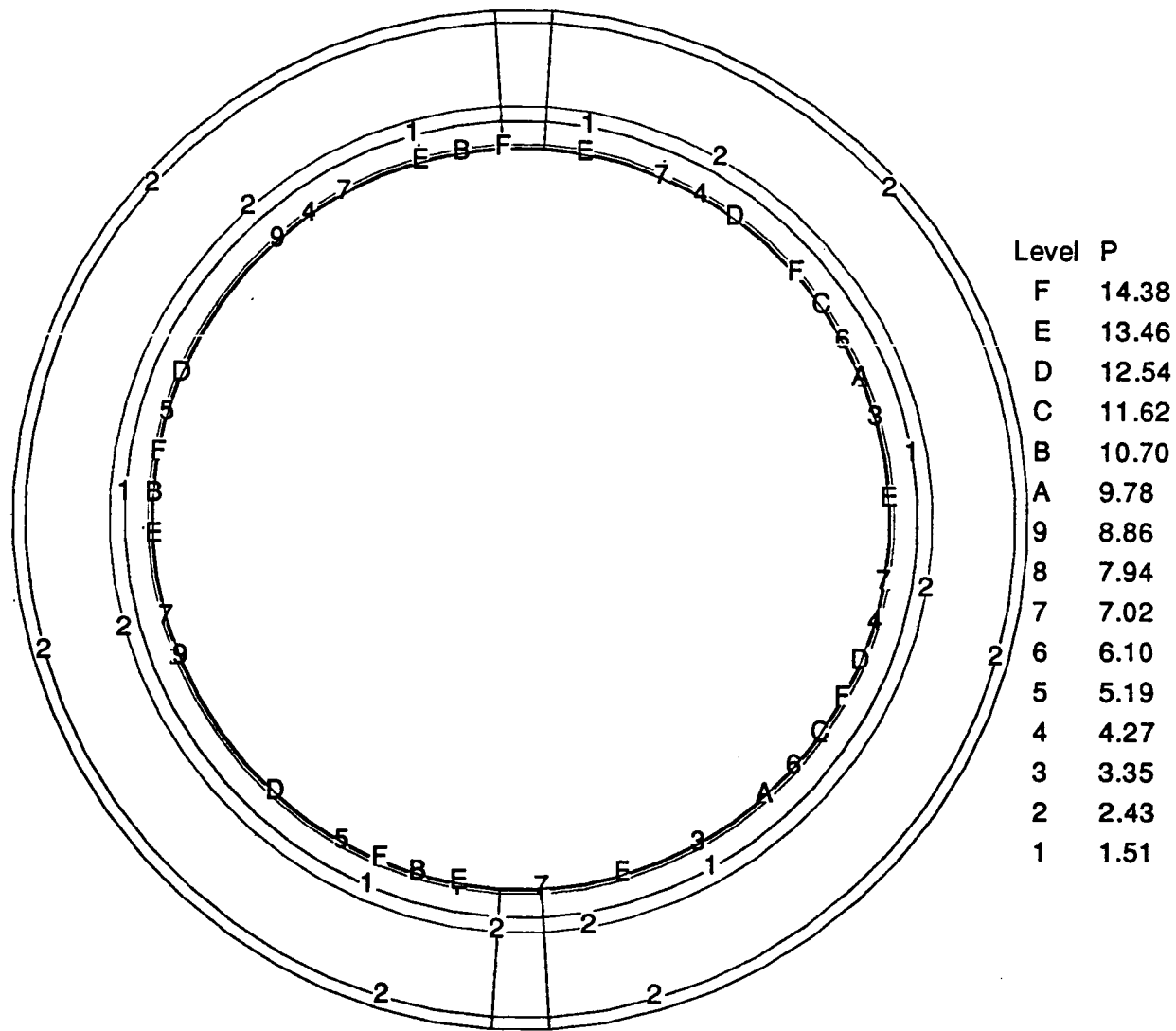


Fig. 5.45 Pressure contours for on-axis biconic at 0° AOA, $R_n=0.00383$ m, $x=11.9 R_n$.

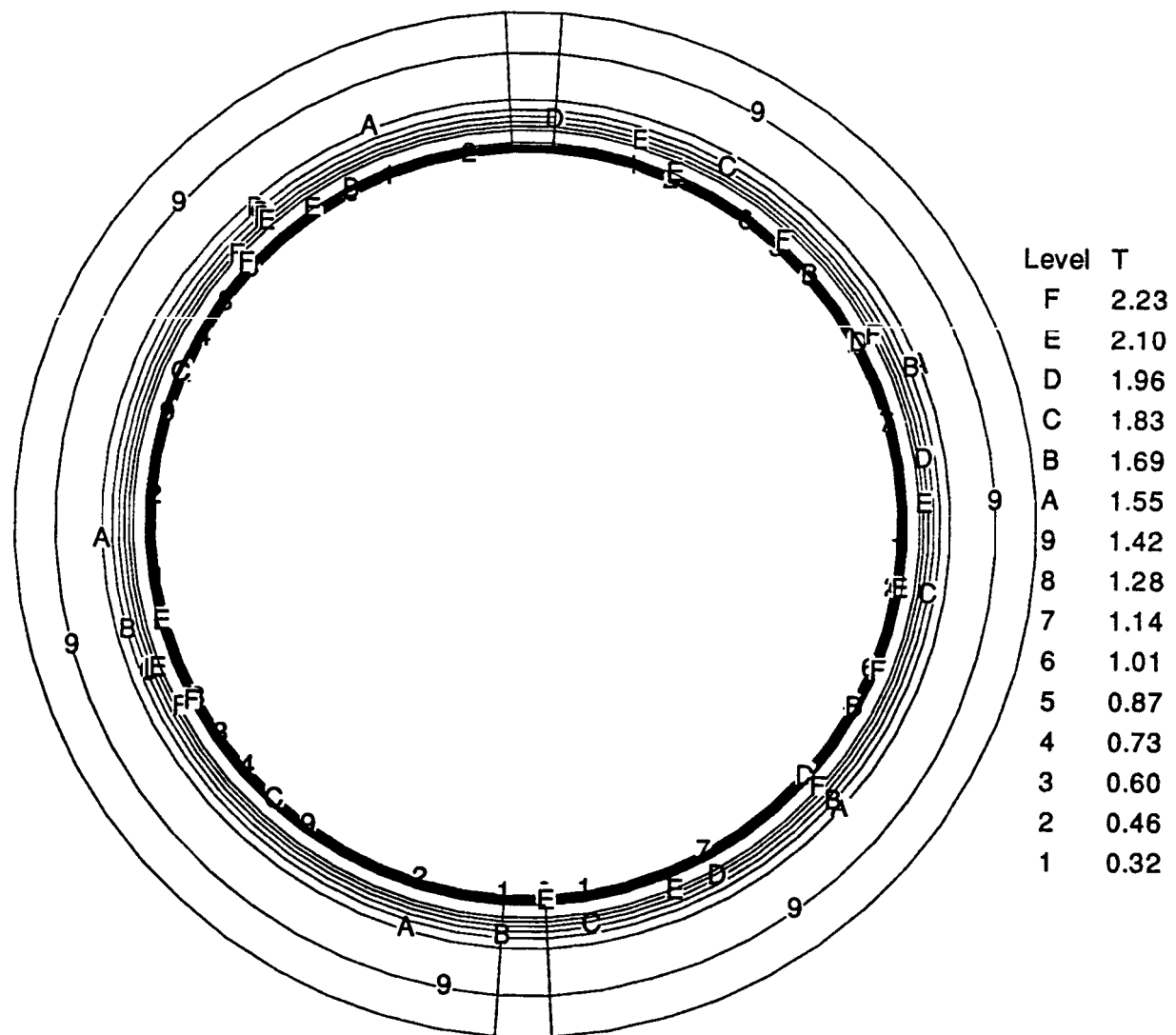


Fig. 5.46 Temperature contours for on-axis
biconic at 0° AOA, $R_n=0.00383$ m, $x=11.9 R_n$.

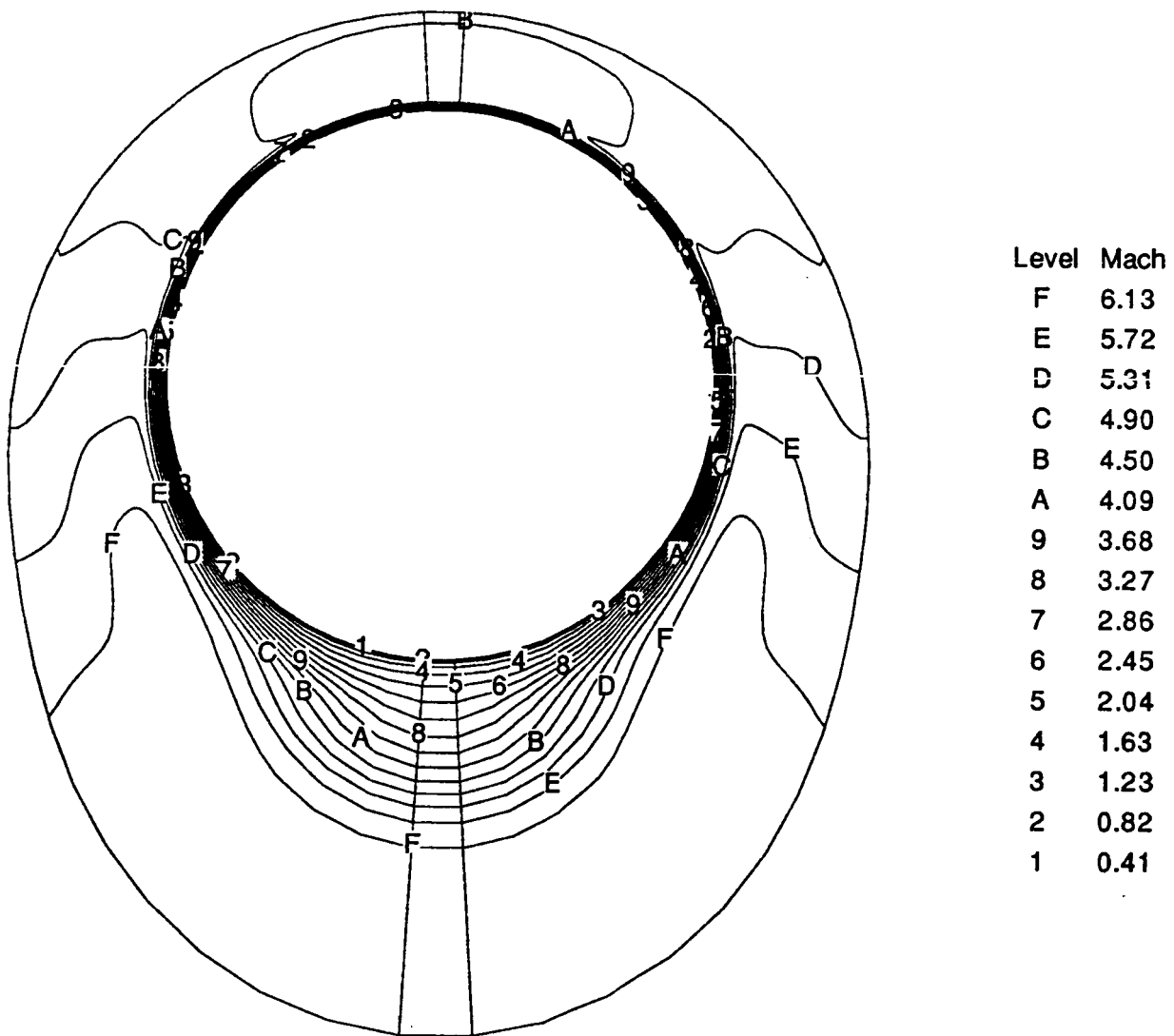


Fig. 5.47 Mach contours for on-axis biconic at 12° AOA, $R_n=0.00383$ m, $x=26 R_n$.

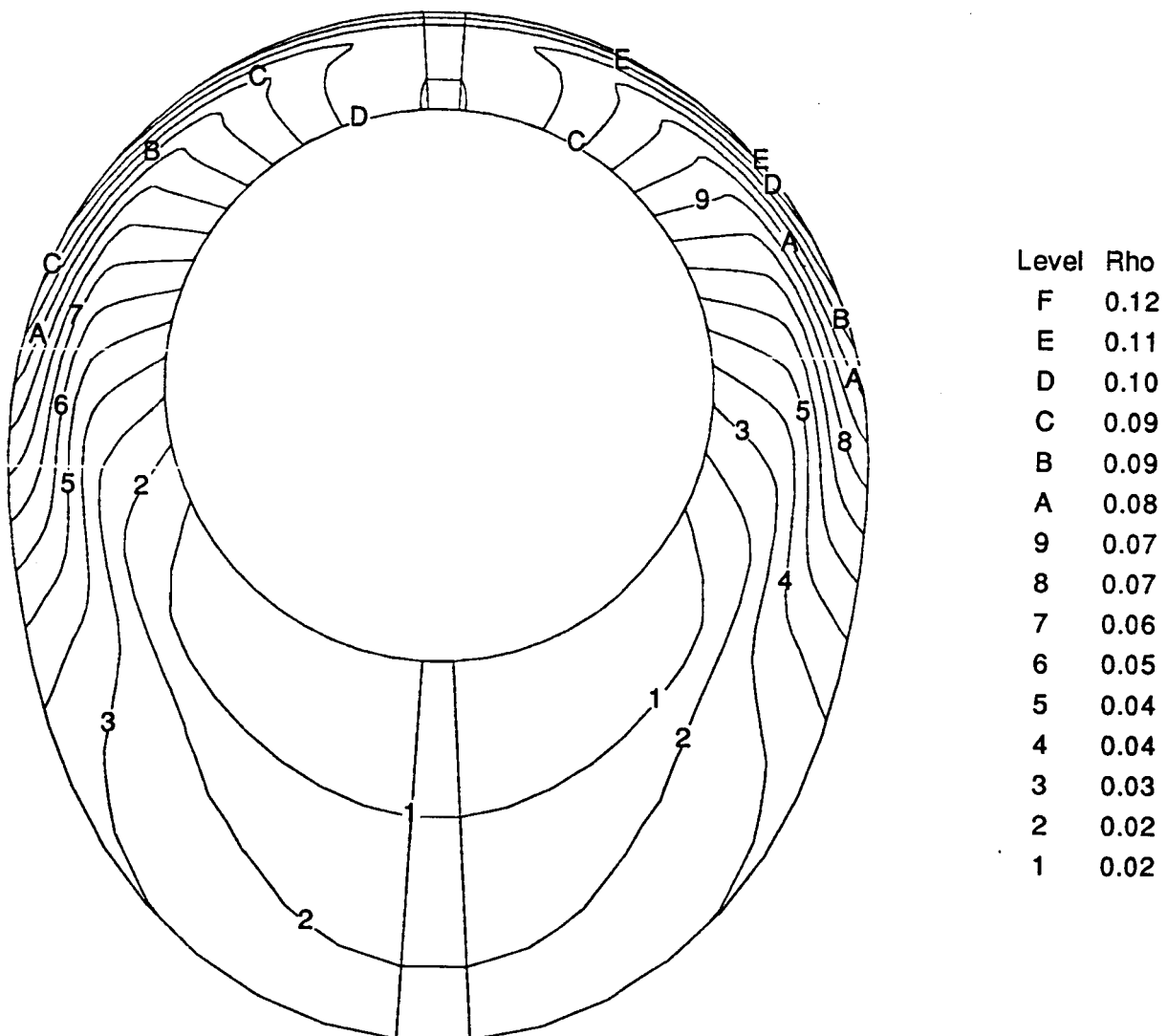


Fig. 5.48 Density contours for on-axis biconic at 12° AOA, $R_n=0.00383$ m, $x=26 R_n$.

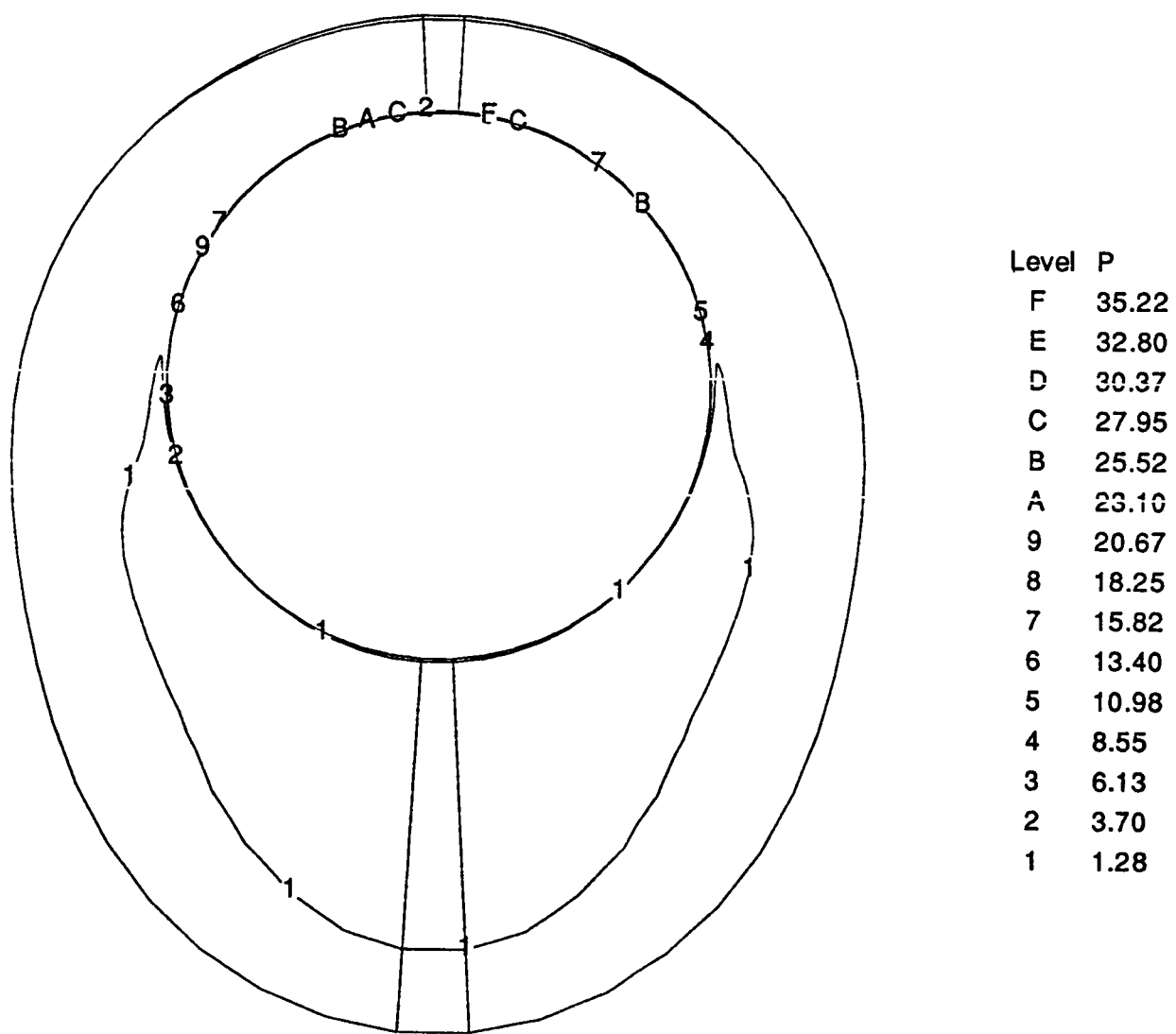


Fig. 5.49 Pressure contours for on-axis biconic at 12° AOA, $R_n=0.00383$ m, $x=26 R_n$.

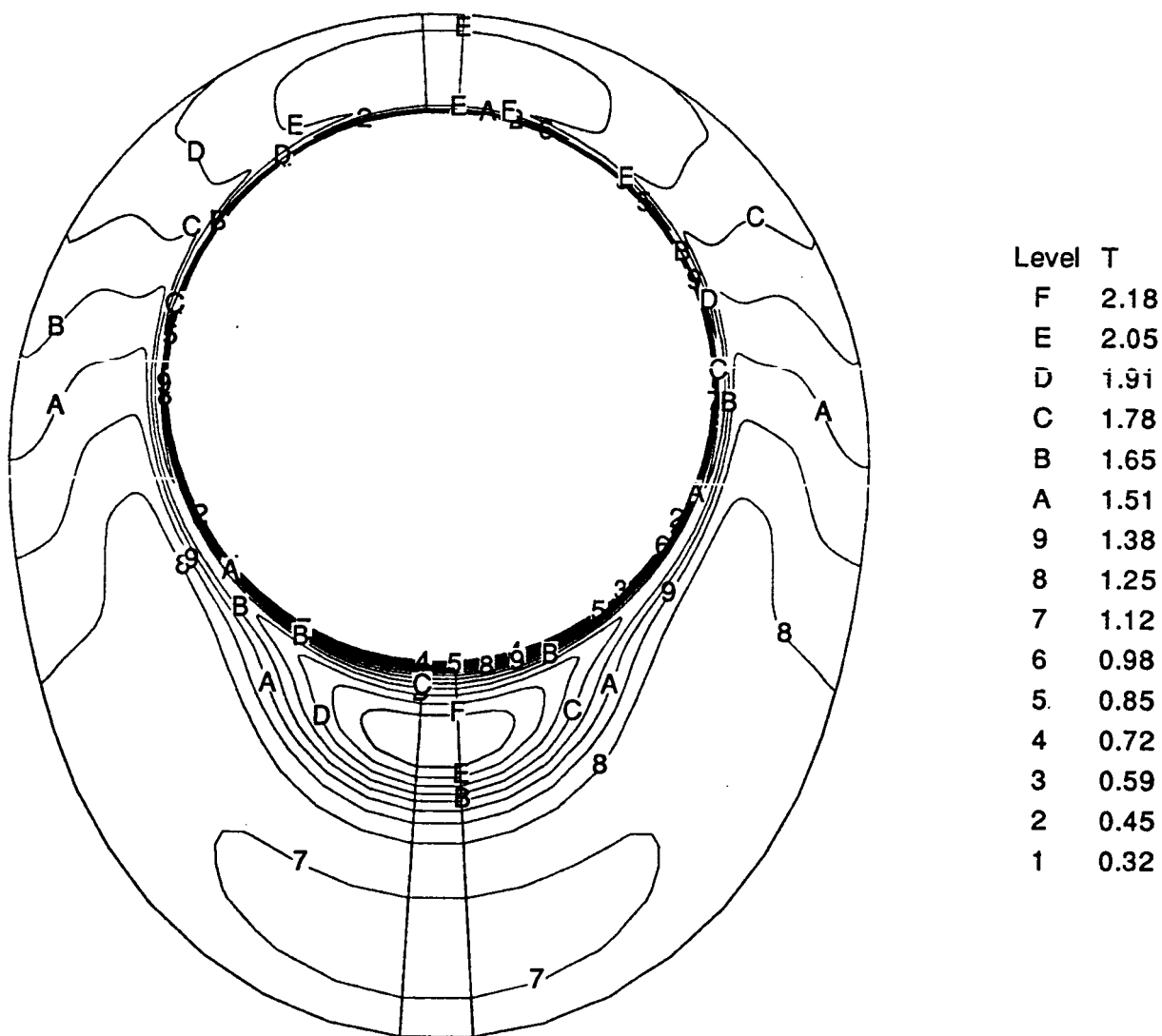


Fig. 5.50 Temperature contours for on-axis
biconic at 12° AOA, $R_n=0.00383$ m, $x=26 R_n$.

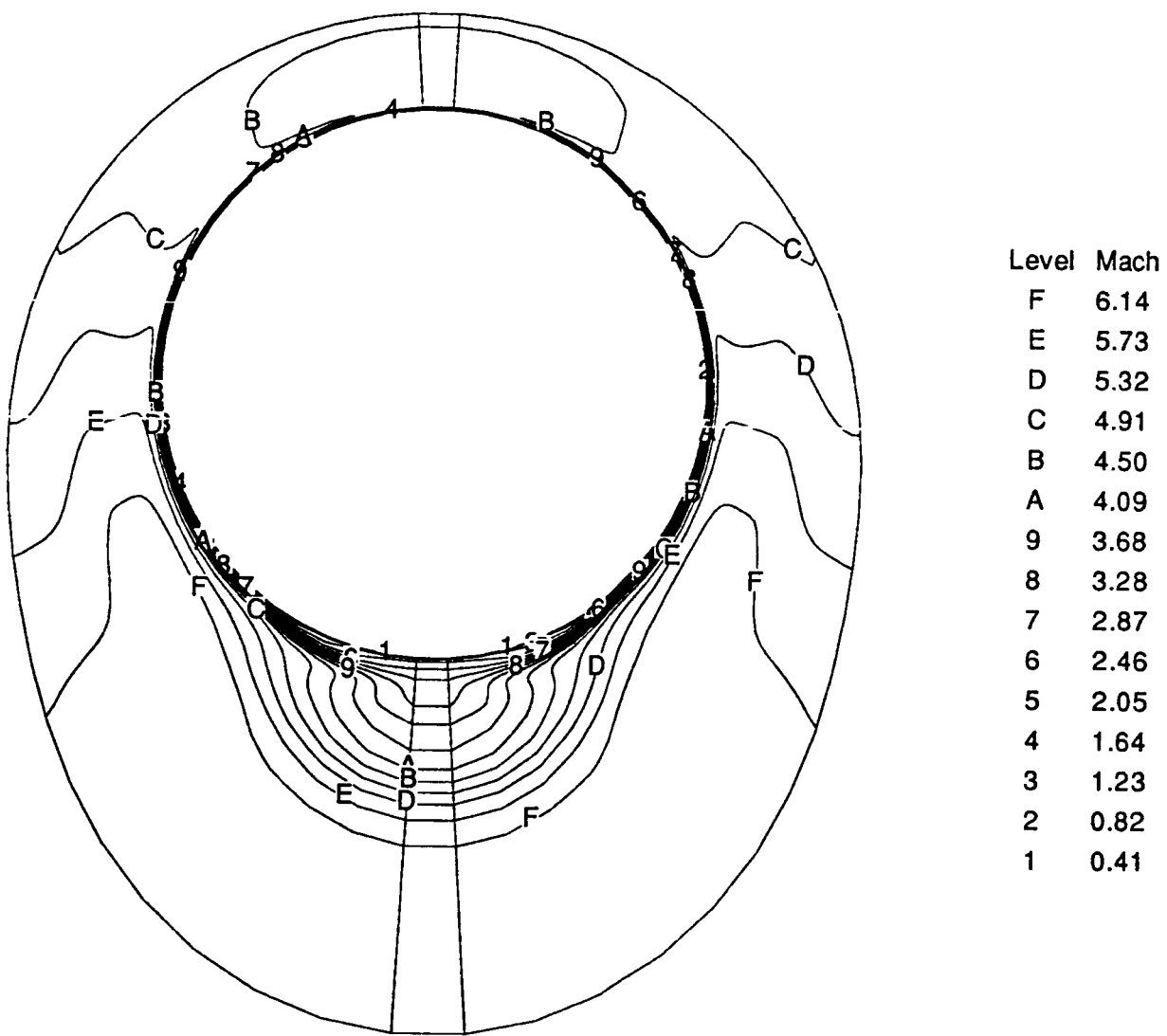


Fig. 5.51 Mach contours for on-axis biconic at 12° AOA, $R_n=0.04$ m, $x=26 R_n$.

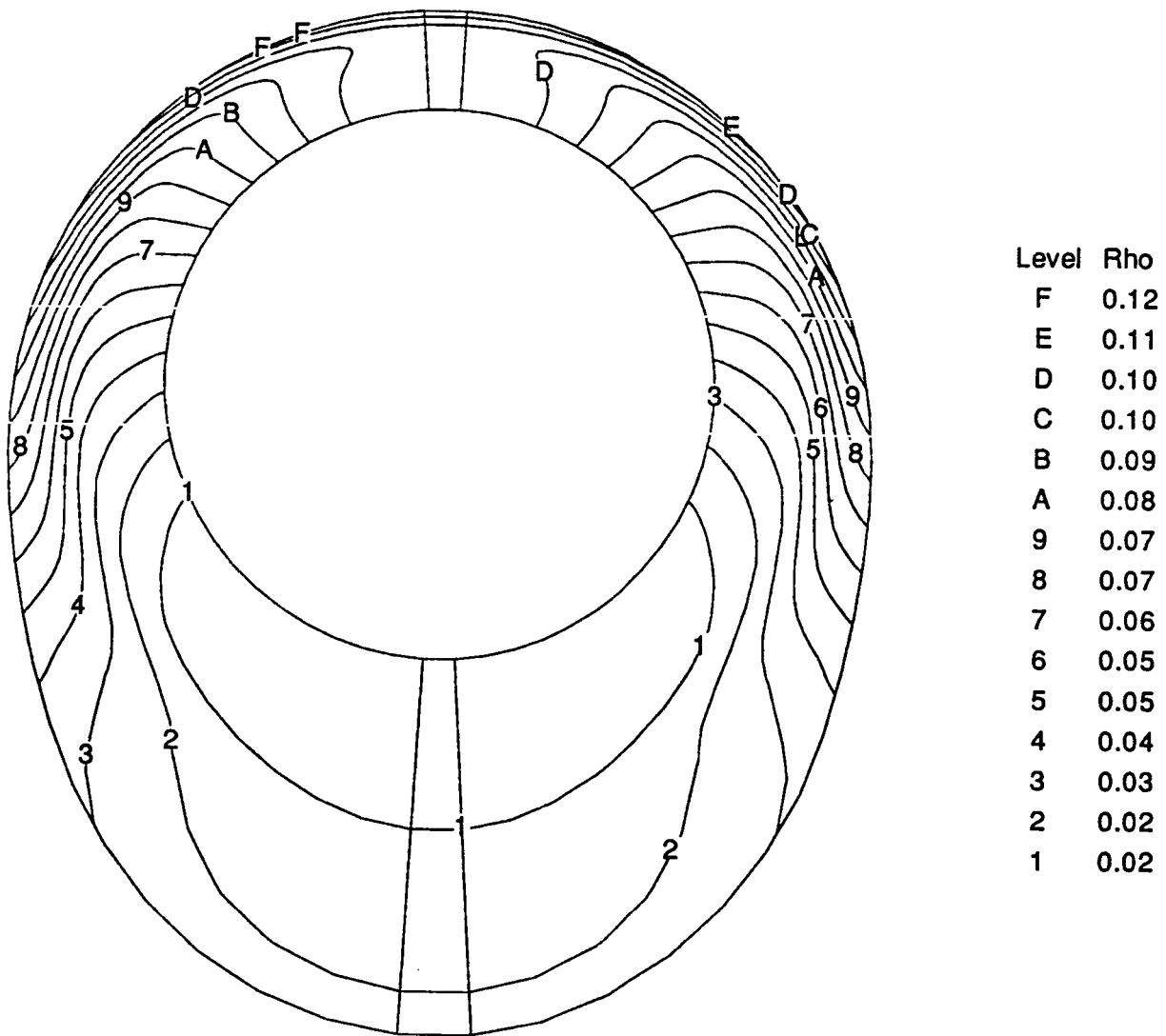


Fig. 5.52 Density contours for on-axis biconic at 12° AOA, $R_n=0.04$ m, $x=26 R_n$.

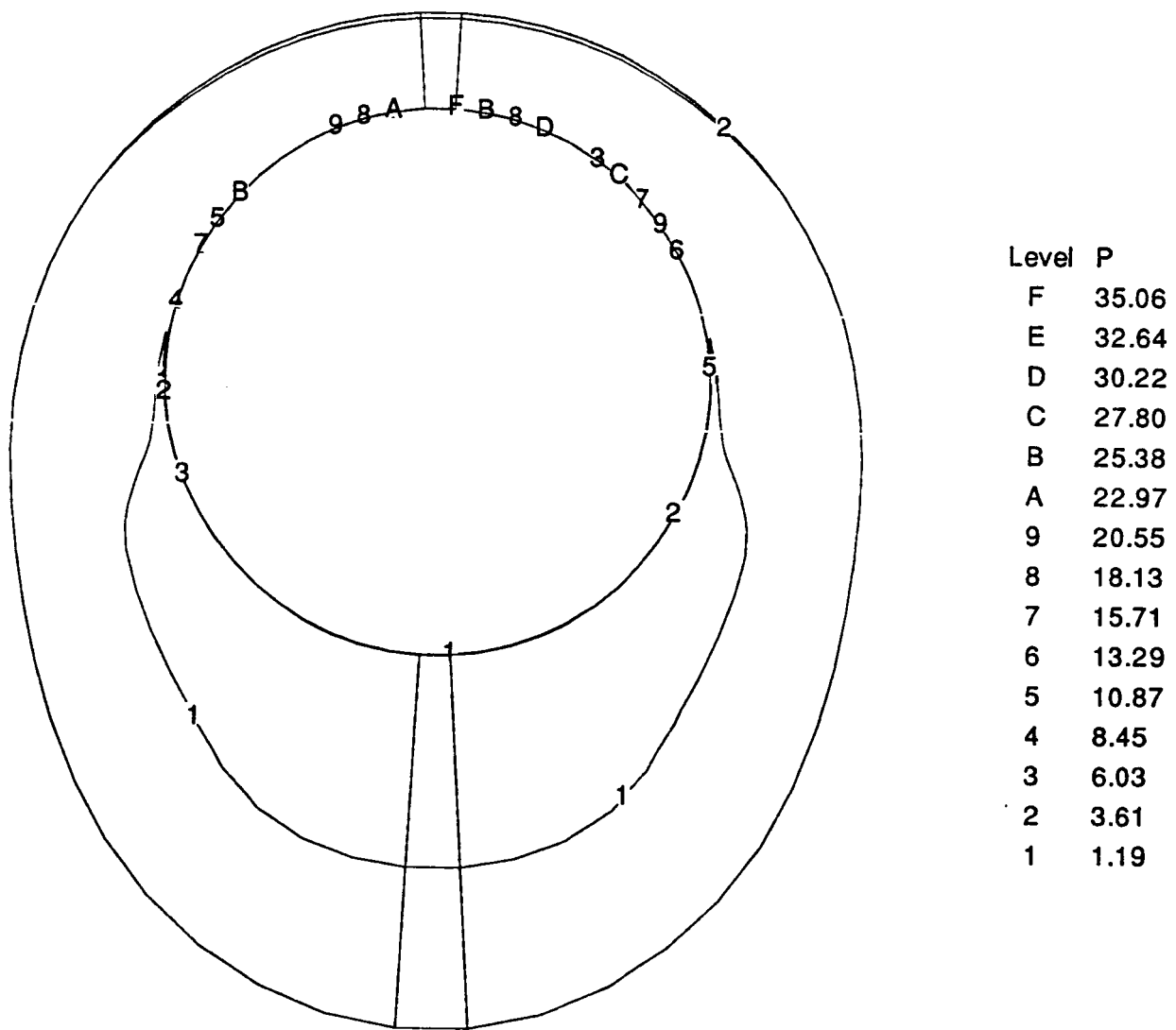


Fig. 5.53 Pressure contours for on-axis biconic at 12° AOA, $R_n=0.04$ m, $x=26 R_n$.

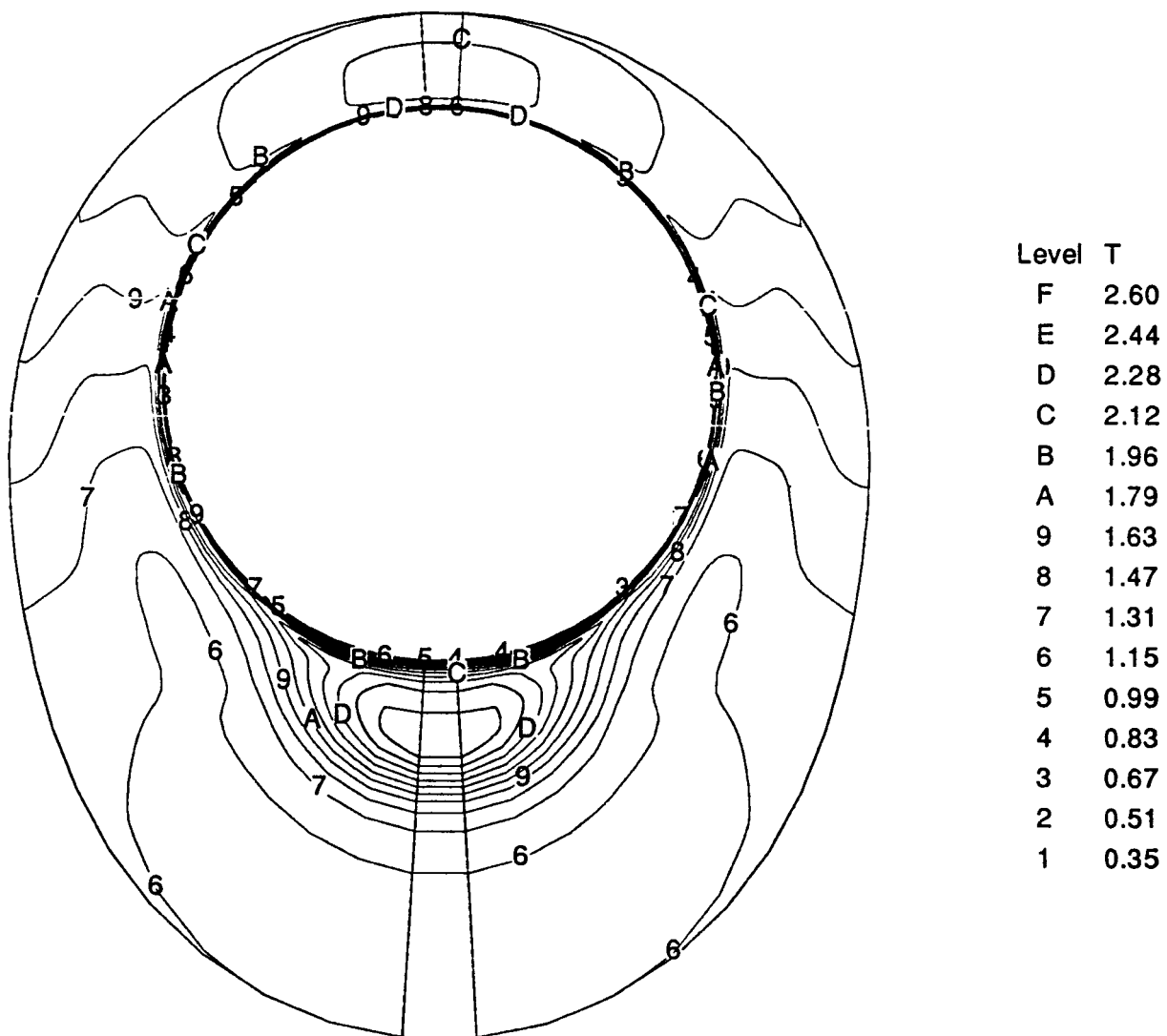


Fig. 5.54 Temperature contours for on-axis biconic at 12° AOA, $R_n=0.04$ m, $x=26 R_n$.

Chapter 6

CONCLUSIONS

The PNS code is successfully applied to study the effects of leading edge bluntness and angle of attack on the flow field and wall quantities of a spherically blunted on-axis biconic configuration in air at Mach 6.89 and $\gamma=1.3$. The variation of wall quantities at low incidence ($\alpha=2^\circ$) and high Mach number ($M_\infty = 20$) for a 5° spherically blunted cone is also studied. The downstream influence of nose bluntness for the blunted cone persists up to 200 nose radii approximately. The complete flow field is accurately predicted using a combination of the full Navier Stokes equations in the nose region and parabolized Navier Stokes equations farther downstream. For the on-axis $12.84^\circ / 7^\circ$ biconic configuration, the influence of entropy layer generated by the shock curvature on the flow field is also addressed. It is found that the entropy layer affects the development of the boundary layer far downstream of the nose section. The entropy layer is not swallowed by the boundary layer for the straight biconic geometry because the flow solution is marched only 32 nose radii downstream of the nose region.

With the increase in AOA from 0° to 12° , heating on the windward ray increases for the blunted on-axis biconic, and decreases on the leeward ray. The same trend is observed for the surface pressure and skin friction coefficient, but shock stand-off distance increases on the leeward side and decreases on the windward side. A similar reasoning can be applied for the results obtained for the spherically blunted cone. The decrease in the leeward side heating rate is more sensitive to AOA compared to the increase in the windward side heating. Heating on the windward side of the on-axis aft-cone is roughly half of that observed on the fore-cone, and leeward side heating is one order of magnitude less than that on the windward side. For the on-axis biconic, the heating on

the leeward side at the aft-cone section starts increasing a little at $\alpha=12^\circ$. This effect is more pronounced when the nose bluntness is increased by an order of magnitude. This trend is attributed to flow separation on leeward side and formation of vortices. The circumferential plot of wall heat transfer and coefficient of pressure and also the cross flow velocity vector plot show this effect more clearly.

With the increase in nose bluntness by an order of magnitude, the windward heating for the on-axis fore-cone section decreases by a factor of four, and by a factor of two on the aft-cone section at 12° AOA. Heating on the leeward ray also decreases by a factor of about five for the fore-cone section, but there is a little change for aft-cone section. A similar trend is observed for the skin friction coefficient. The surface pressure distribution is not sensitive to leading edge bluntness. The shock shape for the blunted bicone looks similar to the sharp one, but the shock radii increase by an order of magnitude.

REFERENCES

1. Miller, C.G. and Gnoffo, P.A., "Pressure Distributions and Shock Shapes for 12.84° / 7° On-Axis and Bent-Nose Biconics in Air at Mach 6," NASA-TM-83222, January 1981.
2. Singh, D.J. and Tiwari, S.N., "Nose Bluntness Effects on Flow field and Wall Quantities Over Slender Bodies in Hypersonic Flows," Department of Mechanical Engineering and Mechanics, College of Engineering and Technology, Old Dominion University, Norfolk, Virginia, Progress Report NAG-1-423, June 30, 1989.
3. Tracy R.R., "Hypersonic Flow over a Yawed Circular Cone," Hypersonic Research Project, Contract No. DA-31-124-ARO(D)-33, Memorandum No. 69, August, 1963.
4. Lubard, S.C. and Helliwell, W.S., "Calculation of the Flow on a Cone at High Angle of Attack," AIAA Journal, Vol.12, No.7. July 1974., pp. 965-973.
5. Stetson, K.F., "Boundary Layer Separation on Slender Cones at Angle of Attack," AIAA Journal, Vol. 10, No.5, May 1972 pp. 642-648.
6. Stetson, K.F., "Effect of Bluntness and Angle of Attack on Boundary Layer Transition on Cones and Biconic Configurations," AIAA Paper 79-0269, January 1979.
7. Holden, M.S., "Experimental Studies of Surface Roughness, Entropy Swallowing and Boundary Layer Transition Effects on the Skin Friction and Heat Transfer Distribution in High Speed Flows," AIAA Paper 82-0034, January 1982.
8. Miller, C.G. and Gnoffo, P.A., "An Experimental Investigation of Hypersonic Flow Over Biconics at Incidence and Comparison to Prediction," AIAA Paper 82-1382, August 1982.
9. Vigneron, Y.C., Rakcih, J.V. and Tannehill, J.C., "Calculation of Supersonic Viscous Flow Over Delta Wings with Sharp Subsonic Leading Edges," NASA TM 78500, June 1978.
10. Miller, C.G., Micol, J.R., Gnoffo, P.A., and Wilder, S.E., "Heat Transfer Distributions on Biconics at Incidence in Hypersonic-Hypervelocity He, N₂, Air and Co₂ Flows," AIAA Paper 83-1508, June 1983.
11. Gnoffo, P.A., "Hypersonic Flows over Biconics Using a Variable-Effective-Gama, Parabolized-Navier-Stokes Code," AIAA Paper 83-1666, July 1983.

12. Kumar, A.J., Graves, R.A., Jr, Weilmuenster, K.J., and Tiwari, S.N., "Laminar and Turbulent Flow Solutions with Radiation and Ablation Injection for Jovian Entry," AIAA Paper 80-0288, January 1980.
13. Moskovitz, C.A. and DeJarnette, F.R., "Effects of Surface Perturbations on the Asymmetric Vortex Flow Over a Slender Body," AIAA Paper 88-0483, January 1988.
14. Prabhu, D.K., Tannehill, J.C., and Marvin, J.G., "A New PNS Code for Chemical Nonequilibrium Flows," AIAA Journal, Vol.26, No.7, July 1988, pp. 808-815.
15. Ericsson, L.E., "Effect of Nose Bluntness and Cone Angle on Slender Vehicle Transition," AIAA Journal, Vol.26, No.10, October 1988, pp. 1168-1174.
16. Malik, M.R., Spall, R.E. and Chang, C.L., "Effect of Nose Bluntness on Boundary Layer Stability and Transition," AIAA Paper 90-0112, January 1990.
17. Gupta, R.N., Lee, K.P., Zoby, E.V., Moss, J.N. and Thompson, R.A., "Hypersonic Viscous Shock-Layer Solutions Over Long Slender Bodies-Part1," Journal of Spacecraft and Rockets, Vol.27, No.2, March-April 1990, pp. 175-184.
18. Moskovitz, C.A., Hall, R.M., and DeJarnette, F.R., "Combined Effects of Nose Bluntness and Surface Perturbations on Asymmetric Flow Past Slender Bodies," Journal of Aircraft, Vol.27, No.10, October 1990, pp. 909-910.
19. Singh, D.J., Kumar, A., and Tiwari, S.N., "Effect of Nose Bluntness on Flow field and Wall Quantities Over Slender Bodies in Hypersonic Flows," AIAA Paper 89-0270, January 1989; also Journal of Thermophysics and Heat Transfer, (accepted for publication).
20. Anderson, J.D., Jr., Hypersonic and High Temperature Gas Dynamics, McGraw Hill, 1989.
21. Ferri, A., "Some Heat Transfer problems in Hypersonic Flows," Aeronautics and Astronautics, Pergamon Press, New York, 1960, pp. 344-377.
22. Ferri, A. and Libby, P.A., "Note on the Interaction between the Boundary Layer and the Inviscid Flow," Journal of Aerospace Sciences, Vol. 21, 1954, pp. 130.
23. Stetson, K.F., "Nose tip Bluntness Effects on Cone Frustum Boundary Layer Transition in Hypersonic Flow," AIAA Paper 83-1763, July 1983.
24. Anderson, D.A., Tannehill, J.C., and Pletcher, R.H., Computational Fluid Mechanics and Heat Transfer, McGraw Hill, New York 1984.

25. Gnoffo, P.A., "A Vectorized Finite Volume, Adaptive Grid Algorithm Applied to Planetary Entry Problems," AIAA Paper 82-1018, June 1982.
26. Beam, R.M. and Warming, R.F., "An Implicit Factored Scheme for the Compressible Navier-Stokes Equation," AIAA Journal, Vol. 16, No.4, April 1978 pp. 393-401.
27. Rubin, S.G. and Lin, T.C., " Numerical Methods for Two and Three dimensional Viscous Flow Problems: Application to Hypersonic Leading Edge Equations.," Polytechnic Institute of Brooklyn, Farmingdale, N.Y., Rept. No. 71-8, April 1971.
28. Lubard, S.C. and Helliwell, W.S., "Calculation of the Flow on a Cone at High Angle of Attack," , R&D Associates, Santa Monica, California, RDA TR 150, February 1973.
29. Hoffmann K.A., Computational Fluid Dynamics for Engineers, A Publication of Engineering Education system, Austin, Texas 1989.
30. Miller, C.G., Blackstock, T.A., Helms V.T., and Midden, R.E., "An Experimental Investigation of Control Surface Effectiveness and Real-Gas Simulation for Biconics," AIAA Paper 83-0213, January 1983.

APPENDIX

CALCULATION OF JACOBIANS

The Jacobians $\frac{\partial F_1}{\partial U_1}$ and $\frac{\partial G_1}{\partial U_1}$ are given by

$$\frac{\partial F_1}{\partial U_1} = \frac{\partial}{\partial U_1} \left\{ \frac{a}{J} \left[\left(a \frac{\partial \eta}{\partial a} - b \frac{\partial \eta}{\partial b} - c \frac{\partial \eta}{\partial c} \right) (E - E_v) + \frac{\partial \eta}{\partial b} (F - F_v) + \frac{\partial \eta}{\partial c} (G - G_v) \right] \right\}$$

$$\frac{\partial G}{\partial U_1} = \frac{\partial}{\partial U_1} \left\{ \frac{a}{J} \left[\left(-b \frac{\partial \zeta}{\partial b} - c \frac{\partial \zeta}{\partial c} \right) (E - E_v) + \frac{\partial \zeta}{\partial b} (F - F_v) + \frac{\partial \zeta}{\partial c} (G - G_v) \right] \right\}$$

These Jacobians have an inviscid part and a viscous part

$$\begin{aligned} \frac{\partial F_1}{\partial U_1} &= \left(\frac{\partial F_1}{\partial U_1} \right)_{\text{inviscid}} - \left(\frac{\partial F_1}{\partial U_1} \right)_{\text{viscous}} \\ \frac{\partial G_1}{\partial U_1} &= \left(\frac{\partial G_1}{\partial U_1} \right)_{\text{inviscid}} - \left(\frac{\partial G_1}{\partial U_1} \right)_{\text{viscous}} \end{aligned}$$

The inviscid part can be written as a linear combination of $\frac{\partial E}{\partial U}$, $\frac{\partial F}{\partial U}$, $\frac{\partial G}{\partial U}$

$$\begin{aligned} \left(\frac{\partial F_1}{\partial U_1} \right)_{\text{inviscid}} &= \frac{1}{a} \left(a \frac{\partial \eta}{\partial a} - b \frac{\partial \eta}{\partial b} - c \frac{\partial \eta}{\partial c} \right) \frac{\partial E}{\partial U} + \frac{1}{a} \frac{\partial \eta}{\partial b} \frac{\partial F}{\partial U} + \frac{1}{a} \frac{\partial \eta}{\partial c} \frac{\partial G}{\partial U} \\ \left(\frac{\partial G_1}{\partial U_1} \right)_{\text{inviscid}} &= \frac{1}{a} \left(-b \frac{\partial \zeta}{\partial b} - c \frac{\partial \zeta}{\partial c} \right) \frac{\partial E}{\partial U} + \frac{1}{a} \frac{\partial \zeta}{\partial b} \frac{\partial F}{\partial U} + \frac{1}{a} \frac{\partial \zeta}{\partial c} \frac{\partial G}{\partial U} \end{aligned}$$

where

$$\frac{\partial E}{\partial U} = \begin{bmatrix} 0 & 1 & 0 & 0 & 0 \\ \frac{\gamma-3}{2}u^2 + & (3-\gamma)u & -(\gamma-1)v & -(\gamma-1)w & \gamma-1 \\ \frac{\gamma-1}{2}(v^2+w^2) & & & & \\ -uv & v & u & 0 & 0 \\ -uw & w & 0 & u & 0 \\ [-\gamma e_t + (\gamma-1) & \gamma e_t - (\gamma-1) & -(\gamma-1)uv & -(\gamma-1)uw & \gamma u \\ (u^2+v^2+w^2)]u & \frac{3u^2+v^2+w^2}{2} & & & \end{bmatrix}$$

$$\frac{\partial F}{\partial U} = \begin{bmatrix} 0 & 0 & 1 & 0 & 0 \\ -uv & v & u & 0 & 0 \\ \frac{\gamma-1}{2}(u^2+w^2) & -(\gamma-1)u & (3-\gamma)v & -(\gamma-1)w & \gamma-1 \\ +\left(\frac{\gamma-3}{2}\right)v^2 & & & v & 0 \\ -vw & 0 & w & & \gamma v \\ [-\gamma e_t + (\gamma-1) & -(\gamma-1)uv & \gamma e_t - \frac{\gamma-1}{2} & -(\gamma-1)vw & \\ (u^2+v^2+w^2)]v & & (u^2+3v^2+w^2) & & \end{bmatrix}$$

$$\frac{\partial G}{\partial U} = \begin{bmatrix} 0 & 0 & 0 & 1 & 0 \\ -uw & w & 0 & u & 0 \\ -vw & 0 & w & v & 0 \\ \frac{\gamma-1}{2}(u^2+v^2) & -(\gamma-1)u & -(\gamma-1)v & (3-\gamma)w & \gamma-1 \\ +\frac{\gamma-3}{2}w^2 & & & & \\ [-\gamma e_t + (\gamma-1) & -(\gamma-1)uw & -(\gamma-1)vw & \gamma e_t - \frac{\gamma-1}{2} & \gamma w \\ (u^2+v^2+w^2)]w & & & (u^2+v^2+3w^2) & \end{bmatrix}$$

The viscous part of the Jacobians is

$$\left(\frac{\partial F_1}{\partial U_1} \right)_{\text{viscous}} = \frac{\partial}{\partial U_1} \left\{ \frac{a}{J} \left[\left(a \frac{\partial \eta}{\partial a} - b \frac{\partial \eta}{\partial b} - c \frac{\partial \eta}{\partial c} \right) E_v + \frac{\partial \eta}{\partial b} F_v + \frac{\partial \eta}{\partial c} G_v \right] \right\}$$

$$\left(\frac{\partial F_1}{\partial U_1} \right)_{\text{viscous}} = \frac{\mu}{JRe} \times$$

$$\begin{bmatrix} 0 & 0 & 0 & 0 & 0 \\ -\left[l_1 \left(\frac{J}{a^2} \frac{u}{\rho} \right)_\eta + l_4 \left(\frac{J}{a^2} \frac{v}{\rho} \right)_\eta \right. & l_1 \left(\frac{J}{a^2} \frac{1}{\rho} \right)_\eta & l_4 \left(\frac{J}{a^2} \frac{1}{\rho} \right)_\eta & l_5 \left(\frac{J}{a^2} \frac{1}{\rho} \right)_\eta & 0 \\ \left. + l_5 \left(\frac{J}{a^2} \frac{w}{\rho} \right)_\eta \right] & & & & \\ -\left[l_4 \left(\frac{J}{a^2} \frac{u}{\rho} \right)_\eta + l_2 \left(\frac{J}{a^2} \frac{v}{\rho} \right)_\eta \right. & l_4 \left(\frac{J}{a^2} \frac{1}{\rho} \right)_\eta & l_2 \left(\frac{J}{a^2} \frac{1}{\rho} \right)_\eta & l_6 \left(\frac{J}{a^2} \frac{1}{\rho} \right)_\eta & 0 \\ \left. + l_6 \left(\frac{J}{a^2} \frac{w}{\rho} \right)_\eta \right] & & & & \\ -\left[l_5 \left(\frac{J}{a^2} \frac{u}{\rho} \right)_\eta + l_6 \left(\frac{J}{a^2} \frac{v}{\rho} \right)_\eta \right. & l_5 \left(\frac{J}{a^2} \frac{1}{\rho} \right)_\eta & l_6 \left(\frac{J}{a^2} \frac{1}{\rho} \right)_\eta & l_3 \left(\frac{J}{a^2} \frac{1}{\rho} \right)_\eta & 0 \\ \left. + l_3 \left(\frac{J}{a^2} \frac{w}{\rho} \right)_\eta \right] & & & & \\ -l_1 \left(\frac{J}{a^2} \frac{u^2}{\rho} \right)_\eta - l_2 \left(\frac{J}{a^2} \frac{v^2}{\rho} \right)_\eta & l_1 \left(\frac{J}{a^2} \frac{u}{\rho} \right)_\eta & l_4 \left(\frac{J}{a^2} \frac{u}{\rho} \right)_\eta & l_5 \left(\frac{J}{a^2} \frac{u}{\rho} \right)_\eta & l_7 \left(\frac{J}{a^2} \frac{1}{\rho} \right)_\eta \\ -l_3 \left(\frac{J}{a^2} \frac{w^2}{\rho} \right)_\eta - 2l_4 \left(\frac{J}{a^2} \frac{uv}{\rho} \right)_\eta & +l_4 \left(\frac{J}{a^2} \frac{v}{\rho} \right)_\eta & +l_2 \left(\frac{J}{a^2} \frac{v}{\rho} \right)_\eta & +l_6 \left(\frac{J}{a^2} \frac{v}{\rho} \right)_\eta & +l_6 \left(\frac{J}{a^2} \frac{v}{\rho} \right)_\eta \\ -2l_5 \left(\frac{J}{a^2} \frac{uw}{\rho} \right)_\eta - 2l_6 \left(\frac{J}{a^2} \frac{vw}{\rho} \right)_\eta & +l_5 \left(\frac{J}{a^2} \frac{w}{\rho} \right)_\eta & +l_6 \left(\frac{J}{a^2} \frac{w}{\rho} \right)_\eta & +l_3 \left(\frac{J}{a^2} \frac{w}{\rho} \right)_\eta & +l_3 \left(\frac{J}{a^2} \frac{w}{\rho} \right)_\eta \\ -l_7 \left\{ \frac{J}{a^2} \left[\frac{p}{(\gamma-1)\rho^2} - \frac{u^2+v^2+w^2}{2\rho} \right] \right\}_\eta & -l_7 \left(\frac{J}{a^2} \frac{u}{\rho} \right)_\eta & -l_7 \left(\frac{J}{a^2} \frac{v}{\rho} \right)_\eta & -l_7 \left(\frac{J}{a^2} \frac{w}{\rho} \right)_\eta & -l_7 \left(\frac{J}{a^2} \frac{w}{\rho} \right)_\eta \end{bmatrix}$$

where

$$\begin{aligned}
 l_1 &= \frac{4}{3}\bar{l}_1^2 + \bar{l}_2^2 + \bar{l}_3^2 \\
 l_2 &= \bar{l}_1^2 + \frac{4}{3}\bar{l}_2^2 + \bar{l}_3^2 \\
 l_3 &= \bar{l}_1^2 + \bar{l}_2^2 + \frac{4}{3}\bar{l}_3^2 \\
 l_4 &= \frac{\bar{l}_1\bar{l}_2}{3} \\
 l_5 &= \frac{\bar{l}_1\bar{l}_3}{3} \\
 l_6 &= \frac{\bar{l}_2\bar{l}_3}{3} \\
 l_7 &= \frac{\gamma}{Pr}(\bar{l}_1^2 + \bar{l}_2^2 + \bar{l}_3^2)
 \end{aligned}$$

$$\begin{aligned}
 \bar{l}_1 &= a\frac{\partial\eta}{\partial a} - b\frac{\partial\eta}{\partial b} - c\frac{\partial\eta}{\partial c} \\
 \bar{l}_2 &= \frac{\partial\eta}{\partial b} \\
 \bar{l}_3 &= \frac{\partial\eta}{\partial c}
 \end{aligned}$$

and $(.)\eta$ indicates derivative with respect to η . Similarly

$$\left(\frac{\partial G_1}{\partial U_1} \right)_{\text{viscous}} = \frac{\partial}{\partial U_1} \left\{ \frac{a}{J} \left[\left(-b\frac{\partial\zeta}{\partial b} - c\frac{\partial\zeta}{\partial c} \right) E_v + \frac{\partial\zeta}{\partial b} F_v + \frac{\partial\zeta}{\partial c} G_v \right] \right\}$$

$$\left(\frac{\partial G_1}{\partial U_1} \right)_{\text{viscous}} = \frac{\mu}{JRe} \times$$

$$\begin{bmatrix}
0 & 0 & 0 & 0 & 0 \\
-\left[m_1 \left(\frac{J}{a^2} \frac{u}{\rho} \right) \zeta + m_4 \left(\frac{J}{a^2} \frac{u}{\rho} \right) \zeta + m_5 \left(\frac{J}{a^2} \frac{w}{\rho} \right) \zeta \right] & m_1 \left(\frac{J}{a^2} \frac{1}{\rho} \right) \zeta & m_4 \left(\frac{J}{a^2} \frac{1}{\rho} \right) \zeta & m_5 \left(\frac{J}{a^2} \frac{1}{\rho} \right) \zeta & 0 \\
-\left[m_4 \left(\frac{J}{a^2} \frac{u}{\rho} \right) \zeta + m_2 \left(\frac{J}{a^2} \frac{v}{\rho} \right) \zeta + m_6 \left(\frac{J}{a^2} \frac{w}{\rho} \right) \zeta \right] & m_4 \left(\frac{J}{a^2} \frac{1}{\rho} \right) \zeta & m_2 \left(\frac{J}{a^2} \frac{1}{\rho} \right) \zeta & m_6 \left(\frac{J}{a^2} \frac{1}{\rho} \right) \zeta & 0 \\
-\left[m_5 \left(\frac{J}{a^2} \frac{u}{\rho} \right) \zeta + m_6 \left(\frac{J}{a^2} \frac{v}{\rho} \right) \zeta + m_3 \left(\frac{J}{a^2} \frac{w}{\rho} \right) \zeta \right] & m_5 \left(\frac{J}{a^2} \frac{1}{\rho} \right) \zeta & m_6 \left(\frac{J}{a^2} \frac{1}{\rho} \right) \zeta & m_3 \left(\frac{J}{a^2} \frac{1}{\rho} \right) \zeta & 0 \\
-m_1 \left(\frac{J}{a^2} \frac{u^2}{\rho} \right) \zeta -m_2 \left(\frac{J}{a^2} \frac{v^2}{\rho} \right) \zeta -m_3 \left(\frac{J}{a^2} \frac{w^2}{\rho} \right) \zeta -2m_4 \left(\frac{J}{a^2} \frac{uv}{\rho} \right) \zeta -2m_5 \left(\frac{J}{a^2} \frac{uw}{\rho} \right) \zeta -2m_6 \left(\frac{J}{a^2} \frac{vw}{\rho} \right) \zeta -m_7 \left\{ \frac{J}{a^2} \left[\frac{P}{(\gamma-1)\rho^2} \right] \right\} & m_1 \left(\frac{J}{a^2} \frac{u}{\rho} \right) \zeta +m_4 \left(\frac{J}{a^2} \frac{v}{\rho} \right) \zeta +m_5 \left(\frac{J}{a^2} \frac{w}{\rho} \right) \zeta -m_7 \left(\frac{J}{a^2} \frac{u}{\rho} \right) \zeta -m_7 \left(\frac{J}{a^2} \frac{v}{\rho} \right) \zeta +m_3 \left(\frac{J}{a^2} \frac{w}{\rho} \right) \zeta -m_7 \left(\frac{J}{a^2} \frac{w}{\rho} \right) \zeta & m_4 \left(\frac{J}{a^2} \frac{u}{\rho} \right) \zeta +m_2 \left(\frac{J}{a^2} \frac{v}{\rho} \right) \zeta +m_6 \left(\frac{J}{a^2} \frac{w}{\rho} \right) \zeta -m_7 \left(\frac{J}{a^2} \frac{v}{\rho} \right) \zeta +m_6 \left(\frac{J}{a^2} \frac{w}{\rho} \right) \zeta +m_3 \left(\frac{J}{a^2} \frac{w}{\rho} \right) \zeta -m_7 \left(\frac{J}{a^2} \frac{w}{\rho} \right) \zeta & m_5 \left(\frac{J}{a^2} \frac{u}{\rho} \right) \zeta +m_6 \left(\frac{J}{a^2} \frac{v}{\rho} \right) \zeta +m_3 \left(\frac{J}{a^2} \frac{w}{\rho} \right) \zeta -m_7 \left(\frac{J}{a^2} \frac{v}{\rho} \right) \zeta +m_6 \left(\frac{J}{a^2} \frac{w}{\rho} \right) \zeta +m_3 \left(\frac{J}{a^2} \frac{w}{\rho} \right) \zeta -m_7 \left(\frac{J}{a^2} \frac{w}{\rho} \right) \zeta & m_7 \left(\frac{J}{a^2} \frac{1}{\rho} \right) \zeta +m_7 \left(\frac{J}{a^2} \frac{v}{\rho} \right) \zeta +m_3 \left(\frac{J}{a^2} \frac{w}{\rho} \right) \zeta -m_7 \left(\frac{J}{a^2} \frac{v}{\rho} \right) \zeta +m_6 \left(\frac{J}{a^2} \frac{w}{\rho} \right) \zeta +m_3 \left(\frac{J}{a^2} \frac{w}{\rho} \right) \zeta -m_7 \left(\frac{J}{a^2} \frac{w}{\rho} \right) \zeta
\end{bmatrix}$$

where

$$\begin{aligned}
 m_1 &= \frac{4}{3}\bar{m}_1^2 + \bar{m}_2^2 + \bar{m}_3^2 \\
 m_2 &= \bar{m}_1^2 + \frac{4}{3}\bar{m}_2^2 + \bar{m}_3^2 \\
 m_3 &= \bar{m}_1^2 + \bar{m}_2^2 + \frac{4}{3}\bar{m}_3^2 \\
 m_4 &= \frac{\bar{m}_1\bar{m}_2}{3} \\
 m_5 &= \frac{\bar{m}_1\bar{m}_3}{3} \\
 m_6 &= \frac{\bar{m}_2\bar{m}_3}{3} \\
 m_7 &= \frac{\gamma}{Pr}(\bar{m}_1^2 + \bar{m}_2^2 + \bar{m}_3^2)
 \end{aligned}$$

$$\begin{aligned}
 \bar{m}_1 &= -b\frac{\partial\zeta}{\partial b} - c\frac{\partial\zeta}{\partial c} \\
 \bar{m}_2 &= \frac{\partial\zeta}{\partial b} \\
 \bar{m}_3 &= \frac{\partial\zeta}{\partial c}
 \end{aligned}$$

and $(.)_\zeta$ indicates derivatives with respect to ζ . In these viscous Jacobians, the cross derivative viscous terms have been neglected and the coefficient of molecular viscosity has been assumed to depend only on the position, not on the vector U . Finally, the Jacobian $\frac{\partial E_1^*}{\partial U_1}$ is given by

$$\frac{\partial E_1^*}{\partial U_1} = \begin{bmatrix} 0 & 1 & 0 & 0 & 0 \\ \frac{w(\gamma-1)-2}{2}u^2 & [2-w(\gamma-1)]u - w(\gamma-1)v - w(\gamma-1)v & w(\gamma-1) & & \\ +\frac{w(\gamma-1)}{2}(v^2 + w^2) & & & & \\ -uv & v & u & 0 & 0 \\ -uw & w & 0 & u & 0 \\ [-\gamma e_t + (\gamma-1) & \gamma e_t - (\gamma-1) & -(\gamma-1)uv & -(\gamma-1)uw & \gamma u \\ (u^2 + v^2 + w^2)]u & \frac{3u^2+v^2+w^2}{2} & & & \end{bmatrix}$$